49. Zhu, M.; Liu, Y.; Yao, Y.; Jiang, J.; Zhang, F.; Yang, Z.; Lu, Z.; Kumakiri, I.; Chen, X.; Kita, H. Preparation and catalytic performance of Ti-MWW zeolite membrane for phenol hydroxylation. *Micropor. Mesopor. Mater.* **2018**, *268*, 84–87. [CrossRef]
50. Zholobenko, V.L.; Khodakov, A.Y.; Impéror-Clerc, M.; Durand, D.; Grillo, I. Initial stages of SBA-15 synthesis: An overview. *Adv. Colloid Interface Sci.* **2008**, *142*, 67–74. [CrossRef]

catalysts

MDPI

Article

Advanced Oxidation Process for Degradation of Carbamazepine from Aqueous Solution: Influence of Metal Modified Microporous, Mesoporous Catalysts on the Ozonation Process

Soudabeh Saeid [1], Matilda Kråkström [2], Pasi Tolvanen [1], Narendra Kumar [1,*], Kari Eränen [1], Jyri-Pekka Mikkola [1,3], Leif Kronberg [2], Patrik Eklund [2], Markus Peurla [4], Atte Aho [1], Andrey Shchukarev [3] and Tapio Salmi [1,*]

[1] Laboratory of Industrial Chemistry and Reaction Engineering, Johan Gadolin Process Chemistry Centre, Åbo Akademi University, Biskopsgatan 8, FI-20500 Åbo/Turku, Finland; soudabeh.saeid@abo.fi (S.S.); pasi.tolvanen@abo.fi (P.T.); kari.eranen@abo.fi (K.E.); jyri-pekka.mikkola@abo.fi (J.-P.M.); atte.aho@abo.fi (A.A.)

[2] Laboratory of Organic Chemistry, Johan Gadolin Process Chemistry Centre, Åbo Akademi University, Biskopsgatan 8, FI-20500 Åbo/Turku, Finland; matilda.krakstrom@abo.fi (M.K.); leif.kronberg@abo.fi (L.K.); patrik.j.eklund@abo.fi (P.E.)

[3] Technical Chemistry Department of Chemistry Chemical-Biological Center, Umeå University, SE-90187 Umeå, Sweden; andrey.shchukarev@umu.se

[4] Institue of Biomedicin, University of Turku, Kiinamyllynkatu 10, FI-205210 Turku, Finland; markus.peurla@utu.fi

* Correspondence: narendra.kumar@abo.fi (N.K.); tapio.salmi@abo.fi (T.S.)

Received: 22 November 2019; Accepted: 30 December 2019; Published: 7 January 2020

Abstract: Carbamazepine (CBZ), a widely used pharmaceutical compound, is one of the most detected drugs in surface waters. The purpose of this work was to identify an active and durable catalyst, which, in combination with an ozonation process, could be used to remove CBZ and its degradation products. It was found that the CBZ was completely transformed after ozonation within the first minutes of the treatment. However, the resulting degradation products, 1-(2-benzaldehyde)-4-hydro-(1H,3H)-quinazoline-2-one (BQM) and 1-(2-benzaldehyde)-(1H,3H)-quinazoline-2,4-dione (BQD), were more resistant during the ozonation process. The formation and degradation of these products were studied in more detail and a thorough catalytic screening was conducted to reveal the reaction kinetics of both the CBZ and its degradation products. The work was performed by non-catalytic ozonation and with six different heterogeneous catalysts (Pt-MCM-41-IS, Ru-MCM-41-IS, Pd-H-Y-12-EIM, Pt-H-Y-12-EIM, Pd-H-Beta-300-EIM and Cu-MCM-41-A-EIM) operating at two temperatures 20 °C and 50 °C. The influence of temperature on degradation kinetics of CBZ, BQM and BQD was studied. The results exhibited a notable difference in the catalytic behavior by varying temperature. The higher reactor temperature (50 °C) showed a higher activity of the catalysts but a lower concentration of dissolved ozone. Most of the catalysts exhibited higher removal rate for BQM and BQD compared to non-catalytic experiments in both temperatures. The Pd-H-Y-12-EIM catalyst illustrated a higher degradation rate of by-products at 50 °C compared to other catalysts.

Keywords: carbamazepine; ozone; zeolites; catalysts synthesis and characterization; catalytic ozonation

1. Introduction

The frequent appearance of pharmaceuticals as high as mg/L levels in the in ground water and surface waters has been reported in several studies during the last decades [1]. A notable attention has

been attracted due to their potential hazard effects on the aquatic ecosystem and human health [2,3]. An emerging concern exists of what exactly happens with the pharmaceutical contaminants in the aquatic environment. The origin of these compounds comes from the fact that they have been employed in several domains of the human activity, for example, human medication, veterinary purposes and aquaculture, as well as large concentrations of them leaking into the sea from pharmaceutical industries. Conventional wastewater treatment is not able to efficiently eliminate most of these pharmaceuticals from wastewaters, not to mention their degradation products [4,5].

Carbamazepine (5H-dibenzo (b,f) azepine-5-carboxamide, shortly CBZ) is a psychiatric pharmaceutical used for treatment of epilepsy and trigeminal neuralgia a chronic pain disorder [6]. CBZ was displayed in a list of essential medicine requirements for a basic health-care in the World Health Organization (WHO) Model List of Essential Medicines (March 2017) in the group of anticonvulsant and antiepileptic pharmaceuticals [7]. Only 28% of CBZ is metabolized by the human body, while the rest is excreted during urination. Before that, it is enzymatically transformed to 10, 11-epoxy-10, 11-dihydro-CBM, and from the hydrolysis of these intermediates, CBZ-diOH is produced. For this reason, CBZ-diOH was one the most abundant CBZ compounds detected in water [8]. CBZ is one of the commonly detected compounds in the effluents. It is resistant against biodegradation, and sometimes the concentration in the effluent has been larger than influent, perhaps due to the conjugates originating from the parent compounds, i.e., hydrolysis through biological treatment [9]. The CBZ and metabolite removal efficiency was −11–18% toward human waste treatment plants, −40% to 25% in the sewage treatment plants and −100–56% in hospital wastewater treatment plants. The concentration of CBZ in the influent and effluent samples were abnormal, this is due to the fact of the low removal rate of CBZ [8].

CBZ has been detected as good as everywhere in the Baltic Sea, in Northern Europe. However, owing to the long turnover time (a very long half-life time in the Baltic Sea, exceeding 3.5 years) and a low elimination rate of CBZ, the wastewater treatment plants exhibit negative removal efficiencies (for instance in Finland with a −41% removal efficiency in wastewater treatment plants). Consequently, it is estimated that more than 55 tons of CBZ has accumulated in the Baltic Sea [10]. CBZ has been detected in the surface water of Milan up to 100 ng/L concentration and it is most frequent drug found in Serbian rivers [11,12]. The research of German and Portuguese surface waters revealed that CBZ and its metabolites were detected to 5000 ng/L in the surface waters, which they were barely decomposed during the wastewater treatment [13].

Significant concentrations of CBZ and five of its metabolites have been detected in urban groundwater in the Spanish rivers Poble Sec and Besòs. Moreover, at the delta of Besòs restored via a river polluted through treated effluent from several treatment plants, CBZ and two of CBZ hydroxyl metabolites were not eliminated following those degrading conditions [14]. Moreover, CBZ was detected in Germany, in the form of the human metabolites, and transformation by-products of CBZ in the several groundwater springs, surface waters and treated wastewater. The genotoxicity of these compounds determined by the so-called silico method (distributed structure-searchable toxicity). These research results revealed that these contaminants have a potential hazard to mammalians, including human beings [15].

The presence of CBZ in the environment poses a potential risk to the aquatic life and human health. This has led to increasing attention to the elimination of CBZ compound through the wastewater treatment plants before discharge into the water basin [16–18]. Several methods have been proposed for the removal of CBZ from wastewaters, for instance, an adsorptive method utilizing biosynthesized hematite nanoparticles. This study did not eliminate the pollutants but instead they were accumulated and pollutants were transferred from aqueous solution to the adsorbent phase [19]. Some another studies concerning an activated sludge system consisting of a membrane bioreactor, the removal was rather low, around 35% due to of recalcitrance [20], or gamma irradiation coupled with microbiological treatment. With this technology, almost 99% of CBZ could be removed, as well as decreasing the TOC by 80%. However the treatment duration was 250 h, which is a quite long period [21]. Advanced oxidation

processes (AOP) have as well been applied for degradation of CBZ such as, radiation-induced activation of peroxymonosulfate, which was reported by Wang et al. [16]. In this investigation, nine intermediate products were detected, and the scientists observed that the limiting step for CBZ mineralization in the system was the decomposition of CBZ intermediates. Low mineralization and hazard intermediates were the biggest obstacles with most of the CBZ treatment trials in the study.

Ozonation has been proposed and applied as a method for removing pharmaceuticals from hospital wastewaters, both in a laboratory and pilot scale. In the laboratory scale, the removal has been successful [22]. Besides, ozonation as an additional treatment step in wastewater treatment has become generally acknowledge for eliminating pharmaceuticals and other micro-pollutants [23]. To improve the ozonation process, more research is needed to study the formation of hydroxyl radicals and the formation of dangerous degradation products of ozonation [9]. Ozonation of CBZ gives some resistant by-products due to the ozone reaction by the olefin group in CBZ, producing an ozonide, which divides the double bond [24]. The major identified by-products from ozonation of CBZ were BQM and BQD [25]. Some methods have been proposed to improve the ozonation of CBZ due to reducing the by-product such as combination by soil aquifer treatment column that enhances degradation of BQD yet the other by-products were more resistance up to 5–6 days [26].

Catalytic ozonation is recommended as an AOP for wastewater treatment, due to enhancing the removal efficiency and its potential to mineralize the organic compounds created. Catalysts improve the decomposition of ozone in the water to produce extremely active hydroxyl radicals [27,28]. Several studies have revealed that coupling ozonation to heterogeneous catalysis is very efficient in oxidizing pharmaceuticals from wastewater. For instance, ozonation combined with a granular activated carbon (GAC) filter can dramatically diminish the CBZ content and its human metabolites [15,29]. Zeolite catalysts exhibited an improvement in the ozonation of the pharmaceutical compound paracetamol [30] and ibuprofen [31]. Moreover, loading of the metals on zeolite catalysts increases the catalytic ozonation efficiency [32].

In the current work, non-catalytic and catalytic ozonation was employed to study the removal of CBZ and its by-products in aqueous solutions. The task is challenging because the degradation rates of the by-products are relatively low. A high concentration of CBZ (30 mg/L) was selected to study the kinetics of the by-products of the degradation. For this purpose, the main products were isolated, and their concentration was monitored with high performance liquid chromatography (HPLC). In order to optimize the degradation of the by-products, the catalysts Pt-MCM-41-IS, Ru-MCM-41-IS, Pd-H-Y-12-EIM, Pt-H-Y-12-EIM, Pd-H-Beta-300-EIM and Cu-MCM-41-A-EIM were used, at two different reaction temperatures. The catalysts were characterized with revealed methods to explain their activities in the experiments.

2. Results and Discussion

2.1. Physico-Chemical Characterization Results: Catalyst Structure and Surface Properties

2.1.1. Transmission Electron Microscopy

The TEM images of (a) Pt-MCM-41-IS, (b) Ru-MCM-41-IS, (c) Pd-H-Y-12-EIM, (d) Pt-H-Y-12-EIM, (e) Pd-H-Beta-300-EIM and (f) Cu-MCM-41-A-EIM catalysts and Pt, Ru, Pd and Cu particle size distributions presented in the form of histograms, are given in Figure 1a–f. The average metal particle size and the distributions were measured and counted from the TEM images, which are displayed in Table 1.

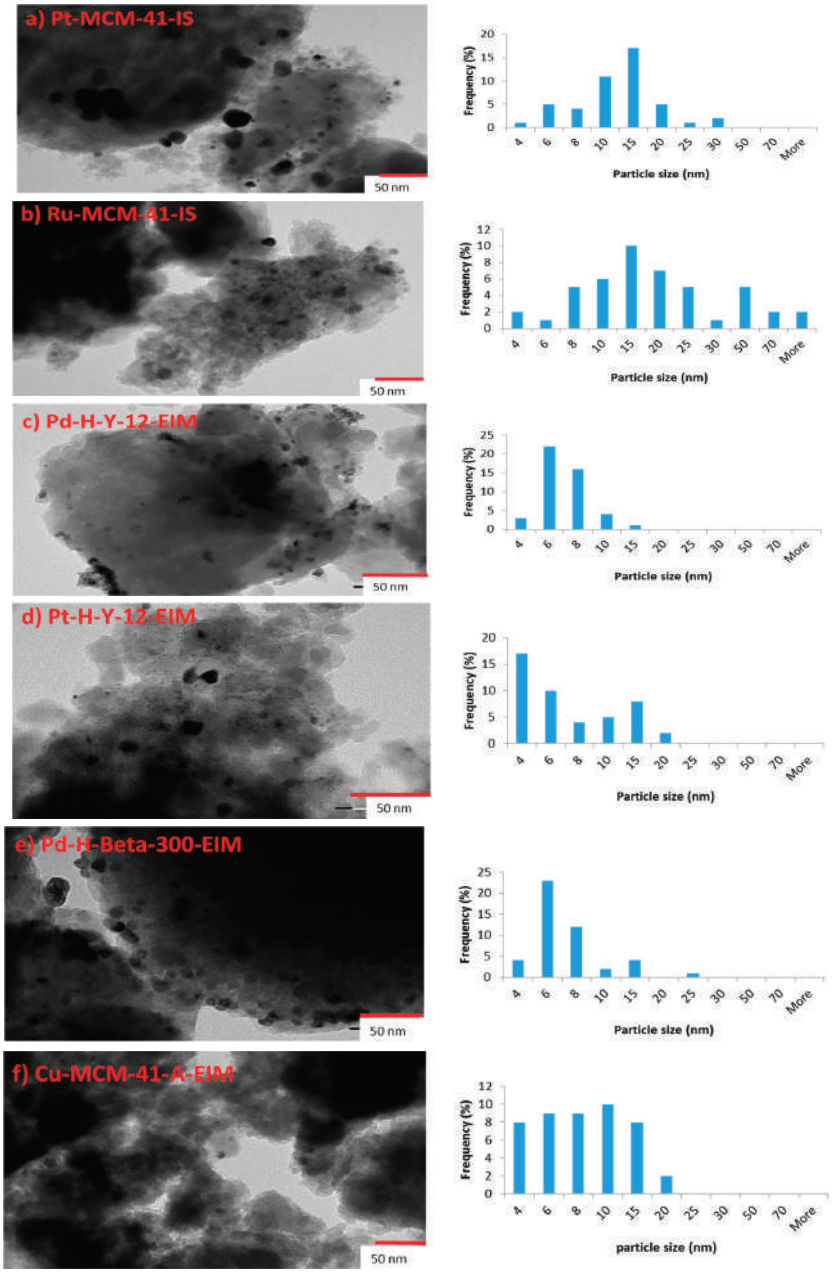

Figure 1. (**a**) TEM image and Pt particle size distribution histogram of Pt-MCM-41-IS, catalyst. (**b**) TEM image and Ru particle size distribution histogram of Ru-MCM-41-IS catalyst. (**c**) TEM image and Pd particle size distribution histogram of Pd-H-Y-12-EIM catalyst. (**d**) TEM image and Pt particle size distribution histogram of Pt-H-Y-12-EIM catalyst. (**e**) TEM image and Pd particle size distribution histogram of Pd-H-Beta-300-EIM catalyst. (**f**) TEM image and Cu particle size distribution histogram of Cu-MCM-41-A-EIM catalyst.

Table 1. Average cluster size distribution of Pt, Ru, Pd and Cu in the catalysts Pt-MCM-41-IS, Ru-MCM-41-IS, Pd-H-Y-12-EIM, Pt-H-Y-12-EIM, Pd-H-Beta-300-EIM and Cu-MCM-41-A-EIM.

Entry	Catalyst	Average Particle Size Distribution (nm)
1	Pt-MCM-41-IS	13.39
2	Ru-MCM-41-IS	13.29
3	Pd-H-Y-12-EIM	6.47
4	Pt-H-Y-12-EIM	5.72
5	Pd-H-Beta-300-EIM	6.11
6	Cu-MCM-41-A-EIM	7.82

The smallest average Pt particle sizes were measured for Pt-H-Y-12-EIM (5.72 nm), whereas the second smallest average Pd particle was measured for Pd-H-Beta-300-EIM (6.11 nm). The largest average particle size was observed for Pt-MCM-41-IS (13.395 nm). The mesoporous material Ru-MCM-41-IS catalyst synthesized also exhibited large average particles (13.29 nm).

It was concluded from the results of averages particle sizes (Table 1), that the method of introducing Pt-, Ru- into the mesoporous MCM-41 influenced the sizes of the particles. Hence, an in-situ method of introducing Pt- and Ru- resulted in large average particles sizes, once again confirming the significance of method of metal introduction in the MCM-41, mesoporous material.

For Cu-MCM-41-A-EIM, the mesoporous catalyst synthesized using the evaporation impregnation method, resulted in the average Cu particle size of 7.82 nm. Therefore, an introduction of metals (Pt-, Pd- and Cu-) using the evaporation impregnation method resulted in average smaller particle sizes.

2.1.2. Nitrogen Physisorption

The specific surface areas and specific pore volumes of fresh and spent Pt-, Ru and the Cu-MCM-41 mesoporous catalyst and Pd- and Pt-H-Y-12 catalysts were measured using nitrogen physisorption and results are collected in Table 2. The lowest specific surface area was obtained for the fresh Pt-MCM-41-IS (429 m^2/g) catalyst and this value increased after the catalyst had been used. The highest specific surface areas were determined for Pt-H-Y-12-EIM (857 m^2/g) and Pd-H-Beta-300-EIM (808 m^2/g).

Table 2. Specific surface area and pore volume of Pt-MCM-41-IS, Ru-MCM-41-IS, Pd-H-Y-12-EIM, Pt-H-Y-12-EIM, Pd-H-Beta-300-EIM and Cu-MCM-41-A-EIM catalysts applied in the experiments.

Entry	Catalyst	Specific Surface Area (m^2/g)		Pore Specific Volume (cm^3/g)	
		Fresh	Spent	Fresh	Spent
1	Pt-MCM-41-IS	429	555	0.409	0.552
2	Ru-MCM-41-IS	747	677	0.491	0.456
3	Pd-H-Y-12-EIM	667	732	0.237	0.259
4	Pt-H-Y-12-EIM	857	344	0.304	0.506
5	Pd-H-Beta-300-EIM	808	657	0.287	0.233
6	Cu-MCM-41-A-EIM	612	104	0.765	0.314

2.1.3. Scanning Electron Microscopy

The morphology, size and shape of the catalysts crystals were analyzed by scanning electron microscopy (SEM). The scanning electron micrographs of the Pt-MCM-41-IS, Ru-MCM-41-IS, Pd-H-Y-12-EIM, Pt-H-Y-12-EIM, Pd-H-Beta-300-EIM and Cu-MCM-41-A-EIM catalysts studied in the removal of CBZ from aqueous solutions exhibited a crystal morphology similar to that of H-MCM-41, H-Y-12 and H-Beta-300 catalyst, prior to their modifications with Pt-, Ru-, Pd- and Cu-metals. The crystal size distribution of the (a) Pt-MCM-41-IS, (b) Ru-MCM-41-IS, (c) Pd-H-Y-12-EIM, (d) Pt-H-Y-12-EIM, (e) Pd-H-Beta-300-EIM and (f) Cu-MCM-41-A-EIM in the form of histograms are displayed in Figure 2a–f. The average size of the catalyst crystals is presented in the Table 3. The largest average crystal size (272.45 nm) was obtained for the Pd-H-Beta-300-EIM synthesized

using evaporation impregnation. The second largest average crystal size measured for Pd-H-Y-12-EIM (257.12 nm) synthesized by using evaporation impregnation. The third largest average crystal size was measured for Pt-MCM-41-IS (219.23), prepared by the in-situ method. The explanation for the variations in the crystal sizes for synthesized catalysts is the structures of the H-Beta-300, H-Y-12 and MCM-41 mesoporous materials. Furthermore, the methods of the Pt-, Ru-, Pd- and Cu- introduction and the synthesis conditions can influence the average crystal size. The smallest crystal size (88.23 nm) was obtained for Cu-MCM-41-A-EIM, the catalyst synthesized using the evaporation impregnation method.

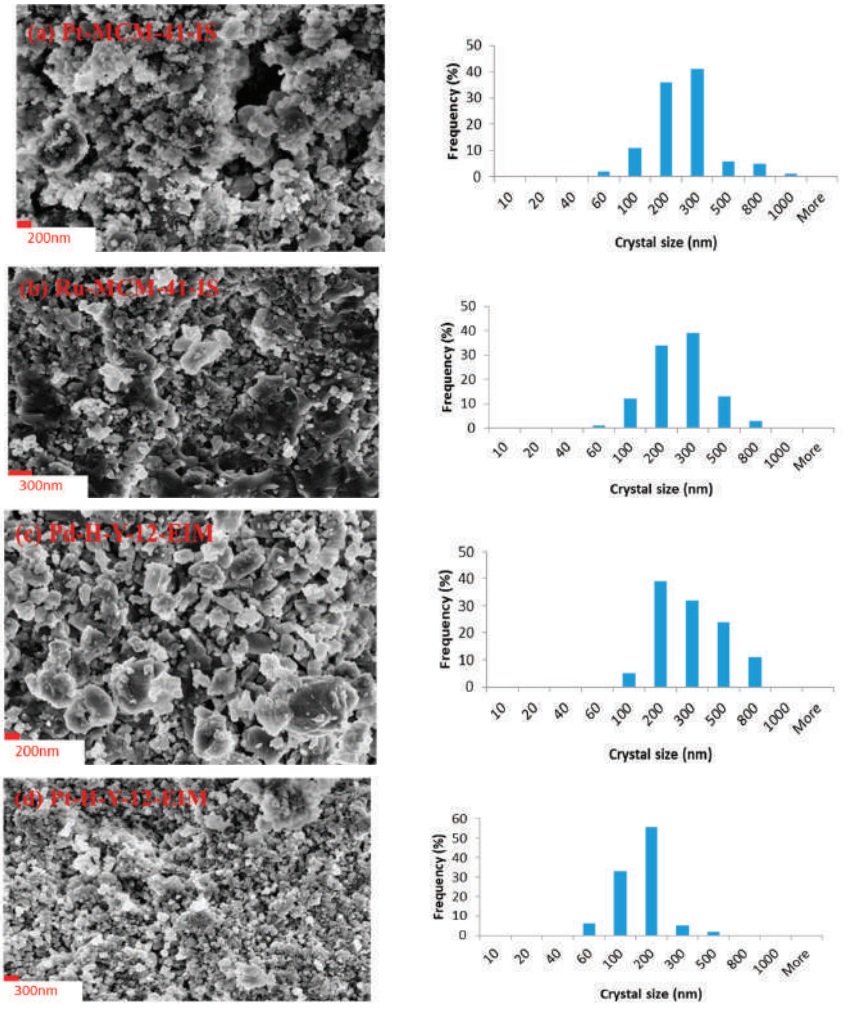

Figure 2. *Cont.*

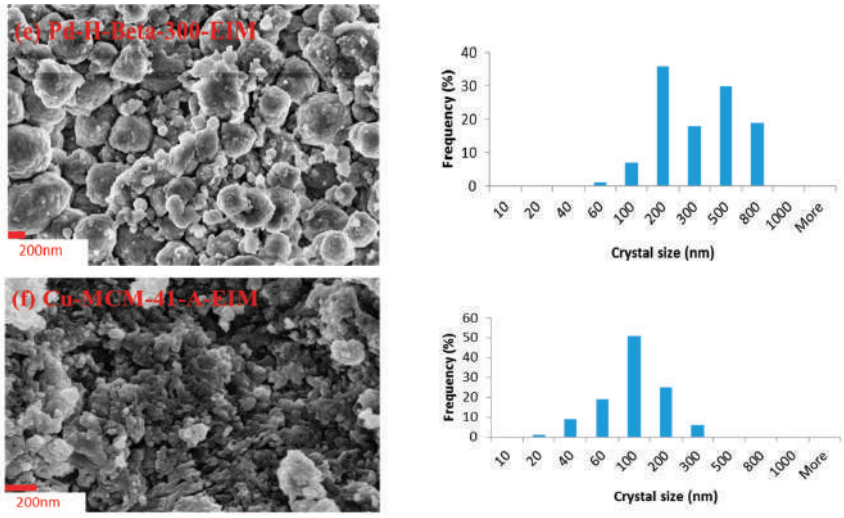

Figure 2. SEM image and crystal size distribution histogram of (**a**) Pt-MCM-41-IS. (**b**) Ru-MCM-41-IS catalyst. (**c**) Pd-H-Y-12-EIM. (**d**) Pt-H-Y-12-EIM. (**e**) Pd-H-Beta-300-EIM and (**f**) Cu-MCM-41-A-EIM catalysts.

Table 3. Average crystal size and metal (Pt, Ru, Pd and Cu) content of Pt-MCM-41-IS, Ru-MCM-41-IS, Pd-H-Y-12-EIM, Pt-H-Y-12-EIM, Pd-H-Beta-300-EIM and Cu-MCM-41-A-EIM catalysts.

Entry	Catalyst	Average Crystal Size (nm)	Metal Concentration (wt%)
1	Pt-MCM-41-IS	219.23	7.12
2	Ru-MCM-41-IS	202.39	1.55
3	Pd-H-Y-12-EIM	257.12	5.34
4	Pt-H-Y-12-EIM	119.62	1.67
5	Pd-H-Beta-300-EIM	272.45	1.95
6	Cu-MCM-41-A-EIM	88.23	3.46

2.1.4. Energy Dispersive X-ray Microanalysis

The Pt, Ru, Pd and Cu contents inside the Pt-MCM-41-IS, Ru-MCM-41-IS, Pd-H-Y-EIM, Pt-H-Y-12-EIM, Pd-H-Beta-300-EIM and Cu-MCM-41-A-EIM catalysts are given in Table 3. The highest amount of Pt was found for the Pt-MCM-41-IS catalyst. The largest amount of metal content (Pt) 7.12 wt% was measured for Pt-MCM-41-IS catalyst synthesized using the in situ method (Table 3). The Pd-H-Y-12-EIM catalyst synthesized using the evaporation method exhibited second highest metal (Pd) content 5.34 wt% Cu metal content (Table 3).

2.1.5. Pyridine Adsorption-Desorption with FTIR Spectroscopy

The concentration of Brønsted at 1545 cm^{-1} and Lewis at 1450 cm^{-1} acid sites were measured with FTIR using pyridine as a probe molecule. At 250–350 °C, pyridine desorption demonstrate weak, medium and strong sites, whereas at 350–450 °C it exhibited medium and strong sites and finally at 450 °C, strong sites prevailed. The acidity of the Pt-MCM-41-IS, Ru-MCM-41-IS, Pd-H-Y-12-EIM, Pt-H-Y-12-EIM, Pd-H-Beta-300-EIM and Cu-MCM-41-A-EIM catalysts analyzed via FTIR is listed in Table 4. Following that, the data of the determination were converted into concentrations using the extinction coefficients of Emeis [33]. It was noticed that Pd-H-Y-EIM showed the presence of largest Brønsted acidity (237 μmol/g) at 250 °C compared to other catalyst. The catalysts Cu-MCM-41-EIM and

Pd-H-Y-12-EIM catalysts had higher Lewis acidities (56 μmol/g and 52 μmol/g) at 250 °C, compared to the other catalysts.

Table 4. Brønsted and Lewis acidities of Pt-MCM-41-IS, Ru-MCM-41-IS, Pd-H-Y-12-EIM, Pt-H-Y-12-EIM, Pd-H-Beta-300-EIM and Cu-MCM-41-A-EIM catalysts.

Catalysts	Brønsted Acidity (μmoL/g)			Lewis Acidity (μmoL/g)		
	250 °C	350 °C	450 °C	250 °C	350 °C	450 °C
Pt-MCM-41-IS	7	2	0	1	1	0
Ru-MCM-41-IS	18	0	0	9	0	0
Pd-H-Y-12-EIM	237	24	0	52	6	0
Pt-H-Y-12-EIM	96	28	0	3	13	0
Pd-H-Beta-300-EIM	58	18	0	9	7	0
Cu-MCM-41-A-EIM	44	10	0	56	9	0

2.1.6. Characterization by X-ray Photoelectron Spectroscopy

The surface composition and oxidation state of metals were determined by the X-ray photoelectron spectroscopy (XPS) method. The XPS analysis indicated the oxidation states of Pt° and PtO on the Pt-MCM-41-IS catalyst (Figure 3a) Similarly oxidation state of Pt in the Pt-H-Y-12-EIM was measured as Pt, PtO_2 (Figure 3d). The oxidation states of Ru in Ru-MCM-41-IS was determined as Ru° and RuO_2 (Figure 3b). The oxidation states of Pd in Pd-H-Y-12-EIM and Pd-H-Beta-300-EIM were measured to be Pd° (Figure 3c,e). The oxidation state of Cu in Cu-MCM-41-A-EIM was measured to be Cu° and CuO (Figure 3f).

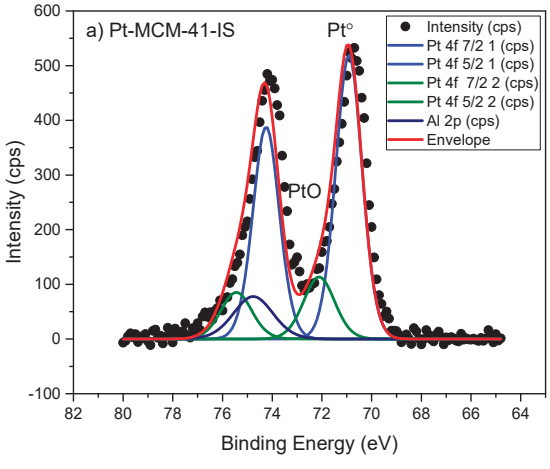

Figure 3. *Cont.*

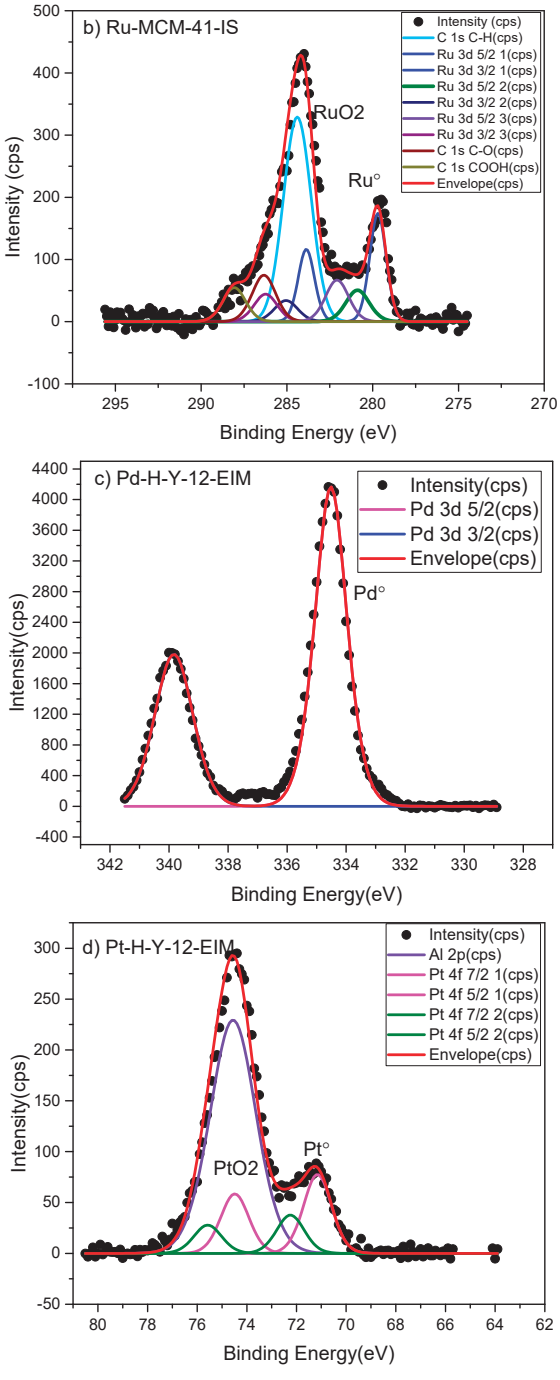

Figure 3. *Cont.*

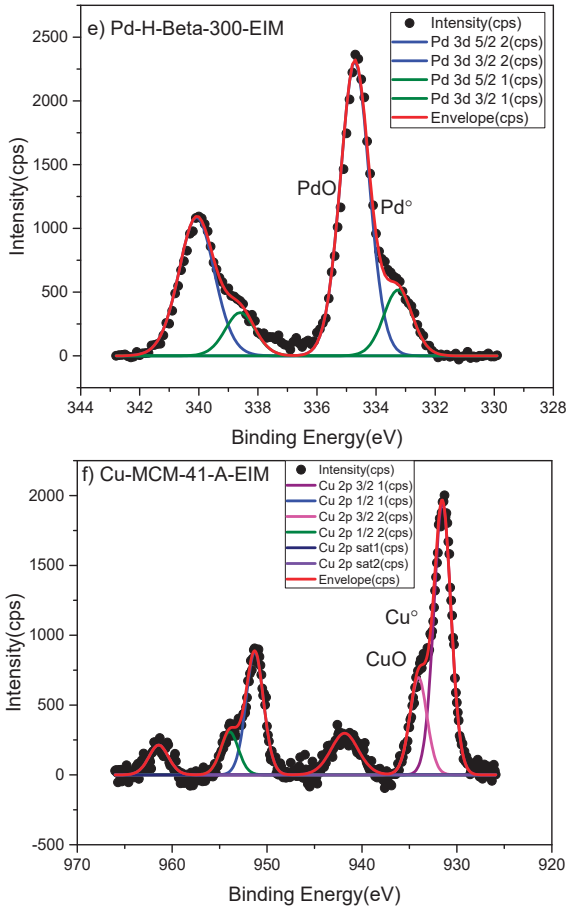

Figure 3. X-ray photoelectron spectroscopy (XPS) spectra of (**a**) Pt-MCM-41-IS, (**b**) Ru-MCM-41-IS, (**c**) Pd-H-Y-12-EIM, (**d**) Pt-H-Y-12-EIM, (**e**) Pd-H-Beta-300-EIM and (**f**) Cu-MCM-41-A-EIM catalysts.

2.2. *Non-Catalytic and Catalytic Ozonation of Carbamazepine*

2.2.1. Influence of Different Catalysts in the Degradation of Carbamazepine and its By-Products in the Presence of Ozone

The influence of different temperatures (5 °C, 20 °C and 50 °C) on the ozonation of CBZ on the reaction rate was evaluated the results are displayed in Figure 4a. These experiments illustrate that the transformation rate of CBZ was rapid and approximately equal to each other, at these three temperatures. After 5 min of ozonation, all the CBZ was transformed. Somathilake et al. obtained similar results from the ozonation of CBZ [34]. The degradation kinetics of CBZ by 0.5 g/L of Pd-H-Beta-300-EIM was studied in the absence and presence of ozone (Figure 4b). This experiment revealed that the CBZ concentration did not change in the absence of ozone, which indicates that the catalyst does not absorb CBZ and it is not transformed without the presence of ozone.

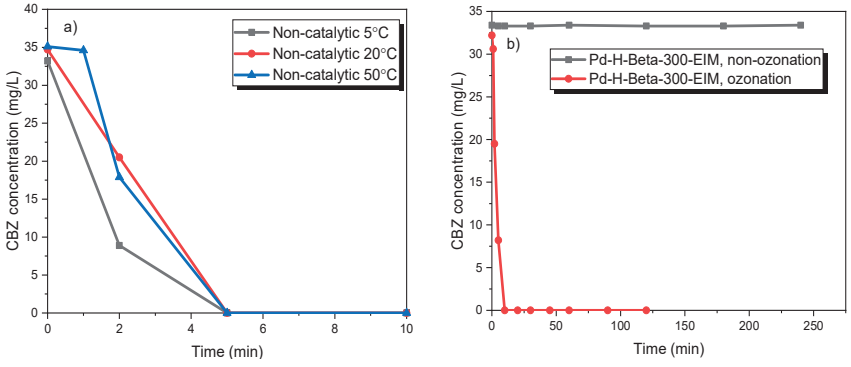

Figure 4. (**a**) CBZ degradation by ozonation at different temperatures (5 °C, 10 °C, 20 °C and 50 °C). (**b**) CBZ degradation by catalysis in the presence and absence of ozone at temperature 20 °C (stirring speed = 900 rpm, $C_{O3,g}$ = 21 mg/L, C_{CBZ} = 35 mg/L, gas flow rate = 110 mL/min, $C_{catalysts}$ = 0.5 g/L).

An identical series of catalytic ozonation experiments were conducted at 20 °C in order to evaluate the effect of different heterogeneous catalysts on the degradation rate of CBZ. Figure 5a shows that Cu-MCM-41-A-EIM and Ru-MCM-41-IS showed higher degradation rates compared to other catalysts the conversion of CBZ was complete already after two minutes for the Cu-catalyst and the Ru-catalyst was almost as active.

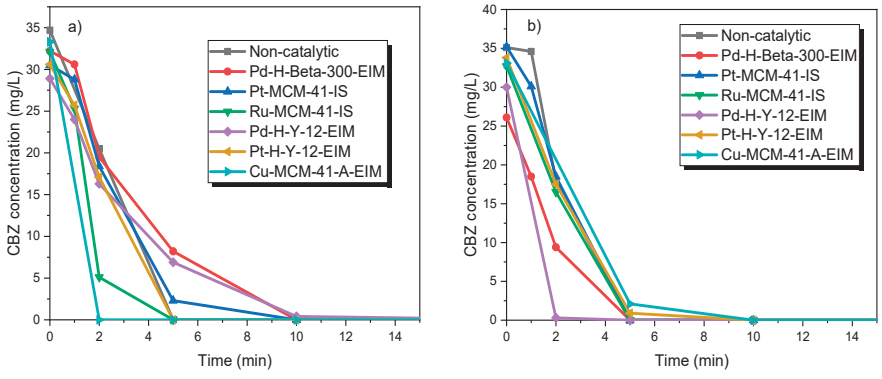

Figure 5. CBZ degradation by ozonation and ozonation combined with catalysis. C_{CBZ} = 35 mg/L, gas flow rate = 110 mL/min, stirring speed = 900 rpm, $C_{O3,\,g}$ = 21 mg/L, $C_{\,catalysts}$ = 0.5 g/L. (**a**) T = 20 °C and (**b**) T = 50 °C.

A similar series of catalytic ozonation experiments were carried out at 50 °C, to evaluate the effect of increased temperature on the catalyst activity while ozonating CBZ (Figure 5b). As revealed in our previous work, the dissolved ozone concentration decreases at higher temperature but, on the other hand, the activity of catalysts increases at higher temperature [31,35]. Here, the Pd-H-Y-12-EIM and Pd-H-Beta-300-EIM illustrated the highest decomposition rate compared to other catalysts and the non-catalytic experiment. Due to the rapid reaction rate, it is hard to evaluate the temperature effect on decomposition rate of CBZ.

2.2.2. Quantification of Catalytic and Non-Catalytic Ozonation Products

Han et al. studied [36] cytotoxicity and genotoxicity of the removal CBZ through chlorination, chloro-amination and ozonation processes. The CBZ solely induces chromosomal damage, and on the other hand, the genotoxicity of the CBZ residues after each treatment was found to be higher. Moreover,

it was demonstrated that the most efficient way for the degradation of CBZ was by ozonation among the other treatments. However, the by-products formed by ozonation exhibited the highest cytotoxicity and an elevated genotoxicity. The authors suspected that the by-products BQM and BQD might cause chromosomal damage effects.

The main ozonation pathway of CBZ is a rapid, almost instantaneous reaction leading to BQM (Figure 6). BQM is transformed further slowly to BQD [37]. In order to investigate the effect of heterogeneous catalysts on the formation and transformation of BQM and BQD, the products were isolated from the kinetic experiments and a quantification method was developed.

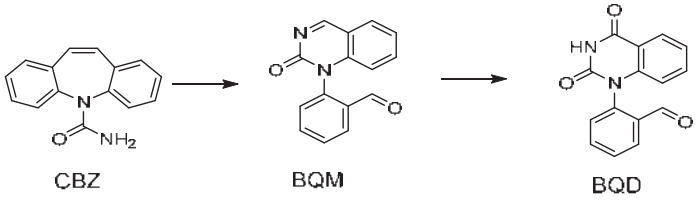

Figure 6. CBZ and its main ozonation products.

The temperature effect on the formation of by-products was also studied for the non-catalytic ozonation using the same temperatures as above. The influence of the reactor temperature on the ozonation of CBZ into BQM and BQD is illustrated in Figure 7. It can be noticed that at higher temperature (50 °C), the concentration of BQM remained at a high level and after 4 h it had only decreased to 19.5 mg/L from the highest value of 28 mg/mL. At lower temperatures (20 °C and 5 °C), the reaction proceeded more rapidly, and almost all of BQM was removed or transformed after four hours. The concentration of the secondary by-product BQD increased simultaneously to 20–24 mg/L when performing the experiments at low temperature (5–20 °C), but it remained low at the higher temperature (50 °C), due to a slow transformation of BQM, BQD formed slower at higher temperatures. If the experiment at 50 °C had been continued, the concentration of BQD might have been the same as for the experiments at lower temperatures. It can be concluded that by lowering the temperature due to higher dissolved ozone concentration, CBZ rapidly converts to BQM, and later on it transforms to BQD faster than at the higher temperature (50 °C).

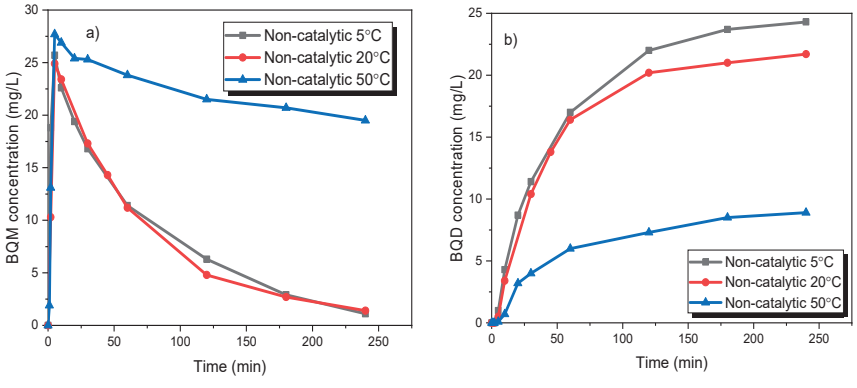

Figure 7. (**a**) BQM and (**b**) BQD concentration during the ozonation of CBZ. C_{CBZ} = 35 mg/L, gas flow rate = 110 mL/min, T = 5 °C, 10 °C, 20 °C and 50 °C, stirring speed = 900 rpm, $C_{O3,\,g}$ = 21 mg/L.

Thereafter, several solid catalysts, which were synthesized and characterized by our group, were employed to reveal the catalytic effect on the CBZ. The formation kinetic of BQM and BQD are displayed in Figures 8 and 9. It was observed that during the first minutes of experiments, the BQM

concentration increased to a maximum 25.7 mg/L (Cu-MCM-41-A-EIM), later on it decreased in 2 h to a minimum of 4 mg/L. For non-catalytic ozonation at 20 °C, the BQM concentration increased to 25.7 mg/L but after 2 h it decreased to 4.8 mg/L. Pt-H-Y-12-EIM and Ru-MCM-41-IS catalysts showed a slightly higher transformation rate of BQM compared to the corresponding non-catalytic experiment. As revealed by Figure 9, BQD was slightly formed within 2 h. The maximum concentration of BQD was 20.2 mg/L for non-catalytic experiment. The catalyst Pd-H-Y-12-EIM showed the lowest BQD concentration (1.7 mg/L) also Pd-H-Beta-300 showed lower formation of BQD (11.9 mg/L). Three mechanisms could occur in these experiments, (1) ozone adsorption on the catalyst surface and generation of active radical species that react with BQM and BQD; (2) BQM and BQD sorption on the catalyst surface followed via the reaction by dissolved ozone in the water and (3) sorption of all three species ozone, BQM and BQD on the catalyst surface followed by a direct or indirect reaction [38].

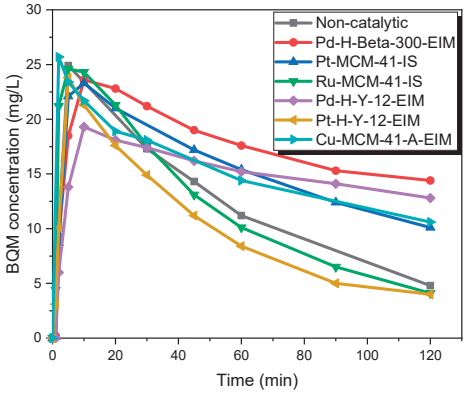

Figure 8. BQM concentration during the catalytic and non-catalytic ozonation of CBZ. C_{CBZ} = 35 mg/L, gas flow rate = 110 mL/min, T = 20 °C, stirring speed = 900 rpm, $C_{O3,g}$ = 21 mg/L, $C_{catalysts}$ = 0.5 g/L.

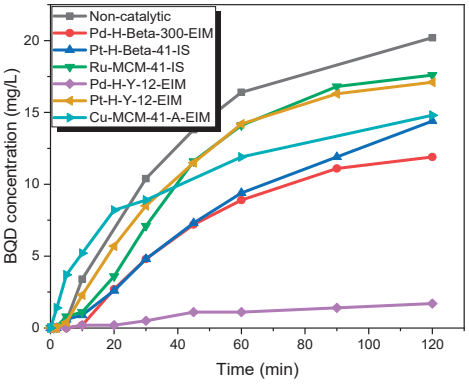

Figure 9. BQD concentration during the catalytic and non-catalytic ozonation of CBZ. C_{CBZ} = 35 mg/L, gas flow rate = 110 mL/min, T = 20 °C, stirring speed = 900 rpm, $C_{O3,g}$ = 21 mg/L, $C_{catalysts}$ = 0.5 g/L.

The catalytic experiments were carried out under several temperatures. Figure 10 shows that in the first minutes, 27.7 mg/L of BQM was formed (similar to non-catalytic ozonation), but later on, the BQM concentration slightly decreased to 9 mg/L when using the Pd-H-Y-12-EIM catalyst. For non-catalytic ozonation at 50 °C, the BQM concentration increased to 27.7 mg/L, after which it decreased to 21.4 after 2 h, and after 4 h it had decreased to 19 mg/L. It can be noticed from results that the activity of catalyst increased with higher temperature, since dissolved ozone concentration is

very low at 50 °C (approximately five times lower than at 20 °C). For example, after 2 h of ozonation combined with Pd-H-Y-12-EIM catalyst, the BQM and BQD concentration were 11.2 mg/L and 0.9 at 50 °C, which were lower compared to 20 °C (BQM concentration was 12.8 mg/L and BQD concentration was 1.7 mg/L) with the same catalyst (Figure 11). One explanation for the increased catalytic efficiency at higher temperatures could be due to that instead of ozonation, catalytic oxidation is observed, where dissolved oxygen is adsorbed on metal oxides and the further generate active atomic oxygen species as well as lattice oxygen atoms, which are present on the metal oxides of catalysts [39].

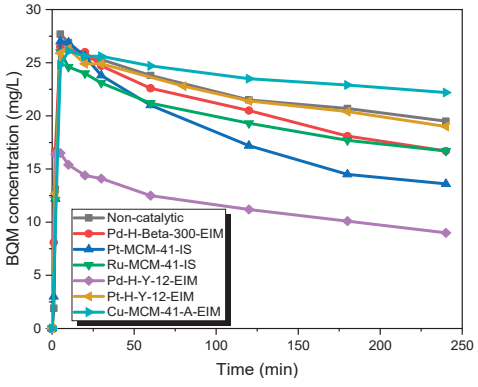

Figure 10. BQM concentration during the catalytic and non-catalytic ozonation of CBZ. C_{CBZ} = 35 mg/L, gas flow rate = 110 mL/min, T = 50 °C, stirring speed = 900 rpm, $C_{O3,g}$ = 21 mg/L, $C_{catalysts}$ = 0.5 g/L.

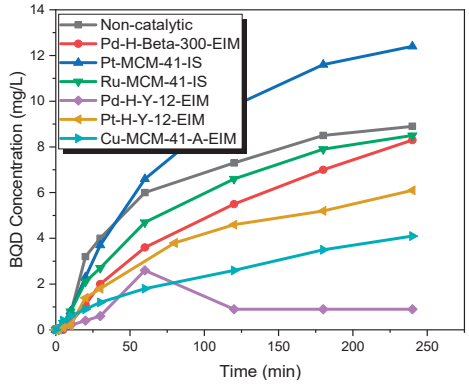

Figure 11. BQD concentration during the catalytic and non-catalytic ozonation of CBZ. C_{CBZ} = 35 mg/L, gas flow rate = 110 mL/min, T = 50 °C, stirring speed = 900 rpm, $C_{O3,g}$ = 21 mg/L, $C_{catalysts}$ = 0.5 g/L.

These results were in line with a study performed by Rosal et al. who investigated catalytic ozonation of CBZ. Their ozonation results revealed that utilizing a titanium dioxide catalyst combined with ozonation provides a significant benefit where the ozone decomposition as well as ozonation reactions were improved, as well as an increase of the formation of hydroxyl radicals and rate of mineralization compared to non-catalytic ozonation [40].

A more detailed investigation of the fate of BQD was conducted using isolated BQD without CBZ and other by-products. Pure BQD was obtained by isolation from an ozonation experiment. BQD was dissolved in acetonitrile and deionized water. Non-catalytic and catalytic ozonation was carried out with this solution. Figure 12 demonstrates that after 4 h of non-catalytic ozonation only 6% of BQD

remained and after 4 h catalytic ozonation only 3% of BQD, catalytic ozonation slightly increased transformation rate.

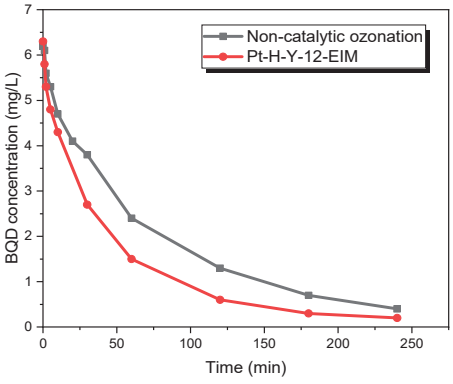

Figure 12. BQD concentration during the catalytic and non-catalytic ozonation of BQD. C_{BQD} = 6 mg/L, $C_{Acetonitrile}$ = 6 mg/L, gas flow rate = 110 mL/min, T = 50 °C, stirring speed = 900 rpm, $C_{O3,g}$ = 21 mg/L, $C_{catalysts}$ = 0.5 g/L.

2.2.3. Leaching of Modified Metals and Aluminum from Catalysts

Inductively coupled optical emission spectrometry (ICP-OES) Optima 5300 DV Perkin Elmer instrument was applied to determine leaching of catalytic metals during ozonation at 20 °C. The aluminum and modified metal were considered in these experiments. Cu-MCM-41A-EIM catalyst showed high leaching of Cu 58.9% and Pd-H-Beta-300-EIM relatively high leaching of Pd and aluminum 14.2% and 20.26% respectively. On the contrary, Pt-H-Y-12-EIM, Ru-MCM-41-IS, Pt-MCM-41-IS showed no leaching for modified metal. Figure 13 illustrates the catalyst leaching during 2 h ozonation.

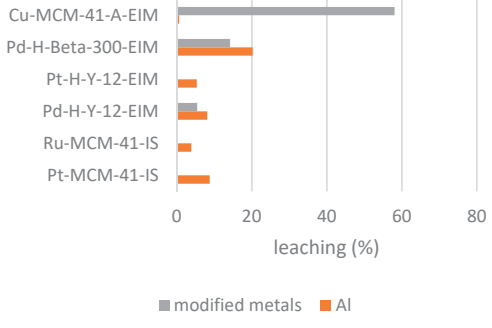

Figure 13. Leaching of modified metal and aluminum (%) in the catalytic ozonation of CBZ at 20 °C.

3. Materials and Methods

3.1. Chemicals

Carbamazepine (CBZ; $C_{15}H_{12}N_2O$, MW: 236.269 g/mol, CAS number: 298-46-4) was purchased from Sigma Life Science. The CBZ was in crystal powder form, therefore it was first dissolved in methanol (H_3COH, MW: 32.04 g/mol, CAS number: 67-56-1), which was obtained from VWR (Briare, France). The water used in the LC-MS analysis was purified using a Millipore Simplicity 185 system (Millipore S.A.S., Molsheim, France). The acetonitrile used in the LC-MS analysis was of LC-MS grade

and was obtained from Fisher scientific and formic acid was obtained from Sigma-Aldrich. BQM and BQD were prepared from ozonation following to the procedure Kråkström et al. Stock solutions of BQM and BQD were prepared in acetonitrile.

3.2. Catalyst Preparation

The following solid catalysts were prepared in our laboratory: Pt-MCM-41-IS, Ru-MCM-41-IS, Pd-H-Y-12-EIM, Pt-H-Y-12-EIM, Pd-H-Beta-300-EIM and Cu-MCM-41-A-EIM. The Pt and Ru modification of Pt-MCM-41-IS and Ru-MCM-41-IS was carried out using the in-situ (IS) synthesis preparation method [41]. The modification methods for Pd, Pt and Cu used for the synthesis of Pd-H-Y-12-EIM, Pt-H-Y-12-EIM, Pd-H-Beta-300-EIM and Cu-MCM-41-A-EIM catalysts were evaporation impregnation (EIM) [31].

For the synthesis of Pd-H-Y-12-EIM, an aqueous solution of $Pd(NO_3)_2$ and H-Y-12 was placed in a Rotavapor for 24 h, until the aqueous phase was evaporated at 60 °C. The Pd-H-Y-12-EIM catalyst was transferred from the flask and dried in an oven overnight at 100 °C. Finally, it was calcined in a muffle oven at 450 °C for three hours.

3.3. Physico-Chemical Characterization of Catalyst

The electron micrographs, metal particle size and structural properties of the catalysts were investigated by transmission electron microscopy (TEM, model JEM 1400 plus: Jeol Ltd., Tokyo, Japan) using a transmission electron microscope (model JEM 1400 Plus), using 120 kV accelerating voltage and a resolution of 0.38 nm provided via OSIS Quemesa 11 Mpix digital camera (rephrase/split). The specific surface areas and pore volumes of the catalysts were determined by nitrogen physisorption (Carlo Erba Sorptomatic 1900, Fisons Instruments, Milan, Italy) and interpreted with Dubinin and B.E.T. (Brunauer–Emmett–Teller) equations. The fresh catalysts were outgassed at 150 °C, whereas the spent catalysts were outgassed at 100 °C for 3 h before each and every nitrogen adsorption measurement. Scanning electron microscopy coupled to energy disperse X-ray analysis (SEM/EDXA) was used to investigate morphology. Crystallite size and metal contents of catalysts was analyzed by SEM (Zeiss Leo Gemini 1530, Oberkochen, Germany) and energy dispersive X-ray micro-analysis. The catalyst acidities were measured by Fourier transform infrared spectroscopy (FTIR) spectroscopy (ATI Mattson Infinity series, Madison, MI, USA) by employing pyridine as the probe molecule. The X-ray photoelectron spectroscopy (XPS, Kratos Analytical, UK) analysis was performed using an X-ray spectrometer (lens mode hybrid resolution by mono aluminum). The specific elemental analysis was done using 20 eV pass energy.

3.4. Kinetic Experiments in a Semi-Batch Reactor

The ozonation experiments were conducted in a double jacket isothermal glass reactor operating in semibatch mode. In order to immobilize the solid catalyst used in these experiments, a Spinchem ^{TM} rotating bed reactor (RBR) was used, typically operating at 900 rpm to ensure vigorous mixing of the liquid and gas phases and to maximize the mass transfer between the gas–liquid interface and the solid catalyst surface. An ozone generator (Absolute Ozone, Nano model, Edmonton, AB, Canada) was used to provide ozone, using oxygen (108.5 mL/min) and nitrogen (1.5 mL/min) as the gas flow rate to the generator was, so the total gas flow was 110 mL/min. The feed gas was super-dried (dew point −60 °C). The ozonator produced a concentration of approximately 21 mg/L of ozone in the gas phase. The ozone concentration was determined by iodine volumetric titration [42]. In order to purge the gas constantly through the reactor vessel, a 7 μm disperser was used at the bottom of the reactor. The dissolved ozone concentration was determined to 1.668 mg/L at 5 °C, 0.441 mg/L at 20 °C and 0.0921 mg/L at 50 °C by the indigo method. The water solubility of CBZ is rather low, only 17.7 mg/L, while it is fully soluble in methanol. Therefore, the stock solution was prepared by dissolving 0.35 g CBZ in 100 mL of methanol. Thereafter, 10 mL of the stock solution was added to 1 L deionized water in the glass reactor in the beginning of each experiment. The initial concentration of CBZ was thus 35 mg/L, which is higher than

the concentration typically detected in surface waters. However, a high initial concentration allows us to detect and identify by-products of very low concentrations. In this study, the reaction time was varied from 180 to 240 min. The reactor system used in the experiments is displayed in Figure 14.

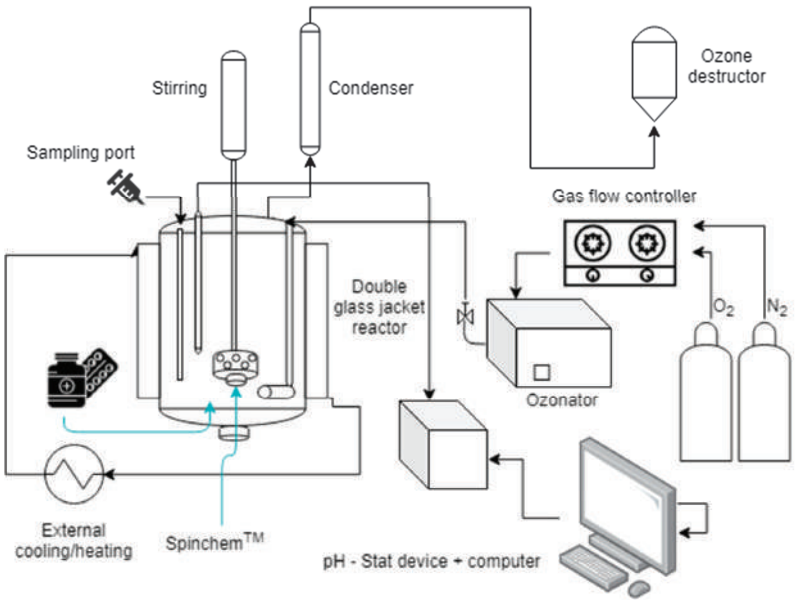

Figure 14. Schematic view of the semi-batch reactor system for degradation of CBZ.

3.5. Quantification of CBZ, BQM and BQD

Various systems have been developed for the analysis and determination of CBZ such as liquid chromatography-mass spectrometry (LC-MS) and gas chromatography-mass spectrometry (GC-MC) [43,44]. For quantification, an Agilent 1100 LC system equipped with a variable wavelength detector set to 254 nm was used. The chromatographic separation was performed using an Agilent 1100 binary pump equipped with a vacuum degasser, an autosampler and a thermostated column oven set to 30 °C and a Waters Atlantis T3 C18 column (2.1 × 100 mm, 3 µm). The eluents were 0.1% formic acid in water (A) and 0.1% formic acid in acetonitrile (B). Initially the composition was held at 0% (B) for 1 min, then the composition was increased linearly to 30% (B) over 9 min. The composition was further increased linearly to 95% (B) over 14 min. Finally, the eluent composition was returned to the initial conditions over the next 1 min and given 10 min for equilibration. The flow rate was 0.3 mL/min. The injection volume was 30 µL. The draw speed was 100 µL/min while the eject speed was 100 µL/min. Using the stock solutions, calibration curves consisting of eight points (in water) were prepared separately for CBZ, BQM and BQD. The ozonated samples were analyzed without any further adjustment.

An MSD ion trap mass spectrometer equipped with an electrospray ionization (ESI) source operating in full scan mode was used for confirmation of the structure. Nitrogen was used as drying gas and argon was used as collision gas. The drying gas was held at 8 L/min and heated to 350 °C. The nebulizer pressure was set to 40 psi. The scan range was set to 50–600 m/z.

4. Conclusions

The current work demonstrated the degradation kinetics of CBZ by ozonation at two reaction temperatures (20 °C and 50 °C), and a number of zeolite catalysts. Pt-MCM-41-IS,

Ru-MCM-41-IS, Pd-H-Y-12-EIM, Pt-H-Y-12-EIM, Pd-H-Beta-300-EIM and Cu-MCM-41-A-EIM catalysts were synthesized and applied with combination of ozone for the removal of CBZ and its ozonation transformed products. Several experiments were carried out in order to evaluate the influence of temperature on the catalyst activity. By increasing the reactor temperature to 50 °C the activities of the catalysts increased, even though the dissolved ozone concentration decreased dramatically at 50 °C compared to 20 °C. The formation of the products BQM and BQD were kinetically displayed and the role of the catalysts were discussed. CBZ rapidly transformed into BQM and later into BQD. The by-product analysis illustrated that degradation of BQM and BQD was higher when using a catalyst combined with ozonation. In addition, Pd-H-Y-12-EIM prepared by evaporation impregnation method revealed the highest degradation rate of BQM and BQD compared to other catalysts at 50 °C. The catalyst Pd-H-Y-12-EIM had the highest Brønsted acidity 237 μmol/g at 250 °C and moderately high Lewis acidity 52 μmol/g at 250 °C. This indicates that the acidity of catalyst has a big role in the transformation of CBZ. Moreover, this catalyst had a high average crystal size, 257.11 nm, compared to the other catalysts, and the Pd concentration was relatively large, 5.34 wt%. The leaching was relatively low for Pd and Al for this catalyst, which makes it a promising catalyst for the ozonation of pharmaceuticals of this kind.

Author Contributions: M.K. and S.S. are Ph.D. students, senior scientists and supervisors with the following competences: P.T.: ozonation technology, N.K.: catalyst specialist, K.E.: reactor design, T.S.: chemical kinetics and experimental planning, J.-P.M.: stirrer expert, L.K.: analysis of organic components in aqueous environment, P.E.: organic reaction technology, M.P.: TEM expert, A.A.: FTIR expert, A.S.: XPS expert. All authors have read and agreed to the published version of the manuscript.

Funding: This work is a part of the activities of the Johan Gadolin Process Chemistry Åbo Akademi University. Financial support from the from Svenska Litteratursällskapet (SLS, Helsinki, Finland), Centre for International Mobility (CIMO, Helsinki, Finland) and Tekniikan Edistämissäätiö (TES) is gratefully acknowledged. SpinChem™ AB is acknowledged for providing the RBR equipment used in this work. The Bio4Energy program and Wallenberg Wood Science Center in Sweden are acknowledged. The foundation Walter och Lisi Wahls Stiftelse för naturvetenskaplig forskning is acknowledged for funding the purchase of the ozonator device.

Conflicts of Interest: The authors declare no competing financial interest.

References

1. Ying, G.-G.; Jiang, Y.-X.; Yang, Y.-Y.; Yao, L.; Zhang, J.-N.; Liu, W.-R.; Zhao, J.-L.; Zhang, Q.-Q.; Liu, Y.-S.; Hu, L.-X. Pharmaceuticals and personal care products (PPCPs) and artificial sweeteners (ASs) in surface and ground waters and their application as indication of wastewater contamination. *Sci. Total Environ.* **2017**, *616–617*, 816–823. [CrossRef]
2. Tran, N.H.; Reinhard, M.; Gin, K.Y.H. Occurrence and fate of emerging contaminants in municipal wastewater treatment plants from different geographical regions-a review. *Water Res.* **2018**, *133*, 182–207. [CrossRef] [PubMed]
3. D'Alessio, M.; Onanong, S.; Snow, D.D.; Ray, C. Occurrence and removal of pharmaceutical compounds and steroids at four wastewater treatment plants in Hawai'i and their environmental fate. *Sci. Total Environ.* **2018**, *631–632*, 1360–1370.
4. Tarpani, R.R.Z.; Azapagic, A. A methodology for estimating concentrations of pharmaceuticals and personal care products (PPCPs) in wastewater treatment plants and in freshwaters. *Sci. Total Environ.* **2018**, *622–623*, 1417–1430. [CrossRef]
5. Papageorgiou, M.; Kosma, C.; Lambropoulou, D. Seasonal occurrence, removal, mass loading and environmental risk assessment of 55 pharmaceuticals and personal care products in a municipal wastewater treatment plant in Central Greece. *Sci. Total Environ.* **2016**, *543*, 547–569. [CrossRef]
6. Fu, Q.; Han, Y.; Xie, Y.F.; Gong, N.B.; Guo, F. Carbamazepine cocrystals with several aromatic carboxylic acids in different stoichiometries: Structures and solid state characterization. *J. Mol. Struct.* **2018**, *1168*, 145–152. [CrossRef]
7. World Health Organization. *WHO Model List of Essential Medicines*, 20th ed.; WHO: Geneva, Switzerland, 2017.

8. Ekpeghere, K.I.; Sim, W.J.; Lee, H.J.; Oh, J.E. Occurrence and distribution of carbamazepine, nicotine, estrogenic compounds, and their transformation products in wastewater from various treatment plants and the aquatic environment. *Sci. Total Environ.* **2018**, *640–641*, 1015–1023. [CrossRef]
9. Wang, J.; Wang, S. Removal of pharmaceuticals and personal care products (PPCPs) from wastewater: A review. *J. Environ. Manag.* **2016**, *182*, 620–640. [CrossRef]
10. Björlenius, B.; Ripszám, M.; Haglund, P.; Lindberg, R.H.; Tysklind, M.; Fick, J. Pharmaceutical residues are widespread in Baltic Sea coastal and offshore waters—Screening for pharmaceuticals and modelling of environmental concentrations of carbamazepine. *Sci. Total Environ.* **2018**, *633*, 1496–1509. [CrossRef]
11. Fattore, E.; Zuccato, E.; Castiglioni, S.; Davoli, E.; Riva, F. Risk assessment of a mixture of emerging contaminants in surface water in a highly urbanized area in Italy. *J. Hazard. Mater.* **2018**, *361*, 103–110.
12. Radović, T.; Grujić, S.; Petković, A.; Dimkić, M.; Laušević, M. Determination of pharmaceuticals and pesticides in river sediments and corresponding surface and ground water in the Danube River and tributaries in Serbia. *Environ. Monit. Assess.* **2015**, *187*, 4092. [CrossRef] [PubMed]
13. Bahlmann, A.; Brack, W.; Schneider, R.J.; Krauss, M. Carbamazepine and its metabolites in wastewater: Analytical pitfalls and occurrence in Germany and Portugal. *Water Res.* **2014**, *57*, 104–114. [CrossRef] [PubMed]
14. Jurado, A.; López-Serna, R.; Vázquez-Suné, E.; Carrera, J.; Pujades, E.; Petrovic, M.; Barceló, D. Occurrence of carbamazepine and five metabolites in an urban aquifer. *Chemosphere* **2014**, *115*, 47–53. [CrossRef] [PubMed]
15. Brezina, E.; Prasse, C.; Meyer, J.; Mückter, H.; Ternes, T.A. Investigation and risk evaluation of the occurrence of carbamazepine, oxcarbazepine, their human metabolites and transformation products in the urban water cycle. *Environ. Pollut.* **2017**, *225*, 261–269. [CrossRef]
16. Wang, S.; Wang, J. Degradation of carbamazepine by radiation-induced activation of peroxymonosulfate. *Chem. Eng. J.* **2018**, *336*, 595–601. [CrossRef]
17. Almeida, Â.; Calisto, V.; Esteves, V.I.; Schneider, R.J.; Soares, A.M.V.M.; Figueira, E.; Freitas, R. Presence of the pharmaceutical drug carbamazepine in coastal systems: Effects on bivalves. *Aquat. Toxicol.* **2014**, *156*, 74–87. [CrossRef]
18. Tsiaka, P.; Tsarpali, V.; Ntaikou, I.; Kostopoulou, M.N.; Lyberatos, G.; Dailianis, S. Carbamazepine-mediated pro-oxidant effects on the unicellular marine algal species Dunaliella tertiolecta and the hemocytes of mussel Mytilus galloprovincialis. *Ecotoxicology* **2013**, *22*, 1208–1220. [CrossRef]
19. Rajendran, K.; Sen, S. Adsorptive removal of carbamazepine using biosynthesized hematite nanoparticles. *Environ. Nanotechnol. Monit. Manag.* **2018**, *9*, 122–127. [CrossRef]
20. Chtourou, M.; Mallek, M.; Dalmau, M.; Mamo, J.; Santos-Clotas, E.; Salah, A.B.; Walha, K.; Salvadó, V.; Monclús, H. Triclosan, carbamazepine and caffeine removal by activated sludge system focusing on membrane bioreactor. *Process Saf. Environ. Prot.* **2018**, *118*, 1–9. [CrossRef]
21. Wang, S.; Wang, J. Carbamazepine degradation by gamma irradiation coupled to biological treatment. *J. Hazard. Mater.* **2017**, *321*, 639–646. [CrossRef]
22. Tang, K.; Spiliotopoulou, A.; Chhetri, R.K.; Ooi, G.T.H.; Kaarsholm, K.M.S.; Sundmark, K.; Florian, B.; Kragelund, C.; Bester, K.; Andersen, H.R. Removal of pharmaceuticals, toxicity and natural fluorescence through the ozonation of biologically-treated hospital wastewater, with further polishing via a suspended biofilm. *Chem. Eng. J.* **2018**, *359*, 321–330. [CrossRef]
23. Hansen, K.M.S.; Spiliotopoulou, A.; Chhetri, R.K.; Escolà Casas, M.; Bester, K.; Andersen, H.R. Ozonation for source treatment of pharmaceuticals in hospital wastewater—Ozone lifetime and required ozone dose. *Chem. Eng. J.* **2016**, *290*, 507–514. [CrossRef]
24. Alharbi, S.K.; Price, W.E.; Kang, J.; Fujioka, T.; Long, D. Ozonation of carbamazepine, diclofenac, sulfamethoxazole and trimethoprim and formation of major oxidation products. *Desalin. Water Treat.* **2016**, *57*, 29340–29351. [CrossRef]
25. Dwivedi, K.; Rudrashetti, A.P.; Chakrabarti, T. Transformation Products of Carbamazepine (CBZ) After Ozonation and their Toxicity Evaluation Using *Pseudomonas* sp. Strain KSH-1 in Aqueous Matrices. *Indian J. Microbiol.* **2018**, *58*, 193–200. [CrossRef]
26. Hübner, U.; Seiwert, B.; Reemtsma, T.; Jekel, M. Ozonation products of carbamazepine and their removal from secondary effluents by soil aquifer treatment—Indications from column experiments. *Water Res.* **2014**, *49*, 34–43. [CrossRef]

27. Wang, B.; Zhang, H.; Wang, F.; Xiong, X.; Tian, K.; Sun, Y.; Yu, T. Application of heterogeneous catalytic ozonation for Refractory Organics in Wastewater. *Catalysts* **2019**, *9*, 241. [CrossRef]
28. Aghaeinejad-Meybodi, A.; Ebadi, A.; Shafiei, S.; Khataee, A.; Kiadehi, A.D. Degradation of Fluoxetine using catalytic ozonation in aqueous media in the presence of nano-γ-alumina catalyst: Experimental, modeling and optimization study. *Sep. Purif. Technol.* **2019**, *211*, 551–563. [CrossRef]
29. Chedeville, O.; Di Giusto, A.; Delpeux, S.; Cagnon, B. Oxidation of pharmaceutical compounds by ozonation and ozone/activated carbon coupling: A kinetic approach. *Desalin. Water Treat.* **2016**, *57*, 18956–18963. [CrossRef]
30. Ikhlaq, A.; Waheed, S.; Joya, K.S.; Kazmi, M. Catalytic ozonation of paracetamol on zeolite A: Non-radical mechanism. *Catal. Commun.* **2018**, *112*, 15–20. [CrossRef]
31. Saeid, S.; Tolvanen, P.; Kumar, N.; Eränen, K.; Peltonen, J.; Peurla, M.; Mikkola, J.P.; Franz, A.; Salmi, T. Advanced oxidation process for the removal of ibuprofen from aqueous solution: A non-catalytic and catalytic ozonation study in a semi-batch reactor. *Appl. Catal. B Environ.* **2018**, *230*, 77–90. [CrossRef]
32. Xu, Y.; Wang, Q.; Yoza, B.A.; Li, Q.X.; Kou, Y.; Tang, Y.; Ye, H.; Li, Y.; Chen, C. Catalytic ozonation of recalcitrant organic chemicals in water using vanadium oxides loaded ZSM-5 zeolites. *Front. Chem.* **2019**, *7*, 384. [CrossRef] [PubMed]
33. Aho, A.; Salmi, T.; Murzin, D.Y. Catalytic Pyrolysis of Lignocellulosic Biomass. *Role Catal. Sustain. Prod. Bio-Fuels Bio-Chem.* **2013**, 137–159. [CrossRef]
34. Somathilake, P.; Dominic, J.A.; Achari, G.; Cooper, H. Degradation of Carbamazepine by Photo-assisted Ozonation: Influence of Wavelength and Intensity of Radiation Degradation of Carbamazepine by Photo-assisted Ozonation: Influence of Wavelength and Intensity of Radiation. *Ozone Sci. Eng.* **2018**, *40*, 113–121. [CrossRef]
35. Cai, T.; Gao, Y.; Yan, J.; Wu, Y.; Di, J. Visual detection of glucose using triangular silver nanoplates and gold nanoparticles. *RSC Adv.* **2017**, *7*, 29122–29128. [CrossRef]
36. Han, Y.; Ma, M.; Li, N.; Hou, R.; Huang, C.; Oda, Y.; Wang, Z. Chlorination, chloramination and ozonation of carbamazepine enhance cytotoxicity and genotoxicity: Multi-endpoint evaluation and identification of its genotoxic transformation products. *J. Hazard. Mater.* **2018**, *342*, 679–688. [CrossRef] [PubMed]
37. Mcdowell, D.C.; Huber, M.M.; Wagner, M.; Von Gunten, U.; Ternes, T.A. Ozonation of carbamazepine in drinking water: Identification and kinetic study of major oxidation products. *Environ. Sci. Technol.* **2005**, *39*, 8014–8022. [CrossRef] [PubMed]
38. Gottschalk, C.; Libra, J.A.; Saupe, A. *Ozonation of Water and Waste Water*; Wiley-VCH: Weinheim, Germany, 2010; ISBN 9783527319626.
39. Einaga, H.; Maeda, N.; Nagai, Y. Comparison of catalytic properties of supported metal oxides for benzene oxidation using ozone. *Catal. Sci. Technol.* **2015**, *5*, 3147–3158. [CrossRef]
40. Rosal, R.; Rodríguez, A.; Gonzalo, M.S.; García-Calvo, E. Catalytic ozonation of naproxen and carbamazepine on titanium dioxide. *Appl. Catal. B Environ.* **2008**, *84*, 48–57. [CrossRef]
41. Kumar, N.; Mäki-Arvela, P.; Hajek, J.; Salmi, T.; Murzin, D.Y.; Heikkilä, T.; Laine, E.; Laukkanen, P.; Väyrynen, J. Physico-chemical and catalytic properties of Ru-MCM-41 mesoporous molecular sieve catalyst: Influence of Ru modification methods. *Microporous Mesoporous Mater.* **2004**, *69*, 173–179. [CrossRef]
42. Iodometric Method for the Determination of Ozone in a Process Gas. Available online: www.otsil.net/articles.html%0D (accessed on 2 January 2020).
43. Lin, W.C.; Chen, H.C.; Ding, W.H. Determination of pharmaceutical residues in waters by solid-phase extraction and large-volume on-line derivatization with gas chromatography-mass spectrometry. *J. Chromatogr. A* **2005**, *1065*, 279–285. [CrossRef]
44. Rossmann, J.; Schubert, S.; Gurke, R.; Oertel, R.; Kirch, W. Simultaneous determination of most prescribed antibiotics in multiple urban wastewater by SPE-LC-MS/MS. *J. Chromatogr. B Anal. Technol. Biomed. Life Sci.* **2014**, *969*, 162–170. [CrossRef] [PubMed]

catalysts

MDPI

Article

Chromium Oxide Supported on Silicalite-1 Zeolite as a Novel Efficient Catalyst for Dehydrogenation of Isobutane Assisted by CO_2

Yajun Luo [1], Changxi Miao [2,*], Yinghong Yue [1], Weimin Yang [2], Weiming Hua [1,*] and Zi Gao [1]

[1] Shanghai Key Laboratory of Molecular Catalysis and Innovative Materials, Department of Chemistry, Fudan University, Shanghai 200438, China; 15110220011@fudan.edu.cn (Y.L.); yhyue@fudan.edu.cn (Y.Y.); zigao@fuan.edu.cn (Z.G.)

[2] Shanghai Research Institute of Petrochemical Technology SINOPEC, Shanghai 201208, China; yangwm.sshy@sinopec.com

* Correspondence: miaocx.sshy@sinopec.com (C.M.); wmhua@fudan.edu.cn (W.H.); Tel.: +86-21-3124-9121 (W.H.)

Received: 3 November 2019; Accepted: 6 December 2019; Published: 7 December 2019

Abstract: The chromium oxide catalysts supported on silicalite-1 zeolite (Cr/S-1) with a Cr content between 0.5% and 7% were synthesized via an incipient wetness method. The catalysts were characterized by XRD, N_2 adsorption, TEM-EDX, UV-vis, DRIFTS, ^{29}Si MAS NMR, XPS, H_2-TPR, and NH_3-TPD. The optimum 3%Cr/S-1 catalyst with 3%Cr is more active and stable than SBA-15-supported one with the same Cr content, which is a consequence of a higher content of Cr^{6+} in the fresh 3%Cr/S-1 catalyst and a higher content of Cr^{6+} retained on the former catalyst during the reaction. The 3%Cr/S-1 catalyst affords an isobutane conversion of 36.5% with 71.2% isobutene selectivity. The catalytic activity is well correlated with the content of Cr^{6+} in the fresh catalysts. Carbon dioxide displays a promoting effect on the dehydrogenation reaction.

Keywords: CO_2 assisted dehydrogenation; isobutane; silicalite-1; SBA-15

1. Introduction

Isobutene is an important industrial chemical employed to produce butyl rubber, gasoline oxygenates (e.g., ethyl tert-butyl ether), and antioxidants (e.g., butylated hydroxyanisole) [1,2]. Its two main manufacture ways which rely on the source of petroleum, i.e., steam cracking of naphtha as well as fluidized catalytic cracking, cannot meet the increasing requirements. Due to the shortage of petroleum and environmental consideration, the dehydrogenation of small alkanes to alkenes assisted by CO_2 has attracted more attention recently [3–13]. Compared to the oxidative dehydrogenation of light alkanes with O_2, the beneficial employment of CO_2 as a soft oxidant comprises improving the product selectivity as well as decreasing CO_2 emissions [14,15]. Moreover, this route opens up a new way to utilize greenhouse CO_2.

The catalysts which were attempted for isobutane dehydrogenation assisted by CO_2 includes Cr_2O_3 [11,16], V_2O_5 [10,17,18], iron oxide [19], NiO [3], and V–Mg–O [20,21]. Ding et al. found that the isobutane conversion was enhanced from 29.8% to 50.3% for the dehydrogenation over active carbon-supported chromium oxide when replacing Ar with CO_2 [16]. Cr-based catalysts were found to exhibit higher activities for dehydrogenation of small alkanes and ethylbenzene with CO_2, and mesoporous silica molecular sieves (e.g., MCM-41 and SBA-15) were usually chosen as catalyst supports owing to their high mesopore volume and surface area [6,11,22–24]. Silicalite-1 is a siliceous zeolite with MFI structure. It is generally applied in the removal of volatile organic compounds [25], separation [26], acid catalyst [27,28], and catalyst support [29–31]. Silicalite-1 exhibits higher thermal and hydrothermal

stability than SBA-15. Thus, higher catalytic stability would be expected when employing silicalite-1 as catalyst support. Herein, a novel efficient catalyst system, i.e., silicalite-1 zeolite supported chromium oxide (Cr/S-1), for CO_2 assisted dehydrogenation of isobutane was developed, and compared with the chromia catalyst supported on SBA-15 (Cr/SBA). The catalytic result of Cr/S-1 was correlated with their physico-chemical properties, and the superior performance of Cr/S-1 to Cr/SBA was revealed.

2. Results and Discussion

2.1. Catalyst Characterization

The MFI structure of the Cr/S-1 catalysts is evidenced by their XRD patterns (Figure 1), i.e., diffraction peaks at 2θ = 8.0°, 8.9°, 23.1°, 23.3°, and 24.0° [12,32]. Crystalline Cr_2O_3 cannot be observed until the Cr content reaches 7%, indicating that chromium oxide is highly dispersed on silicate-1 zeolite at a Cr content ≤3%. The 3%Cr/SBA catalyst does not show Cr_2O_3 crystallites either (Figure 1a). The good preservation of the ordered hexagonal mesoporous structure of SBA-15 upon supporting chromia is demonstrated by the SAXS patterns (Figure S1). The more homogeneous distribution of chromium on 3%Cr/S-1 than 3%Cr/SBA is verified by the HAADF STEM mapping (Figure S2).

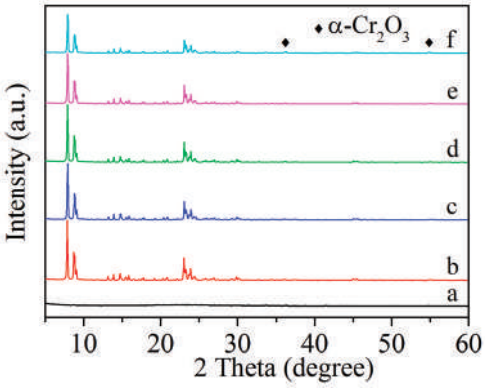

Figure 1. XRD patterns of the catalysts. (**a**) 3%Cr/SBA, (**b**) 0.5%Cr/S-1, (**c**) 1%Cr/S-1, (**d**) 2%Cr/S-1, (**e**) 3%Cr/S-1, (**f**) 7%Cr/S-1.

A surface area of 379 m^2/g observed for silicalite-1 zeolite (Table 1) is similar to the value reported in the literature [30]. As the Cr content increases from 0.5% to 3%, the surface area, microporosity and mesoporosity (contribution from silicalite-1 intercrystalline voids) of the Cr/S-1 catalysts slightly decrease (Table 1). At a high content of Cr (7%), the microporosity obviously decreases, which can be attributed to the blockage of some micropores by large chromium oxide particles (evidenced by XRD observation).

The band at 541 cm^{-1} on the Raman spectra of the Cr/S-1 and 3%Cr/SBA catalysts is characteristic of Cr_2O_3 crystallites (Figure 2) [33–35]. This band does not appear until the Cr content achieves 3% for the Cr/S-1 catalysts. The stronger intensity of this band found for the 3%Cr/SBA catalyst than 3%Cr/S-1 suggests that chromium oxide is worse dispersed on the former catalyst, which is consistent with the result of STEM mapping. The band at 983 cm^{-1} and the shoulder at 1006 cm^{-1} are related to the Cr-O stretching of monochromate and polychromate species, respectively [6,36]. The band at 603 cm^{-1} occurred in the 3%Cr/SBA catalyst is associated with a tri-siloxane ring in SBA-15 [37].

The bands at 275 and 359 nm on the diffuse reflectance UV-vis spectra of the Cr/S-1 and 3%Cr/SBA catalysts are attributed to tetrahedral Cr^{6+} species, while the ones at 458 and 599 nm are assigned to octahedral Cr^{3+} species existing in Cr_2O_3 or CrO_x clusters (Figure 3) [36,38]. The band at 599 nm cannot be found for the Cr/S-1 catalysts until the Cr content of 7%. 3%Cr/SBA shows the strongest

intensity of this band, suggesting the worse dispersion of chromium oxide on 3%Cr/SBA than 3%Cr/S-1. The above result is consistent with those of XRD and STEM mapping.

Table 1. Textural properties and H_2-TPR results of the samples.

Sample	S_{BET} (m^2/g)	V_{micro} [a] (cm^3/g)	V_{meso} (cm^3/g)	V_{total} [b] (cm^3/g)	T_M (°C)	H_2 Uptake (mmol/g)	Cr^{6+} (%) [c]
Silicalite-1	379	0.18	0.12	0.30	-	-	-
0.5%Cr/S-1	378	0.17	0.05	0.22	424	0.141	0.49
1%Cr/S-1	368	0.16	0.06	0.22	377	0.189	0.66
2%Cr/S-1	358	0.16	0.05	0.21	369	0.253	0.88
3%Cr/S-1	350	0.16	0.04	0.20	364	0.342	1.19
7%Cr/S-1	345	0.13	0.05	0.18	372 (213) [d]	0.330	1.14
SBA-15	655	0.06	1.02	1.08	-	-	-
3%Cr/SBA	469	0.02	0.69	0.71	373	0.304	1.05

[a] Calculated by the *t*-plot method; [b] Total pore volume adsorbed at $P/P_0 = 0.99$; [c] The weight percentage of Cr^{6+} in the sample calculated based on the H_2 consumption, assuming that Cr^{6+} was reduced to Cr^{3+} by H_2; [d] The high-temperature reduction peak and low-temperature one are 372 °C and 213 °C, respectively.

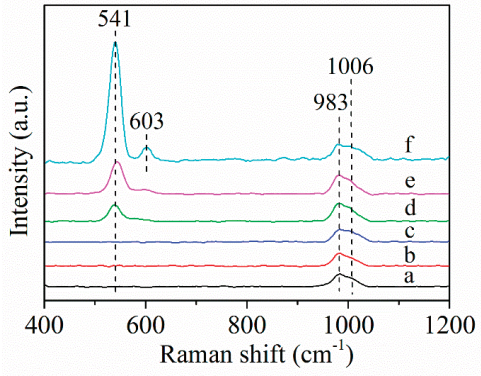

Figure 2. Raman spectra of the catalysts. (**a**) 0.5%Cr/S-1, (**b**) 1%Cr/S-1, (**c**) 2%Cr/S-1, (**d**) 3%Cr/S-1, (**e**) 7%Cr/S-1, (**f**) 3%Cr/SBA.

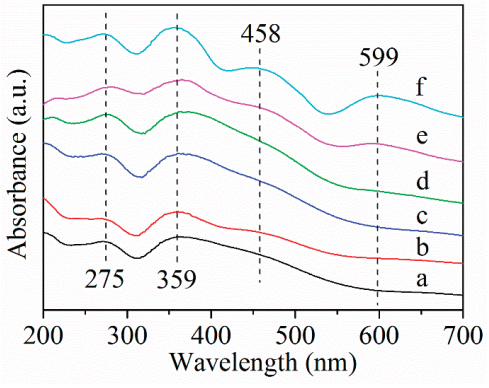

Figure 3. Diffuse reflectance UV-vis spectra of the catalysts. (**a**) 0.5%Cr/S-1, (**b**) 1%Cr/S-1, (**c**) 2%Cr/S-1, (**d**) 3%Cr/S-1, (**e**) 7%Cr/S-1, (**f**) 3%Cr/SBA.

The XPS spectra of the 3%Cr/S-1 and 3%Cr/SBA catalysts are depicted in Figure S3, and the XPS data are listed in Table 2. A remarkable decrease in the Cr^{6+} to Cr^{3+} ratio after isobutane

dehydrogenation is indicative of the reduction of most Cr^{6+} to Cr^{3+}. More Cr^{6+} was reduced to Cr^{3+} in the absence of CO_2 than in the presence of CO_2. The Cr^{6+} to Cr^{3+} ratio is greater for 3%Cr/S-1 than 3%Cr/SBA, both before and after the dehydrogenation reaction assisted by CO_2. After isobutane dehydrogenation over 3%Cr/S-1 in the absence of CO_2, followed by the treatment with CO_2 at the same temperature, the Cr^{6+} to Cr^{3+} ratio increases from 0.91 to 1.97, but it is still lower than the value of the fresh catalyst (2.82). This finding implies that CO_2 assisted isobutane dehydrogenation proceeds via a redox mechanism (Scheme 1).

Table 2. Summary of XPS data.

Sample	Sample Description	E_b (eV) [a]		Cr^{6+}/Cr^{3+} [b]
		Cr^{3+}	Cr^{6+}	
A	Fresh 3%Cr/S-1	576.9	579.2	2.82
B	Sample A reacted for 6 h in the presence of CO_2	577.1	579.5	1.19
C	Sample A reacted for 6 h in the absence of CO_2	576.7	579.6	0.91
D	Sample C subsequently treated with CO_2 at 570 °C for 0.5 h	577.0	579.4	1.97
E	Fresh 3%Cr/SBA	576.7	579.2	2.42
F	Sample E reacted for 6 h in the presence of CO_2	576.8	579.3	0.72

[a] Binding energy of Cr $2p_{3/2}$; [b] Atomic ratio of Cr^{6+} to Cr^{3+}. Reaction conditions: 570 °C, 0.1 g catalyst, CO_2 (N_2)/*i*-C_4H_{10} = 1 (mol/mol), WHSV = 4.1 h^{-1}.

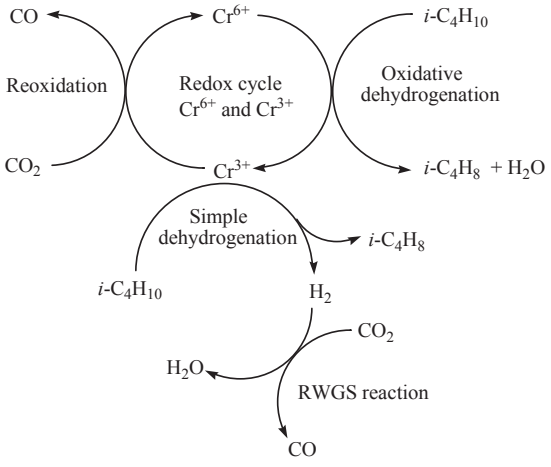

Scheme 1. Proposed reaction mechanism of isobutane dehydrogenation assisted by CO_2 over silicalite-1-supported chromium oxide catalysts.

The peak on the H_2-TPR profiles of the Cr/S-1 and 3%Cr/SBA catalysts with peak temperatures between 364 and 424 °C is assigned to the reduction of Cr^{6+} to Cr^{3+} (Figure 4) [39–41]. An additional small peak at 213 °C is observed for the 7%Cr/S-1 catalyst, indicating that large chromia crystals exist on this catalyst in addition to the dispersed chromium oxide [42]. The H_2-TPR data are presented in Table 1. The 3%Cr/S-1 catalyst exhibits a lower reduction in temperature than 3%Cr/SBA (364 °C vs. 373 °C), showing that the former catalyst displays higher reducibility than the latter one. The higher content of Cr^{6+} observed in 3%Cr/S-1 than 3%Cr/SBA (1.19% vs. 1.05%) could be related to the better dispersion of chromium species on silicalite-1 [11], as demonstrated by the STEM mapping result.

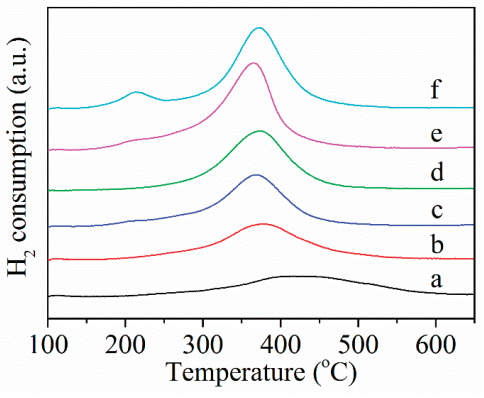

Figure 4. H_2-TPR profiles of the catalysts. (**a**) 0.5%Cr/S-1; (**b**) 1%Cr/S-1; (**c**) 2%Cr/S-1; (**d**) 3%Cr/SBA; (**e**) 3%Cr/S-1; (**f**) 7%Cr/S-1.

As revealed in Figure 5, silicalite-1 zeolite has three kinds of hydroxyl groups: Isolated silanol groups (3739 cm^{-1}), vicinal silanol groups (3686 cm^{-1}), and nest silanol groups (3493 cm^{-1}) [27,43,44]. After supporting chromium oxide, the intensities of these -OH groups, particularly the nest silanol groups, diminish. The peak area ratio of nest silanol groups to isolated silanol ones declines from 16 to 5.0 after supporting chromia (3%Cr). This observation suggests that the number of silanol groups decreases via the interaction of Cr species with the -OH groups [29,44,45]. SBA-15 has only isolated silanol groups. Supporting chromium oxide on SBA-15 also leads to a decrease in the number of hydroxyl groups. The nest silanols have a higher local density of hydroxyls than isolated silanols [46], thus resulting in a stronger interaction between chromium species and nest silanols. Therefore, the better dispersion of chromium species on silicalite-1 than SBA-15 can be attributed to the abundant nest silanol groups present on the former support.

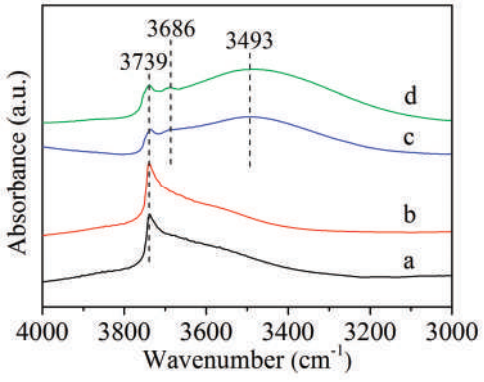

Figure 5. DRIFT spectra of some selected samples. (**a**) 3%Cr/SBA, (**b**) SBA-15, (**c**) 3%Cr/S-1, (**d**) silicalite-1.

Figure S4 presents the ^{29}Si MAS NMR spectra of some selected samples. For silicalite-1 and 3%Cr/S-1 samples, two resonances at −113 and −102 ppm correspond to Q^4 and Q^3 species representing (Si-[$(OSi)_4$]) and (HO-Si-[$(OSi)_3$]), respectively [28]. The ratio of Q^3 to Q^4 decreases from 0.108 for silicalite-1 to 0.096 for 3%Cr/S-1, indicating a loss of silanol groups. In the case of SBA-15 and 3%Cr/SBA, the broad signal can be deconvoluted into a few peaks. The peaks at ca. −90 and −100 ppm are attributed to Q^2 ([$HO]_2$-Si-[$(OSi)_2$]) and Q^3 species, respectively, while the ones below −102 ppm are

assigned to Q^4 species [23,47]. The lower (Q^2 + Q^3) to Q^4 ratio observed for 3%Cr/SBA than SBA-15 (0.272 vs. 0.341) implies a decrease in the number of hydroxyl groups.

2.2. Catalytic Performance

The catalytic results of CO_2 assisted isobutane dehydrogenation over the Cr/S-1 catalysts are shown in Figure 6 and Table 3. The effect of content of Cr in the Cr/S-1 catalysts on the initial conversion of isobutane and initial product selectivity is depicted in Figure S5. The initial isobutene selectivity declines from 79.7% to 71.2%, with increasing the Cr content from 0.5% to 3%, followed by a slight diminishment with further increasing the Cr content to 7%. The initial selectivities to C1-C3 (alkanes and alkenes) and butenes (except isobutene) follow the opposite variation trend. The activity is strongly dependent on the Cr content. The initial isobutane conversion improves markedly from 20.8% to 36.5% with increasing the Cr content from 0.5% to 3%, followed by a very slight decline in the conversion with further increasing the Cr content to 7%. The 3%Cr/S-1 catalyst displays the optimum activity, giving 36.5% isobutane conversion and 71.2% selectivity toward isobutene. As shown in Table 3, the catalyst which is more active for CO_2 assisted dehydrogenation of isobutane displays higher activity for the conversion of CO_2 to CO. The very small conversion of isobutane (ca. 3%) observed on silicalite-1 zeolite suggests that the dispersed chromium oxide on silicalite-1 is primarily responsible for the catalytic activity.

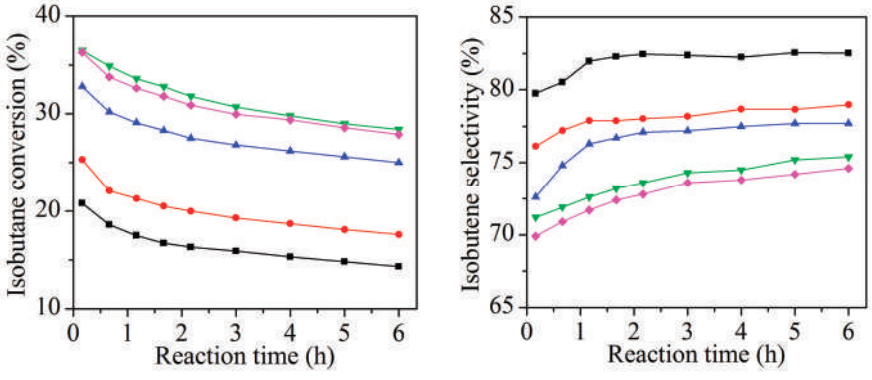

Figure 6. Catalytic performance of the Cr/S-1 catalysts for isobutane dehydrogenation assisted by CO_2 at 570 °C, (■) 0.5%Cr/S-1, (●) 1%Cr/S-1, (▲) 2%Cr/S-1, (▼) 3%Cr/S-1, (♦) 7%Cr/S-1. Reaction conditions: 570 °C, 0.1 g catalyst, CO_2/*i*-C_4H_{10} = 1 (mol/mol), WHSV = 4.1 h^{-1}.

Table 3. Reaction data of silicalite-1-supported chromium oxide catalysts [a].

Catalyst	Conversion (%)		Selectivity (%)							H_2/CO [c]
	i-C_4H_{10}	CO_2	*i*-C_4H_8	CH_4	C_2H_4	C_2H_6	C_3H_6	C_3H_8	C_4H_8 [b]	
0.5%Cr/S-1	20.8 (14.3)	3.5 (1.7)	79.7 (82.5)	3.9 (3.2)	0 (0)	0 (0)	10.7 (9.4)	0.9 (0.7)	4.8 (4.2)	4.2 (5.6)
1%Cr/S-1	25.3 (17.6)	4.8 (4.4)	76.1 (79.0)	4.8 (4.4)	0.6 (0.3)	0.4 (0.1)	10.9 (11.4)	1.3 (0.7)	5.9 (4.1)	2.6 (3.1)
2%Cr/S-1	32.8 (25.0)	10.6 (5.6)	72.6 (77.7)	5.3 (4.4)	0.7 (0.3)	0.6 (0.3)	11.0 (10.1)	1.8 (1.2)	8.0 (6.0)	1.9 (2.1)
3%Cr/S-1	36.5 (28.4)	13.3 (6.9)	71.2 (75.4)	5.6 (4.9)	0.8 (0.5)	0.9 (0.6)	11.4 (10.6)	2.0 (1.5)	8.1 (6.5)	1.8 (2.0)
7%Cr/S-1	36.3 (27.9)	11.7 (6.2)	69.9 (74.6)	5.8 (5.2)	1.0 (0.7)	1.0 (0.7)	11.6 (10.5)	2.2 (1.7)	8.5 (6.6)	2.0 (2.4)

[a] The values outside and inside the bracket are the data obtained at 10 min and 6 h, respectively; [b] Butenes excluding isobutene; [c] Molar ratio of H_2 to CO. Reaction conditions are the same as given in caption to Figure 6.

It is well accepted that CO_2 assisted dehydrogenation of small alkanes over metal oxides with redox property (e.g., chromia and vanadia) proceeds through a redox mechanism [18,22,48,49]:

$$C_nH_{2n+2} + MO_x = C_nH_{2n} + MO_{x-1} + H_2O \quad (1)$$

$$CO_2 + MO_{x-1} = CO + MO_x \quad (2)$$

The XPS results (Table 2) confirm that CO_2 assisted isobutane dehydrogenation follows the redox mechanism (Scheme 1). According to this redox mechanism, one might envisage that the Cr/S-1 catalyst having a higher amount of Cr^{6+} species would favor the dehydrogenation reaction. This hypothesis is further demonstrated by a good correlation between the initial activity and the content of Cr^{6+} in the fresh Cr/S-1 catalysts as measured by H_2-TPR (Figure 7). On the other hand, H_2 was detectable in the products. The H_2 to CO molar ratio for the Cr/S-1 catalysts is presented in Table 3. This finding suggests that besides the redox mechanism (i.e., a one-step pathway, *i*-C_4H_{10} + CO_2 = *i*-C_4H_8 + CO + H_2O), a two-step pathway also occurs during the reaction, i.e., a simple dehydrogenation of isobutane coupled with the reverse water-gas shift (RWGS) reaction (Scheme 1). The results of a separate RWGS reaction carried out at 570 °C verify that the Cr/S-1 catalysts are indeed active for this reaction (Figure S6).

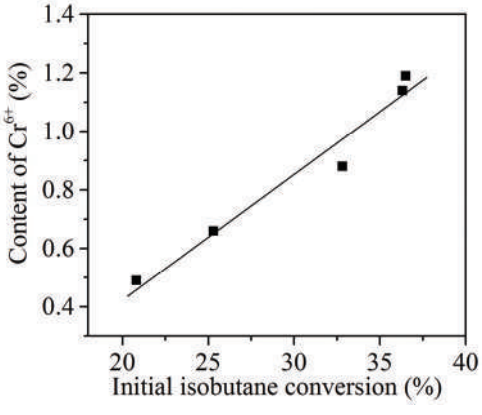

Figure 7. Correlation between the initial conversion of isobutane in the presence of CO_2 and the content of Cr^{6+} in the fresh Cr/S-1 catalysts. Reaction conditions are the same as given in caption to Figure 6.

We chose the best 3%Cr/S-1 to investigate its catalytic performance under a CO_2 or N_2 atmosphere (Figure 8). In the case of CO_2 atmosphere, this catalyst gives a 36.5% isobutane conversion with 71.2% isobutene selectivity after 10 min of reaction. In the case of N_2 atmosphere, the initial isobutane conversion and isobutene selectivity are 30.8% and 67.5%, respectively. This finding suggests that CO_2 displays a promoting effect on isobutane dehydrogenation. CO_2 enhances the dehydrogenation reaction via a redox mechanism in which the catalyst undergoes reduction (by isobutane) and reoxidation (by carbon dioxide) cycles as well as the reaction coupling between a simple dehydrogenation of isobutane and the RWGS reaction, as illustrated in Scheme 1.

A comparison of 3%Cr/S-1 and 3%Cr/SBA catalysts indicates that the initial isobutane conversion is higher on 3%Cr/S-1 than 3%Cr/SBA (Figure 9, 36.5% vs. 33.5%), which is caused by the fact that the former catalyst possesses a higher content of Cr^{6+} than the latter one (1.19% vs. 1.05%). The higher isobutene selectivity observed for 3%Cr/SBA than 3%Cr/S-1 is due to the fact that the former catalyst has lower acidity and weaker acid sites. Two desorption peaks on the NH_3-TPD profiles of both 3%Cr/S-1 and 3%Cr/SBA catalysts correspond to the weak and strong acid sites of the catalysts (Figure S7). The higher peak temperature observed for 3%Cr/S-1 than 3%Cr/SBA (393 °C vs. 320 °C) suggests that the former catalyst has stronger acid sites than the latter one. Moreover, the 3%Cr/S-1 catalyst has more acid sites than 3%Cr/SBA (0.445 vs. 0.266 mmol/g). Moreover, the 3%Cr/S-1 catalyst exhibits higher stability than 3%Cr/SBA. After 6 h of the reaction, the isobutane conversion for 3%Cr/S-1 and 3%Cr/SBA is 28.4% and 20.2%, respectively. Coking and the reduction of Cr^{6+} to Cr^{3+} are two causes responsible for the catalyst deactivation [11,50]. An in situ pretreatment of the 3%Cr/S-1 catalyst

with 10% H_2/Ar (30 mL/min) at 450 °C for 1 h leads to a decline in the initial activity from 36.5% to 32.3% (Figure 10), further confirming that the reduction of Cr^{6+} to Cr^{3+} is one of the causes for the deactivation of catalyst. The amount of coke on 3%Cr/S-1 and 3%Cr/SBA catalysts after 6 h of the reaction is 3.2% and 1.5%, respectively. The TPO profiles of both spent 3%Cr/S-1 and 3%Cr/SBA catalysts are shown in Figure S8. The peak temperature is lower for the former catalyst than the latter one (359 °C vs. 375 °C), suggesting that coke deposited on 3%Cr/S-1 is more easily burnt off. The NH_3-TPD result accounts for the higher amount of coke on 3%Cr/S-1 than 3%Cr/SBA. The XPS result shows that after the reaction, the Cr^{6+} to Cr^{3+} ratio is higher for 3%Cr/S-1 than 3%Cr/SBA (Table 2, 1.19 vs. 0.72). This result implies that the reduced chromium species which interact with the nest silanols could be more easily reoxidized to Cr^{6+} species by CO_2 during the dehydrogenation reaction. Hence, the higher catalytic stability of 3%Cr/S-1 than 3%Cr/SBA is ascribed to a higher amount of Cr^{6+} species retained during the reaction, which could be related to the abundant nest silanol groups present on the silicalite-1 support. There are no differences in the XRD patterns for the spent and fresh 3%Cr/S-1 catalysts (Figure S9), indicating the good maintenance of the catalyst structure. However, an evident diminishment in the intensity of XRD patterns for the spent 3%Cr/SBA catalyst in comparison with the fresh one was observed, suggesting a degradation of the ordered hexagonal arrangement of the SBA-15 mesopores. This is another cause for the lower catalytic stability of the 3%Cr/SBA catalyst.

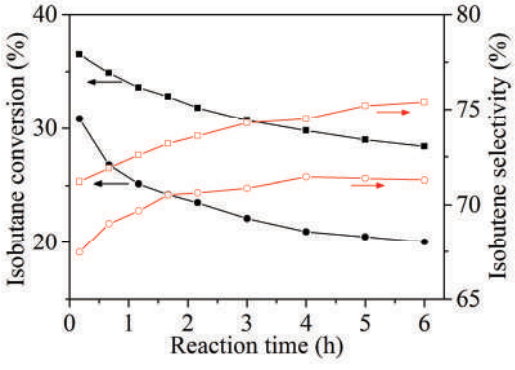

Figure 8. Conversion of isobutane and selectivity to isobutene as a function of reaction time for the 3%Cr/S-1 catalyst at 570 °C in the presence (■, □) and absence (●, ○) of CO_2. Reaction conditions: 0.1 g catalyst, CO_2 (N_2)/*i*-C_4H_{10} = 1 (mol/mol), WHSV = 4.1 h^{-1}.

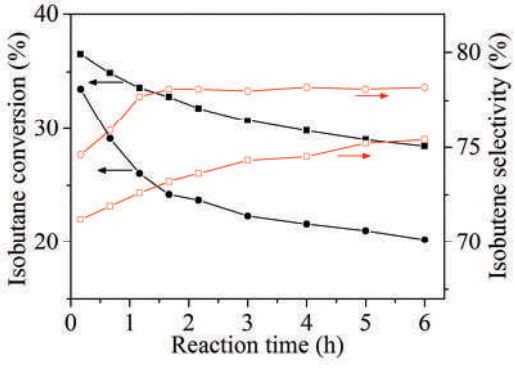

Figure 9. Conversion of isobutane and selectivity to isobutene as a function of reaction time at 570 °C in the presence of CO_2. (■, □) 3%Cr/S-1, (●, ○) 3%Cr/SBA. Reaction conditions are the same as given in caption to Figure 6.

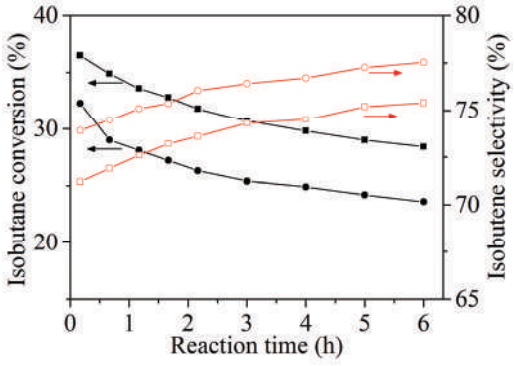

Figure 10. Conversion of isobutane and selectivity to isobutene as a function of reaction time for the 3%Cr/S-1 catalyst. (■, □) fresh catalyst, (●, ○) catalyst that was in situ pretreated by 10 vol.% H_2/Ar at 450 °C for 1 h. Reaction conditions are the same as given in caption to Figure 6.

3. Materials and Methods

3.1. Catalyst Preparation

Silicalite-1 zeolite was synthesized as follows [51]. Tetrapropylammonium hydroxide (TPAOH, 25% aqueous solution), tetraethyl orthosilicate (TEOS), and distilled water were mixed to obtain a clear suspension (9TPAOH:25SiO_2:480H_2O, molar composition). The above mixture was stirred at room temperature to hydrolyze TEOS for 4 h, followed by being transferred into an autoclave and crystallized at 170 °C for 72 h. The obtained product was filtered, washed, and dried at 100 °C overnight, followed by calcination at 550 °C for 4 h in air.

The silicalite-1-supported chromium oxide catalysts were prepared through an incipient wetness method employing $Cr(NO_3)_3{\cdot}9H_2O$ as the precursor. The impregnated samples were dried at 100 °C overnight, followed by calcination in air at 600 °C for 6 h. The obtained catalysts were designated as *x*%Cr/S-1, where *x*% represents the weight percentage of Cr in the catalysts. For the purpose of comparison, the 3%Cr/SBA catalyst (3%Cr) was prepared in the same way using SBA-15 as the support. SBA-15 was prepared according to the literature [52].

3.2. Catalyst Characterization

X-ray diffraction (XRD) measurements were performed with a D2 PHASER X-ray diffractometer (Brucker, Madison, WI, USA) at 40 mA and 40 kV. Small-angle *X*-ray scattering (SAXS) measurements were performed with a Nanostar U SAXS system (Brucker, Madison, WI, USA) using Cu Kα radiation at 35 mA and 40 kV. The surface areas and pore volumes of the catalysts were measured by N_2 adsorption on a Tristar 3000 instrument (Micromeritics, Atlanta, GA, USA). The HAADF-STEM images and elemental mapping were acquired with a Tecnai G^2 F20 S-TWIN instrument (FEI, Hillsboro, TX, USA). Diffuse reflectance ultraviolet-visible (UV-vis) spectra were collected with a Lambda 650S spectrometer (Perkin-Elmer, Waltham, MA, USA). Raman spectra were collected with an XploRA spectrometer (HORIBA Jobin Yvon, Paris, France). The exciting light wavelength was 532 nm. *X*-ray photoelectron spectroscopy (XPS) measurements were performed on a PHI 5000C spectrometer with Mg Kα radiation (Perkin-Elmer, Waltham, MA, USA). ^{29}Si MAS NMR characterization was carried out with an AVANCE III 400WB instrument (Brucker, Rheinstetten, Germany). To analyze the amount of deposited coke on the catalyst after reaction, thermogravimetric (TG) analysis was carried out in flowing air with a TGA8000 apparatus (Perkin-Elmer, Waltham, MA, USA).

Temperature-programmed desorption of NH_3 (NH_3-TPD), temperature-programmed reduction of H_2 (H_2-TPR), and temperature-programmed oxidation (TPO) characterizations were performed on an AutoChem II instrument (Micromeritics, Atlanta, GA, USA). We pretreated 0.1 g of sample (40–60 mesh)

in situ at 550 °C in N_2 flow for 1 h before the measurement. In the case of NH_3-TPD experiment, the temperature was cooled to 80 °C, and the flow was changed to 10 vol.% NH_3/He (30 mL/min) and maintained at 80 °C for 2 h, followed by being swept with He (30 mL/min) for 2 h. Then, the sample was heated in He (30 mL/min) to 600 °C at a ramp rate of 10 °C/min. In the case of H_2-TPR experiment, the temperature was cooled to 100 °C, and the flow was switched to 10% H_2/Ar (30 mL/min), followed by heating to 650 °C at a ramp rate of 10 °C/min. In the case of TPO experiment, the temperature was cooled to 150 °C, and the flow was changed to 3% O_2/He (30 mL/min), followed by heating to 650 °C at a ramp rate of 10 °C/min. Diffuse reflectance infrared Fourier transform spectroscopy (DRIFTS) spectra were recorded at 300 °C on a Nicolet 6700 spectrometer (ThermoFisher, Waltham, MA, USA) equipped with an MCT detector and a heating accessory. The sample was pretreated in situ in flowing He (30 mL/min) at 450 °C for 1 h before the measurement.

3.3. Catalytic Evaluation

Catalytic performance in CO_2 assisted dehydrogenation of isobutane was carried at 570 °C in a fixed-bed quartz tube reactor (6 mm internal diameter) under ambient pressure. The catalyst loading was 0.1 g. The catalyst (40–60 mesh) was activated in situ in N_2 flow at 570 °C for 1 h before the reaction. The feed gas contained 50 vol.% CO_2 and 50 vol.% isobutane (2.9 mL/min of isobutane), i.e., the weight hourly space velocity of 4.1 h^{-1} for isobutane. In the case of isobutane dehydrogenation in the absence of CO_2, CO_2 was replaced by N_2, while keeping the other reaction conditions the same. In the case of reverse water–gas shift reaction, the feed gas contained 50 vol.% H_2 and 50 vol.% CO_2 (2.9 mL/min of CO_2), while keeping the other reaction conditions the same. The hydrocarbon products were in-situ analyzed with a GC (FID and HP-AL/S capillary column). The column temperature was 100 °C. CO and CO_2 were in-situ analyzed with another GC (TCD and carbon molecular sieve 601 packed column). The column temperature was 70 °C. The conversion and selectivity were calculated using the standard normalization method.

4. Conclusions

In this work, we have explored the silicalite-1-supported chromium oxide catalysts for isobutane dehydrogenation assisted by CO_2. This family of catalysts is shown to be effective for the reaction. A good correlation between the initial activity of the Cr/S-1 catalysts and content of Cr^{6+} in the fresh catalysts is established. CO_2 promotes the isobutane dehydrogenation via a redox mechanism and two-step pathway. The best 3%Cr/silicalite-1 catalyst gives an isobutane conversion of 36.5% with 71.2% isobutene selectivity. The greater initial activity observed for 3%Cr/S-1 than 3%Cr/SBA is attributed to a higher content of Cr^{6+} in the fresh 3%Cr/S-1 catalyst, and the better catalytic stability for the former catalyst than the latter one is associated with a higher content of Cr^{6+} retained on the former catalyst during the reaction. This finding could be related to the abundant nest silanol groups present on the silicalite-1 support.

Supplementary Materials: The following are available online at http://www.mdpi.com/2073-4344/9/12/1040/s1, Figure S1: SAXS patterns of SBA-15 and 3%Cr/SBA, Figure S2: HAADF STEM images (left) and corresponding EDX elemental mapping of Cr (right). (a) 3%Cr/S-1; (b) 3%Cr/SBA, Figure S3: XPS spectra of Cr 2p on the fresh and spent 3%Cr/S-1 and 3%Cr/SBA catalysts. (a) fresh 3%Cr/S-1; (b) 3%Cr/S-1 after isobutane dehydrogenation in the presence of CO_2 at 570 °C for 6 h; (c) 3%Cr/S-1 after isobutane dehydrogenation in the absence of CO_2 (i.e., using N_2 instead of CO_2) at 570 °C for 6 h; (d) 3%Cr/S-1 after isobutane dehydrogenation in the absence of CO_2 at 570 °C for 6 h, followed by treatment with CO_2 at 570 °C for 0.5 h; (e) fresh 3%Cr/SBA; (f) 3%Cr/SBA after isobutane dehydrogenation in the presence of CO_2 at 570 °C for 6 h, Reaction conditions: 570 °C, 0.1 g catalyst, CO_2 (N_2)/*i*-C_4H_{10} = 1 (mol/mol), WHSV = 4.1 h^{-1}, Figure S4: ^{29}Si MAS NMR spectra of (a) Silicalite-1, (b) 3%Cr/S-1, (c) SBA-15 and (d) 3%Cr/SBA, Figure S5: The effect of content of Cr in the Cr/S-1 catalysts on the initial conversion of isobutane and initial product selectivity. Reaction conditions: 570 °C, 0.1 g catalyst, CO_2/*i*-C_4H_{10} = 1 (mol/mol), WHSV = 4.1 h^{-1}. Figure S6: The results of the reverse water gas shift reaction over the Cr/S-1 catalysts at 570 °C. (■) 0.5%Cr/S-1; (●) 1%Cr/S-1; (▲) 2%Cr/S-1; (▼) 3%Cr/S-1; (♦) 7%Cr/S-1. Reaction conditions: 0.1 g catalyst, CO_2/H_2 = 1 (mol/mol), 2.9 mL/min of CO_2. Figure S7: NH_3-TPD profiles of (a) 3%Cr/SBA and (b) 3%Cr/S-1, Figure S8: TPO profiles of both spent 3%Cr/S-1 and 3%Cr/SBA catalysts. Reaction conditions are the same as given in caption to

Figure S5. Figure S9: (a) SAXS patterns of 3%Cr/SBA and (b) XRD patterns of 3%Cr/S-1 before and after isobutane dehydrogenation assisted by CO_2. Reaction conditions are the same as given in caption to Figure S5.

Author Contributions: C.M., W.H. conceived and designed the experiments; Y.L. performed the experiments; Y.Y., W.H. and Z.G. analyzed the data; Y.L. wrote the paper; C.M., W.Y. and W.H. revised the paper.

Acknowledgments: This work was financially supported by the National Key R&D Program of China (2017YFB0602200), the National Natural Science Foundation of China (91645201), the Science and Technology Commission of Shanghai Municipality (13DZ2275200) and the Shanghai Research Institute of Petrochemical Technology SINOPEC (17ZC06070001).

Conflicts of Interest: The authors declare no conflict of interest.

References

1. Sun, J.; Zhu, K.; Gao, F.; Wang, C.; Liu, J.; Peden, C.H.F.; Wang, Y. Direct conversion of bio-ethanol to isobutene on nanosized $Zn_xZr_yO_z$ mixed oxides with balanced acid–base sites. *J. Am. Chem. Soc.* **2011**, *133*, 11096–11099. [CrossRef] [PubMed]
2. Luttrell, W.E. Isobutylene. *J. Chem. Health Saf.* **2013**, *20*, 35–37. [CrossRef]
3. Ding, J.F.; Qin, Z.F.; Li, X.K.; Wang, G.F.; Wang, J.G. Catalytic dehydrogenation of isobutane in the presence of carbon dioxide over nickel supported on active carbon. *J. Mol. Catal. A* **2010**, *315*, 221–225. [CrossRef]
4. Chen, M.; Wu, J.L.; Liu, Y.M.; Cao, Y.; Guo, L.; He, H.Y.; Fan, K.N. Study in support effect of In_2O_3/MO_x (M = Al, Si, Zr) catalysts for dehydrogenation of propane in the presence of CO_2. *Appl. Catal. A* **2011**, *407*, 20–28. [CrossRef]
5. Michorczyk, P.; Ogonowski, J.; Zenczak, K. Activity of chromium oxide deposited on different silica supports in the dehydrogenation of propane with CO_2—A comparative study. *J. Mol. Catal. A* **2011**, *349*, 1–12. [CrossRef]
6. Baek, J.; Yun, H.J.; Yun, D.; Choi, Y.; Yi, J. Preparation of highly dispersed chromium oxide catalysts supported on mesoporous silica for the oxidative dehydrogenation of propane using CO_2: Insight into the nature of catalytically active chromium sites. *ACS Catal.* **2012**, *2*, 1893–1903. [CrossRef]
7. Wu, J.L.; Chen, M.; Liu, Y.M.; Cao, Y.; He, H.Y.; Fan, K.N. Sucrose-templated mesoporous β-Ga_2O_3 as a novel efficient catalyst for dehydrogenation of propane in the presence of CO_2. *Catal. Commun.* **2013**, *30*, 61–65. [CrossRef]
8. Koirala, R.; Buechel, R.; Krumeich, F.; Pratsinis, S.E. Oxidative dehydrogenation of ethane with CO_2 over flame-made Ga-loaded TiO_2. *ACS Catal.* **2015**, *5*, 690–702. [CrossRef]
9. Rahmani, F.; Haghighi, M.; Amini, M. The beneficial utilization of natural zeolite in preparation of Cr/clinoptilolite nanocatalyst used in CO_2-oxidative dehydrogenation of ethane to ethylene. *J. Ind. Eng. Chem.* **2015**, *31*, 142–155. [CrossRef]
10. Wei, C.L.; Xue, F.Q.; Miao, C.X.; Yue, Y.H.; Yang, W.M.; Hua, W.M.; Gao, Z. Dehydrogenation of isobutane with carbon dioxide over SBA-15-supported vanadium oxide catalysts. *Catalysts* **2016**, *6*, 171. [CrossRef]
11. Wei, C.L.; Xue, F.Q.; Miao, C.X.; Yue, Y.H.; Yang, W.M.; Hua, W.M.; Gao, Z. Dehydrogenation of isobutane to isobutene with carbon dioxide over SBA-15-supported chromia-ceria catalysts. *Chin. J. Chem.* **2017**, *35*, 1619–1626. [CrossRef]
12. Cheng, Y.H.; Lei, T.Q.; Miao, C.X.; Hua, W.M.; Yue, Y.H.; Gao, Z. Ga_2O_3/NaZSM-5 for C_2H_6 dehydrogenation in the presence of CO_2: Conjugated effect of silanol. *Micropor. Mesopor. Mater.* **2018**, *268*, 235–242. [CrossRef]
13. Lei, T.Q.; Guo, H.Y.; Miao, C.X.; Hua, W.M.; Yue, Y.H.; Gao, Z. Mn-doped CeO_2 nanorod supported Au catalysts for dehydrogenation of ethane with CO_2. *Catalysts* **2019**, *9*, 119. [CrossRef]
14. Wang, S.B.; Zhu, Z.H. Catalytic conversion of alkanes to olefins by carbon dioxide oxidative dehydrogenations—A review. *Energy Fuels* **2004**, *18*, 1126–1139. [CrossRef]
15. Mukherjee, D.; Parkb, S.E.; Reddy, B.M. CO_2 as a soft oxidant for oxidative dehydrogenation reaction: An ecobenign process for industry. *J. CO2 Util.* **2016**, *16*, 301–312. [CrossRef]
16. Ding, J.F.; Qin, Z.F.; Li, X.K.; Wang, G.F.; Wang, J.G. Coupling dehydrogenation of isobutane in the presence of carbon dioxide over chromium oxide supported on active carbon. *Chin. Chem. Lett.* **2008**, *19*, 1059–1062. [CrossRef]
17. Ogonowski, J.; Skrzyńska, E. Dehydrogenation of isobutane in the presence of carbon dioxide over supported vanadium oxide catalysts. *React. Kinet. Catal. Lett.* **2006**, *88*, 293–300. [CrossRef]

18. Yuan, R.X.; Li, Y.; Yan, H.B.; Wang, H.; Song, J.; Zhang, Z.S.; Fan, W.B.; Chen, J.G.; Liu, Z.W.; Liu, Z.T.; et al. Insights into the vanadia catalyzed oxidative dehydrogenation of isobutane with CO_2. *Chin. J. Catal.* **2014**, *35*, 1329–1336. [CrossRef]
19. Shimada, H.; Akazawa, T.; Ikenaga, N.; Suzuki, T. Dehydrogenation of isobutane to isobutene with iron-loaded activated carbon catalyst. *Appl. Catal. A* **1998**, *168*, 243–250. [CrossRef]
20. Ogonowski, J.; Skrzyńska, E. Catalytic dehydrogenation of isobutane in the presence of carbon dioxide. *React. Kinet. Catal. Lett.* **2005**, *86*, 195–201. [CrossRef]
21. Ogonowski, J.; Skrzyńska, E. Activity of vanadium magnesium oxide supported catalysts in the dehydrogenation of isobutane. *Catal. Lett.* **2006**, *111*, 79–85. [CrossRef]
22. Shi, X.J.; Ji, S.F.; Wang, K. Oxidative Dehydrogenation of ethane to ethylene with carbon dioxide over Cr–Ce/SBA-15 catalysts. *Catal. Lett.* **2008**, *125*, 331–339. [CrossRef]
23. Cheng, Y.H.; Zhou, L.B.; Xu, J.X.; Miao, C.X.; Hua, W.M.; Yue, Y.H.; Gao, Z. Chromium-based catalysts for ethane dehydrogenation: Effect of SBA-15 support. *Micropor. Mesopor. Mater.* **2016**, *234*, 370–376. [CrossRef]
24. Ohishi, Y.; Kawabata, T.; Shishido, T.; Takaki, K.; Zhang, Q.H.; Wang, Y.; Takehira, K. Dehydrogenation of ethylbenzene with CO_2 over Cr-MCM-41 catalyst. *J. Mol. Catal. A* **2005**, *230*, 49–58. [CrossRef]
25. Li, J.X.; Shi, C.H.; Zhang, H.F.; Zhang, X.F.; Wei, Y.Y.; Jiang, K.; Zhang, B.G. Silicalite-1 zeolite membrane: Synthesis by seed method and application in organics removal. *Chemosphere* **2019**, *218*, 984–991. [CrossRef] [PubMed]
26. Wu, A.; Tang, C.Y.; Zhong, S.L.; Wang, B.; Zhou, J.J.; Zhou, R.F. Synthesis optimization of (h0h)-oriented silicalite-1 membranes for butane isomer separation. *Sep. Purif. Technol.* **2019**, *214*, 51–60. [CrossRef]
27. Heitmann, G.P.; Dahlhoff, G.; Hölderich, W.F. Catalytically active sites for the Beckmann rearrangement of cyclohexanone oxime to ε-Caprolactam. *J. Catal.* **1999**, *186*, 12–19. [CrossRef]
28. Lanzafame, P.; Barbera, K.; Perathoner, S.; Centi, G.; Aloise, A.; Migliori, M.; Macario, A.; Nagy, J.B.; Giordano, G. The role of acid sites induced by defects in the etherification of HMF on Silicalite-1 catalysts. *J. Catal.* **2015**, *330*, 558–568. [CrossRef]
29. Shi, L.H.; Liu, G.D.; Guo, H.C. Efficient Pt/Silicalite-1 catalyst for isomerization of *n*-heptane. *Catal. Commun.* **2017**, *101*, 111–115. [CrossRef]
30. Wang, D.; Wang, J.F.; Lu, C.Y.; Zou, X.L.; Cheng, H.W.; Ning, J.Y.; Lu, X.G.; Zhou, Z.F. Hydrogen production from coke oven gas by CO_2 reforming over a novel Ni-doped Silicalite-1. *Catal. Lett.* **2018**, *148*, 1424–1434. [CrossRef]
31. Niu, R.Y.; Liu, P.C.; Li, W.; Wang, S.; Li, J.P. High performance for oxidation of low-concentration methane using ultra-low Pd in silicalite-1 zeolite. *Micropor. Mesopor. Mater.* **2019**, *284*, 235–240. [CrossRef]
32. Sang, S.; Chang, F.; Liu, Z.; He, C.; He, Y.; Xu, L. Difference of ZSM-5 zeolites synthesized with various templates. *Catal. Today* **2004**, *93–95*, 729–734. [CrossRef]
33. Zaki, M.I.; Fouad, N.E.; Leyrev, J.; Knözinger, H. Physicochemical investigation of calcined chromia-coated silica and alumina catalysts—Characterization of chromium-oxygen species. *Appl. Catal.* **1986**, *21*, 359–377. [CrossRef]
34. Grzybowska, B.; Sloczynski, J.; Grabowski, R.; Wcislo, K.; Kozlowska, A.; Stoch, J.; Zielinski, J. Chromium oxide alumina catalysts in oxidative dehydrogenation of isobutane. *J. Catal.* **1998**, *178*, 687–700. [CrossRef]
35. Gao, B.; Luo, Y.J.; Miao, C.X.; Yue, Y.H.; Yang, W.M.; Hua, W.M.; Gao, Z. Oxidative dehydrogenation of 1-butene to 1,3-butadiene using CO_2 over Cr-SiO_2 catalysts prepared by sol-gel method. *Chem. Res. Chin. Univ.* **2018**, *34*, 609–615. [CrossRef]
36. Weckhuysen, B.M.; Wachs, I.E.; Schoonheydt, R.A. Surface chemistry and spectroscopy of chromium in inorganic oxides. *Chem. Rev.* **1996**, *96*, 3327–3349. [CrossRef]
37. Gao, X.; Bare, S.R.; Weckhuysen, B.; Wachs, I.E. In situ spectroscopic investigation of molecular structures of highly dispersed vanadium oxide on silica under various conditions. *J. Phys. Chem. B* **1998**, *102*, 10842–10852. [CrossRef]
38. Takehira, K.; Ohishi, Y.; Shishido, T.; Kawabata, T.; Takaki, K.; Zhang, Q.H.; Wang, Y. Behavior of active sites on Cr-MCM-41 catalysts during the dehydrogenation of propane with CO_2. *J. Catal.* **2004**, *224*, 404–416. [CrossRef]
39. Cherian, M.; Rao, M.S.; Yang, W.T.; Jehng, J.M.; Hirt, A.M.; Deo, G. Oxidative dehydrogenation of propane over Cr_2O_3/Al_2O_3 and Cr_2O_3 catalysts: Effects of loading, precursor and surface area. *Appl. Catal. A* **2002**, *233*, 21–33. [CrossRef]

40. Yim, S.D.; Nam, I.S. Characteristics of chromium oxides supported on TiO_2 and Al_2O_3 for the decomposition of perchloroethylene. *J. Catal.* **2004**, *221*, 601–611. [CrossRef]
41. Zhu, Q.J.; Takiguchi, M.; Setoyama, T.; Yokoi, T.; Kondo, J.N.; Tatsumi, T. Oxidative dehydrogenation of propane with CO_2 over Cr/H[B]MFI catalysts. *Catal. Lett.* **2011**, *141*, 670–677. [CrossRef]
42. Ye, X.N.; Hua, W.M.; Yue, Y.H.; Dai, W.L.; Miao, C.X.; Xie, Z.K.; Gao, Z. Ethylbenzene dehydrogenation to styrene in the presence of carbon dioxide over chromia-based catalysts. *New J. Chem.* **2014**, *28*, 373–378. [CrossRef]
43. Barbera, K.; Bonino, F.; Bordiga, S.; Janssens, T.V.W.; Beato, P. Structure-deactivation relationship for ZSM-5 catalysts governed by framework defects. *J. Catal.* **2011**, *280*, 196–205. [CrossRef]
44. Liu, G.D.; Liu, J.X.; He, N.; Miao, C.L.; Wang, J.L.; Xin, Q.; Guo, H.C. Silicalite-1 zeolite acidification by zinc modification and its catalytic properties for isobutane conversion. *RSC Adv.* **2018**, *8*, 18663–18671. [CrossRef]
45. Zhao, H.H.; Song, H.L.; Chou, L.J.; Zhao, J.; Yang, J.; Yan, L. Insight into the structure and molybdenum species in mesoporous molybdena–alumina catalysts for isobutane dehydrogenation. *Catal. Sci. Technol.* **2017**, *7*, 3258–3267. [CrossRef]
46. Zecchina, A.; Bordiga, S.; Spoto, G.; Marchese, L.; Petrini, G.; Leofanti, G.; Padovan, M. Silicalite characterization. 1. Structure, adsorptive Capacity, and IR spectroscopy of the framework and hydroxyl modes. *J. Phys. Chem.* **1992**, *96*, 4985–4990. [CrossRef]
47. Benamor, T.; Michelin, L.; Lebeau, B.; Marichal, C. Flash induction calcination: A powerful tool for total template removal and fine tuning of the hydrophobic/hydrophilic balance in SBA-15 type silica mesoporous materials. *Micropor. Mesopor. Mater.* **2012**, *147*, 370–376. [CrossRef]
48. Nakagawa, K.; Kajita, C.; Ikenaga, N.; Nishitani-Gamo, M.; Ando, T.; Suzuki, T. Dehydrogenation of light alkanes over oxidized diamond-supported catalysts in the presence of carbon dioxide. *Catal. Today* **2003**, *84*, 149–157. [CrossRef]
49. Mimura, N.; Okamoto, M.; Yamashita, H.; Oyama, S.T.; Murata, K. Oxidative dehydrogenation of ethane over Cr/ZSM-5 catalysts using CO_2 as an oxidant. *J. Phys. Chem. B* **2006**, *110*, 21764–21770. [CrossRef]
50. Zhang, F.; Wu, R.X.; Yue, Y.H.; Yang, W.M.; Gu, S.Y.; Miao, C.X.; Hua, W.M.; Gao, Z. Chromium oxide supported on ZSM-5 as a novel efficient catalyst for dehydrogenation of propane with CO_2. *Micropor. Mesopor. Mater.* **2011**, *145*, 194–199. [CrossRef]
51. Butt, T.; Tosheva, L. Synthesis of colloidal silicalite-1 at high temperatures. *Micropor. Mesopor. Mater.* **2014**, *187*, 71–76. [CrossRef]
52. Smith, M.A.; Zoelle, A.; Yang, Y.; Rioux, R.M.; Hamilton, N.G.; Amakawa, K.; Nielsen, P.K.; Trunschke, A. Surface roughness effects in the catalytic behavior of vanadia supported on SBA-15. *J. Catal.* **2014**, *312*, 170–178. [CrossRef]

catalysts

MDPI

Article

H-ZSM-5 Materials Embedded in an Amorphous Silica Matrix: Highly Selective Catalysts for Propylene in Methanol-to-Olefin Process

Huda Sharbini Kamaluddin, Sulaiman Nassir Basahel, Katabathini Narasimharao * and Mohamed Mokhtar *

Surface Chemistry and Catalytic Studies (SCCS) Group, Department of Chemistry, King AbdulAziz University, Jeddah 21589, Saudi Arabia; hudashkamaluddin@gmail.com (H.S.K.); sbasahel@hotmail.com (S.N.B.)

* Correspondence: nkatabathini@kau.edu.sa (K.N.); mmoustafa@kau.edu.sa (M.M.); Tel.: +96-65-3863-8994 (K.N.); +96-65-0055-8045 (M.M.)

Received: 15 March 2019; Accepted: 13 April 2019; Published: 17 April 2019

Abstract: H-ZSM-5 materials embedded in an amorphous silica were successfully synthesized with three different Si/Al ratios (i.e., 40, 45, and 50). The presence of the MFI structure in the synthesized samples was confirmed by X-ray diffraction (XRD), Fourier transform infra-red (FT-IR), and solid state-nuclear magnetic resonance (SSNMR) techniques. The morphology and textural properties of the samples were investigated by scanning electron microscopy (SEM), TEM, and N_2-physisorption measurements. Furthermore, acidic properties of the synthesized catalysts have been studied by NH_3-TPD and FT-IR spectroscopy of CO adsorption studies. Variation of the Si/Al ratio affected the crystal morphology, porosity, and particle size, as well as the strength and distribution of acid sites. The synthesized zeolite materials possessed low acid-site density and exhibited high catalytic activity in the methanol-to-olefin (MTO) reaction. To study the intermediate species responsible for catalyst deactivation, the MTO reaction was carried out at high temperature (500 °C) to accelerate catalyst deactivation. Interestingly, the synthesized catalysts offered high selectivity towards the formation of propylene ($C_{3=}$), in comparison to a commercial microporous crystalline H-ZSM-5 with Si/Al = 40, under the same reaction conditions. The synthesized H-ZSM-5 materials offered a selectivity ratio of $C_{3=}/C_{2=}$ 12, while it is around 2 for the commercial H-ZSM-5 sample. The formation of hydrocarbon species during MTO reaction over zeolite samples has been systematically studied with operando UV-vis spectroscopy and online gas chromatography. It is proposed that the strength and type of acid sites of catalyst play a role in propylene selectivity as well as the fast growing of active intermediate species. The effective conversion of methanol into propylene in the case of synthesized H-ZSM-5 materials was observed due to possession of weak acid sites. This effect is more pronounced in H-ZSM-5 sample with a Si/Al ratio of 45.

Keywords: mesoporous H-ZSM-5; methanol-to-olefin (MTO); propylene; acid sites density; operando UV-vis spectroscopy

1. Introduction

Propylene is one of the most important base chemicals in chemical industries. Due to the high demand for propylene, the development of more selective catalysts for the methanol-to-olefin (MTO) process is highly desired [1,2]. So far, crystalline zeolite and zeolite-like materials have been the most studied catalysts in the MTO reaction, due to their unique physico-chemical properties, including acidity, topology, and shape selectivity [3–5] Usually, zeolites with 8- to 10-membered rings, such as H-SAPO-34 (CHA) and H-ZSM-5 (MFI), have been used as selective and stable catalysts for the MTO process [6,7]. Therefore, many researchers have explored different strategies to synthesize zeolites

with different structures (particularly MFI and CHA) to improve propylene selectivity. The zeolite topology, e.g., structure, 1-, 2-, 3-dimention, shape, cage size, and channel system, affect the nature of the retained hydrocarbon pool that formed during MTO reaction, and, accordingly, the olefin product selectivity [8,9]. In addition to the effort of forming high selectivity towards propylene, Palčić et al. [10] studied the effect of crystallization temperature (170, 150, 120, and 100 °C) on the ZSM-5 properties. They observed that the decrease in the crystallization temperature 100 °C led to significant changes in zeolite properties exhibiting many framework defects with decrease in acid-site density, decrease in their strength, and larger external surface area. Those properties affected to the product selectivity in MTO reaction, and show a $C_{3=}/C_{2=}$ = 6 with high selectivity towards propylene (53%). Moreover, Losch et al. [11] studied the effect of external surface passivation of ZSM-5 by chemical liquid deposition on its C_2-C_3 selectivity. A 10–30% increase in the C_2-C_3 selectivity was recorded for the passivated zeolites.

The MTO process is known to be greatly influenced by the Brønsted acid sites presented in the solid catalyst. The Brønsted and Lewis acid sites exist in the zeolites due to presence of tetrahedral framework Al atoms and/or silanol (Si–OH) groups within framework and extra-framework Al species [12]. It was suggested that existence of Brønsted and Lewis acid sites could lead to synergistic effects between the two types of acid sites [13]. Corma et al. [14] and Mirodatos et al. [13] proposed the mechanism of synergistic effect between two types of acid sites; the authors indicated that the extra-framework Al species directly interact with the acidic –OH groups, which involves partial electron transfer from O–H groups to the oxoaluminum species (AlO^+ and AlOOH). The electron transfer lead to delocalization of electron density around the O-atom, which is very similar to the super-acid systems ($AlCl_3$-HCl and SbF_5-HF).

It has also been reported that reactions of hydrocarbons over the strong Brønsted acid sites located on the outer surface of zeolite particles cause external coke deposition, leading to a short lifetime of catalysts [15]. Many efforts have already been reported to nullify the adverse effects of acid sites by minimizing the inner density of acid sites within the structure to prevent non-selective catalytic activity in the MTO process. Hadi et al. [16] used ion exchange procedure to exchange some acidic H^+ ions in the framework with Ca, Mn, Cr, Fe, Ni, Ag, and Ce ions. Some other strategies, such as changing the medium of zeolite preparation (fluoride route) [17], altering Si/Al ratio, synthesizing distorted zeolite framework, building hierarchical zeolite materials [1,18,19], preparing composite molecular sieves [20,21], and synthesizing the nanosheet framework to decrease long channels [22], were employed. In addition, several research groups focused on tuning the reaction conditions, e.g., increasing the reaction temperature, decreasing the partial pressure of methanol, changing the reactor design [23], and introducing a co-feed of methanol containing water to the MTO reaction [24]. Consequently, selectivity towards light olefins can be increased by decreasing the selectivity towards aromatic products [25]. Yarulina et al. [26] incorporated Ca into ZSM-5 structure and observed an increase of propylene selectivity. The authors claimed that modification with Ca^{2+} resulted in a decrease in the acidity of the zeolite. As a result, the rate of hydride transfer and oligomerization reactions on these sites is greatly reduced, causing the suppression of ethylene selectivity. In another report, Yarulina et al. [27] also studied the effect of acidity on the catalytic activity of the ZSM-5 for the MTO process; the authors observed that the introduction of Lewis acid sites averts coke formation, thus enhancing the lifetime of the catalyst and also observing that the isolation of Brønsted acid sites is essential to increase propylene selectivity.

Several decades ago, Jacobs et al. [28] reported the existence of X-ray amorphous ZSM-5 material, which contained zeolite particles of less than 8 nm sizes embedded in an amorphous matrix of silica. Later, Nicolaides [29] reported the synthesis of substantially amorphous ZSM-5 materials at various temperatures under autogenous pressure. Triantafyllidis et al. [30] reported the hydrothermal synthesis of X-ray amorphous samples at temperature as low as 25 °C. The authors observed that the materials consisted of well-formed particles of almost spherical shape and with dimensions of about 20–30 nm. Corma and Daiz-Caban [31] also synthesized amorphous zeolite materials using the self-assembly of organic structure-directing agents. Significant efforts have been made to synthesize

ZSM-5 materials embedded in amorphous silica without using any seeding agent [32]. Kim and Kim [33] successfully synthesized ZSM-5 materials in the absence of template or seeding agent using two-step temperature technique. Recently, a modified method for the synthesis of an amorphous ZSM-5 has been reported by Yeong et al. [34]. Our group also synthesized ZSM-5 materials containing amorphous silica matrix using aluminum nitrate as Al source for the first time without using any organic template [35]. Many research groups have reported on the synthesis and characterization of ZSM-5 materials embedded in amorphous silica, but these materials were not explored for catalytic application in the MTO process [36].

In this research, H-ZSM-5 materials with different Si/Al ratios (40, 45, and 50) embedded in amorphous silica were synthesized; the acid-site density of the H-ZSM-5 materials decreased by intercepting the crystallization process and making use of a unified crystallization time of 16 h. The physico-chemical properties were studied by different methods and the materials were used as catalysts in the MTO process. It is also our aim to understand the intermediate species responsible for catalyst deactivation in the MTO process at high temperature; therefore, the catalytic performance of the synthesized materials was studied at 500 °C. Furthermore, we used a combination of operando UV-vis spectroscopy and online gas chromatography to correlate and elucidate the catalytic activity with the formation of different active and deactivating hydrocarbon species generated in the catalyst bed.

2. Results and Discussion

2.1. Structure, Morphology, and Porosity of Synthesized Materials

Figure 1 shows powder X-ray diffraction (XRD) patterns of the H-ZSM-5 materials embedded in amorphous silica along with a commercial Zeolyst sample. The synthesized materials exhibited major reflections in the ranges of 2θ = 8–11° and 27–30° corresponding to the MFI structure [ICDD file no. 41–1478]. The XRD patterns also show additional broad humps corresponding to silica, indicating that the synthesized samples are composed of both ZSM-5 and silica phases. It is clear from Figure 1 that the intensity of the reflections of the MFI-40 sample is higher than those of the MFI-45 and MFI-50 samples. This observation indicates that the Si/Al ratio of the synthesized materials has an influence on the crystal size of ZSM-5 structure; crystallite increased with the increase of Si/Al ratio (Table 1).

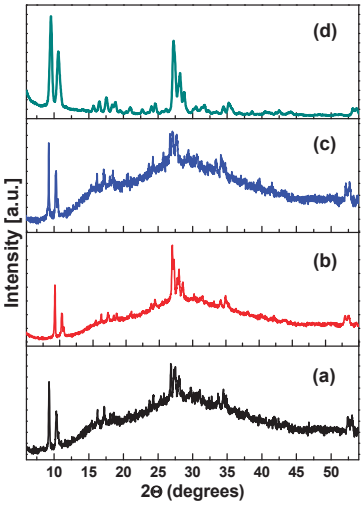

Figure 1. Powder X-ray diffraction (XRD) patterns of the synthesized samples; (**a**) MFI-40, (**b**) MFI-45, (**c**) MFI-50, and (**d**) Zeolyst.

Table 1. Crystallite size, chemical composition, and textural properties for synthesized H-ZSM-5 and Zeolyst samples.

Sample	Si/Al Ratio [a]	Average Crystal Size (nm) [b]	S_{BET} [c] (m^2/g)	S_{micro} (m^2/g)	S_{meso} (m^2/g)	V_{Total} [d] (cm^3/g)	V_{micro} [e] (cm^3/g)	V_{meso} [f] (cm^3/g)	Hierarchy Factor [g]
MFI-40	42	89	383	358	45	0.901	0.039	0.862	0.005
MFI-45	46	126	403	322	81	1.141	0.042	1.099	0.007
MFI-50	53	140	420	347	73	1.057	0.049	1.008	0.008
Zeolyst	40	63	262	115	147	0.115	0.098	0.017	0.478

[a] ICP-MS analysis; [b] estimated from XRD analysis; [c] Brunauer-Emmett-Teller (BET) surface area; [d] Total pore volume at P/P_o = 0.997; [e] Micropore volume from *t*-plot; [f] $V_{meso} = V_{Total} - V_{micro}$; [g] Hierarchy factor = $(V_{micro}/V_{Total}) \times (S_{meso}/S_{BET})$.

Fourier transform infra-red (FT-IR) spectral analysis was used to confirm the presence of the MFI structure in the synthesized samples, since Jacobs et al. [28] indicated that XRD should be used with caution for ZSM-5 materials embedded in an amorphous silica. The authors recommended the FT-IR technique to determine the MFI structure as the vibrations of the zeolite skeleton are intense even for agglomerates of a few unit cells. Figure S1 shows the FT-IR spectra of the synthesized materials along with Zeolyst ZSM-5 sample. A band at ~550 cm^{-1} was observed in all the samples, which corresponds to the vibration of a five-membered ring (Pentasil) for the MFI structure [37]; however, the intensity of this band decreased with increasing Si/Al ratio. Furthermore, a broad band at around 1060 cm^{-1} due to an internal vibration of (Si,Al) O_4 tetrahedron (T) of the MFI structure was also observed for the synthesized samples. These results clearly indicate the presence of MFI structure in synthesized H-ZSM-5 samples. FT-IR analysis was also used to study the characteristics of different hydroxyl groups presented in the MFI framework of the samples (Figure 2).

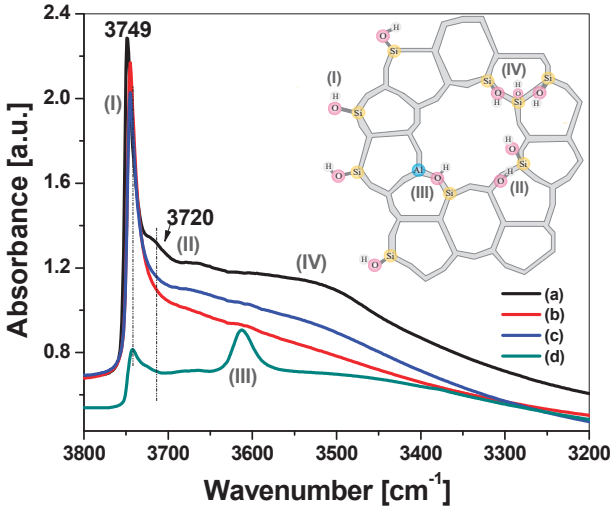

Figure 2. Fourier transform infra-red (FT-IR) spectra for studied materials (**a**) MFI-40; (**b**) MFI-45; (**c**) MFI-50 and (**d**) Zeolyst.

The analysis was performed after outgassing the samples at 300 °C under vacuum. The band at 3749 cm^{-1} (I) corresponds to the external Si-OH groups and the intensity of this band is very low in the case of the Zeolyst compared to synthesized samples. It was proposed that appearance of the intense band at 3749 cm^{-1} is an indication of the amorphous nature of the samples with low Al content that possessed high external surface area [17,38,39]. The IR band for terminal isolated Si-OH groups at 3720 cm^{-1} (II) are clearly observed as a weak shoulder in the case of the Zeolyst and MFI-40 samples. The shoulder is very weak and broad in the Zeolyst compared with the MFI-40 sample. The intense IR

band at 3612 cm^{-1} (III) corresponding to the internal vibration of Brønsted acid sites [38], which is very sharp in Zeolyst sample compared to synthesized H-ZSM-5 samples, indicates the presence of high density of Brønsted acid sites in the Zeolyst sample. Interestingly, a broad envelope appeared centered at ~3500 cm^{-1} (IV) related to Si-OH nests that comprised many Si-OH groups interacting through extended H-bonding, and this type of nest generally forms at crystal steps or extended defects [38]. Among studied samples, the MFI-40 sample exhibited the broadest envelope.

The morphology of the synthesized samples was investigated using the scanning electron microscopy (SEM) technique. The SEM images of the samples are shown in Figure 3. The MFI-40 and MFI-45 samples contained crystalline MFI particles with a polygon shape surrunded by amorphous material. On the other hand, the MFI-50 sample possessed agglomerated particles with no definite shape along with a large amount of amorphous material. Interestingly, the large particles presented in MFI-45 and MFI-50 samples did not represent the normal shape (coffin-like) of ZSM-5 crystals due to modified synthesis conditions. The Zeolyst sample showed presence of very large crystalline particles several micrometers in length and width.

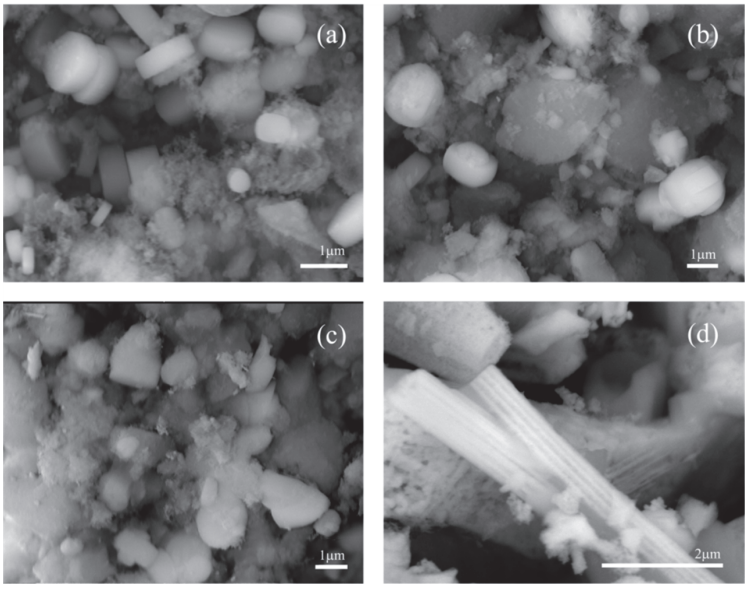

Figure 3. Scanning electron microscopy (SEM) images of the studied samples (**a**) MFI-40, (**b**) MFI-45, (**c**) MFI-50 and (**d**) Zeolyst.

The N_2 adsorption-desorption isotherms of synthesized H-ZSM-5 and commercial Zeolyst samples are shown in Figure 4A. The pore-size distribution patterns, which were derived from the adsorption branches using the Non-Local Density Functional Theory (NLDFT) method, are shown in Figure 4B. The Zeolyst sample shows mixed type I and type IV isotherms according to the classification of international union of pure and applied chemistry (IUPAC), with a distinct hysteresis loop at relative pressure range between P/P_o = 0.4 and 0.95, with a sharp increase of N_2 uptake between P/P_o = 0.95 and 1.0, which are the characteristics of materials with micro- and meso-pores. This is verified by the NLDFT pore-size distribution pattern of Zeolyst sample, where there is a sharp peak below 20 Å (micropores) and a minor hump in the mesoporous range.

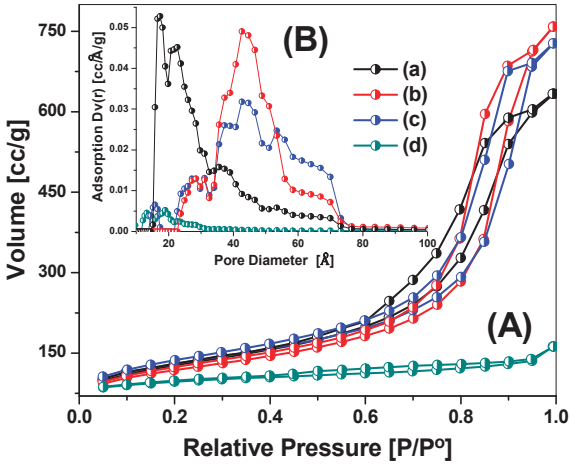

Figure 4. (**A**) N_2 adsorption-desorption isotherms and (**B**) pore-size distribution patterns of (**a**) MFI-40, (**b**) MFI-45, (**c**) MFI-50 and (**d**) Zeolyst.

The synthesized H-ZSM-5 (MFI-40, MFI-45 and MFI-50) samples showed type IV isotherms, with a hysteresis loop at relative pressures higher than $P/P_o = 0.4$, which is typical for mesoporous materials. These hysteresis loops are due to the capillary condensation in the mesopore void spaces [40]. The dramatic increase in the adsorption amounts at high relative pressure compared with isotherm of the commercial H-ZSM-5 sample is mainly due to the generation of mesopores due to voids in the three samples. Table 1 shows the Brunauer-Emmett-Teller (BET) surface area (S_{BET}), micropore surface area (S_{micro}), mesopore surface area (S_{meso}), total pore volume (V_{total}) micropore volume (V_{micro}), and mesopore volume (V_{meso}) of all the investigated samples. Their BET surface areas, total pore volumes, and mesopore volumes are higher than the commercial H-ZSM-5 sample (Table 1). The mesoporous volume for partially crystalline samples increases in the following order: MFI-40 < MFI-50 < MFI-45. The major difference between the synthesized H-ZSM-5 embedded in silica and Zeolyst sample is the presence of non-crystallographic intracrystalline mesopores resulting in the high porosity of synthesized zeolite compared to the conventional zeolite. Trintafyllidis et al. [30] indicated that the mesoporous nature could be due to the presence of some impurities, such as amorphous silica-alumina. It can be concluded that the sudden-stop of the crystallization process during synthesis to get mesoporous ZSM-5 is a very effective method.

To study the nature of Al and Si coordination sites, solid-state ^{27}Al and ^{29}Si MAS NMR spectra for the investigated samples were obtained. The ^{27}Al MAS NMR spectra for all the samples are shown in Figure 5A. The spectra exhibited two sharp NMR resonances centered at 56.1 ppm and 0 ppm corresponding to the Al^{IV} species presented in the framework of zeolite in a tetrahedral coordination [41] and Al^{VI} presented outside the zeolite framework in an octahedral coordination [42], respectively. The intensity of the resonance at 56.1 ppm for the synthesized ZSM-5 samples is low in comparison with the Zeolyst sample. This observation indicates that the incorporation of Al in the MFI framework is lower in synthesized samples compared to Zeolyst sample. The octahedral coordinated Al species, most probably existing in extra-framework position ($EFAl^+$), were dominant especially for the synthesized materials [43]. Deconvolution of the ^{29}Si MAS NMR spectra for all samples was performed in Figure 5B. All the samples showed a major resonance at −112 ppm; evidently a strong signal corresponding to Si(4Si) of Q_4 at high field side was shown in all high siliceous zeolites samples [44]. The other types of Si species such as Si attached to one, two, three, or four Al atoms through oxygens could be observed as shoulders [45]. In addition, the occurrence of a silanol group (Si-OH) led to a change in the coordination, Q_4, Q_3, Q_2 and chemical shift of about +10 ppm/OH [12]. The Zeolyst

sample showed only one small shoulder at −103.2 ppm, which could be assigned to Si(3Si,1Al) sites [41]. On the other hand, the synthesized samples showed two shoulders, the first one in the range of −103.2 ppm to −105 ppm, indicating the existence of Si atoms with chain and chain-branching structure Si(3Si,1Al) and Si(2Si,2Al), overlapped with Q_3 and Q_2 of Si-OH, respectively [46], and the second one in the range of −90. 2 ppm to −99 ppm, which is ascribed to $AlOSi^*(OSi)_3$ and/or $HOSi^*(OSi)_3$ of Q_3 signal [47]. Moreover, there are minute resonances recorded below −100 ppm, which correspond to Si(2Si,2Al) atoms indicating the presence of Al-O-Si-O-Al sequences in minor quantities in the synthesized samples [42].

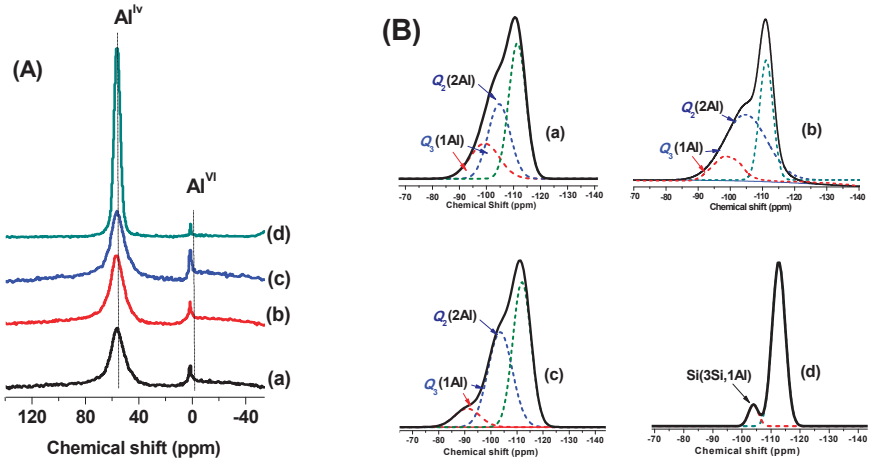

Figure 5. (**A**) ^{27}Al MAS NMR and (**B**) deconvoluted ^{29}Si MAS NMR of (**a**) MFI-40, (**b**) MFI-45, (**c**) MFI-50, and (**d**) Zeolyst samples.

Increase of Si/Al ratio of samples resulted in an increase of the intensity of the resonance at −112 ppm [Si(4Si) species] and the decrease of the intensity of shoulder in the range of −90. 2 ppm to −99 ppm [$AlOSi^*(OSi)_3$] species indicating a decrease in the number of Al framework species (Table 2). Combining the ^{27}Al and ^{29}Si MAS NMR spectral results, it is clear that the synthesized samples possessed both MFI and amorphous silica phases and increase of Si/Al ratio resulted in the formation of Si(4Si) sites and extra-framework Al species. The MAS NMR results clearly indicate that Si/Al ratio has an influence on the coordination of Al and Si atoms, which could subsequently affect the acidic properties of the samples.

Table 2. Types of Aluminum and total number of acid sites for studied samples.

Sample	% Al^{IV}_{FAl} *Atoms* [a]	% Al^{IV}_{EFAl} *Atoms* [b]	Total Number of Acid Sites (mmoL g^{-1}) [c]
MFI-40	90.44	9.56	0.25
MFI-45	78.20	21.80	0.28
MFI-50	67.34	32.34	0.16
Zeolyst	95.13	4.87	0.39

[a, b] Framework (*FAl*) and non-framework (*EFAl*) of Al atoms are estimated from ^{29}Si MAS NMR; [c] number of acid sites estimated from NH_3-TPD analysis.

2.2. Acidity Measurnments

The NH_3 desorption temperature is directly indicative of a strength of acid sites presented in the samples [48]. The synthesized H-ZSM-5 samples exhibited different NH_3-TPD profiles compared to the Zeolyst sample (Figure S2). Two major NH_3 desorption peaks were observed for the Zeolyst sample with maxima at 175 °C and 370 °C indicating the presence of weak and strong acid sites, respectively.

A decrease of the total acidity of the synthesized zeolite samples as measured by a lower amount of NH_3 desorbed (Figure S2 and Table 2), indicating the decrease in number and strength of the acid sites in the synthesized samples compared to the Zeolyst sample. Furthermore, we studied the acidic properties of samples by using CO as a probe molecule; it is known that CO has several advantages as a probe molecule such as weak basicity, small diameter, and high sensitivity to IR frequency [49]. Figure 6 shows FT-IR spectra of all the investigated samples after CO adsorption. The spectra were divided into two regions—spectra in the range of 3800–3100 cm^{-1} (a) and in the range of 2250–2100 cm^{-1} (b).

The FT-IR spectra presented in red correspond to the samples treated at 300 °C under vacuum. The upper spectra in blue are related to the highest CO pressure and the grey spectra in between are the set of spectra recorded with increase of CO pressure. For the Zeolyst sample, the intensity of the band at 3612 cm^{-1} corresponding to Si-OH-Al species (Brønsted acid sites) is clearly decreased with the increase of CO pressure. A new band clearly appeared at 3276 cm^{-1}, which could be attributed to CO coordinated to Si–OH–Al groups, Figure 6a. It can be seen that the intensity of the 3276 cm^{-1} band increased with an increase of CO pressure, indicating the higher strength of Brønsted acid sites in the Zeolyst sample. The intensity of the band at 3742 cm^{-1}, which is due to internal isolated Si–OH groups including a shoulder at 3722 cm^{-1}, decreased and another new band, due to formation of Si–OH–CO species, was clearly observed at 3641 cm^{-1}. Bleken et al. [22] reported very similar observations in the case of CO adsorbed on H-ZSM-5 nanosheet samples. The major difference between synthesized H-ZSM-5 samples and Zeolyst sample is that the synthesized samples exhibited a low-intensity band at 3612 cm^{-1}, which indicated that the synthesized samples possessed a lower density of Brønsted acid sites [38].

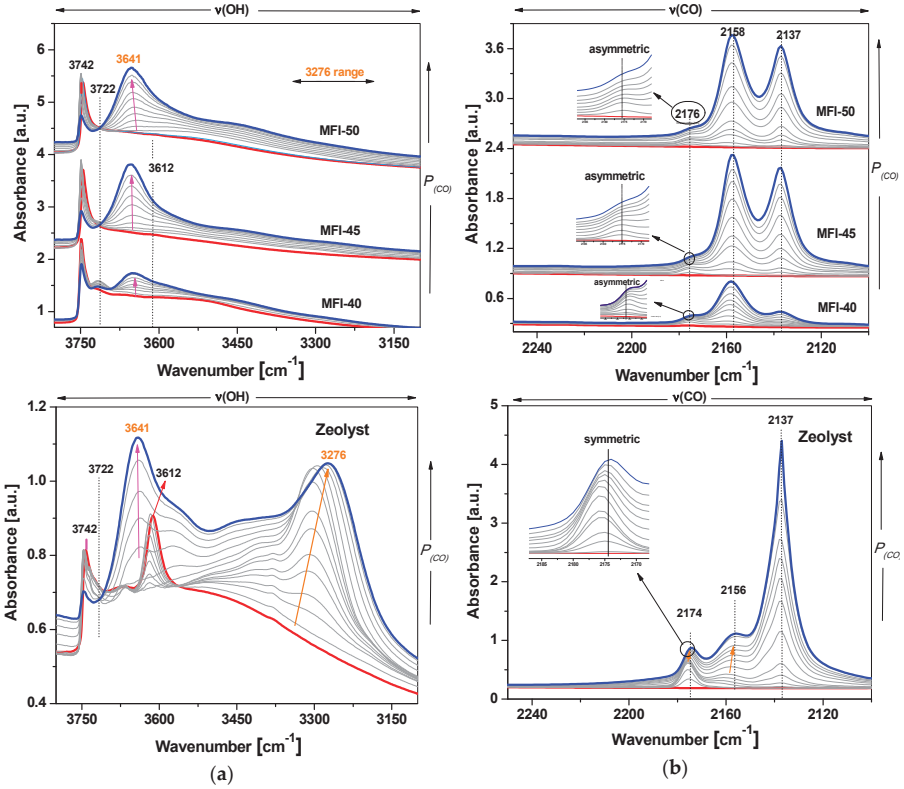

Figure 6. The FT-IR spectra after CO adsorption for synthesized H-ZSM-5 and Zeolyst samples; (**a**) in the range of 3800–3100 cm^{-1}, and (**b**) in the range of 2250–2100 cm^{-1}.

It was also reported that the IR absorption band at 2175 cm^{-1} could be due to CO interaction with Si-OH-Al groups [39]. This band was observed in the Zeolyst sample as well as in synthesized H-ZSM-5 samples. Leydier et al. [50] reported that amorphous silica-alumina materials showed the band at 2175 cm^{-1} with a tail, due to the adducts formed by -OH groups and framework Al sites on the external surfaces. Very similar FT-IR spectra were observed in the case of synthesized H-ZSM-5 samples. With the increase of CO pressure, the intensity of the band at 2175 cm^{-1} was also increased. From Figure 6b, we can notice that the most intense band was observed in the MFI-40 sample and the intensity decreased with the increase of Si/Al ratio. The band at 2175 cm^{-1} is sharp and symmetric in the case of the Zeolyst sample than the synthesized H-ZSM-5 samples. This is an indication of a homogeneous distribution of strong Brønsted acid sites in the Zeolyst sample, but not in the synthesized samples. Two additional bands appeared at 2158 cm^{-1} and 2137 cm^{-1} could be attributed to CO adsorbed on Si-OH species [51] and CO condensed in the pores of the zeolites [17,38,39], respectively. The band at 2137 cm^{-1} is sharp and intense in case of the Zeolyst sample, indicating that more CO molecules were trapped inside the micropores of the sample. However, synthesized H-ZSM-5 samples showed low peak areas under 2137 cm^{-1} peak compared to the Zeolyst sample (Figure S3 and Table S1), which is an indication that the synthesized samples possessed shortened channels with mesopores.

2.3. Catalytic Performance in the MTO Reaction

The catalytic performance of the samples was evaluated for the MTO reaction at 500 °C using a weight hourly space velocity (WHSV) of 3.0 h^{-1}. The methanol conversion and selectivity to different products for all the samples are presented in Figure 7.

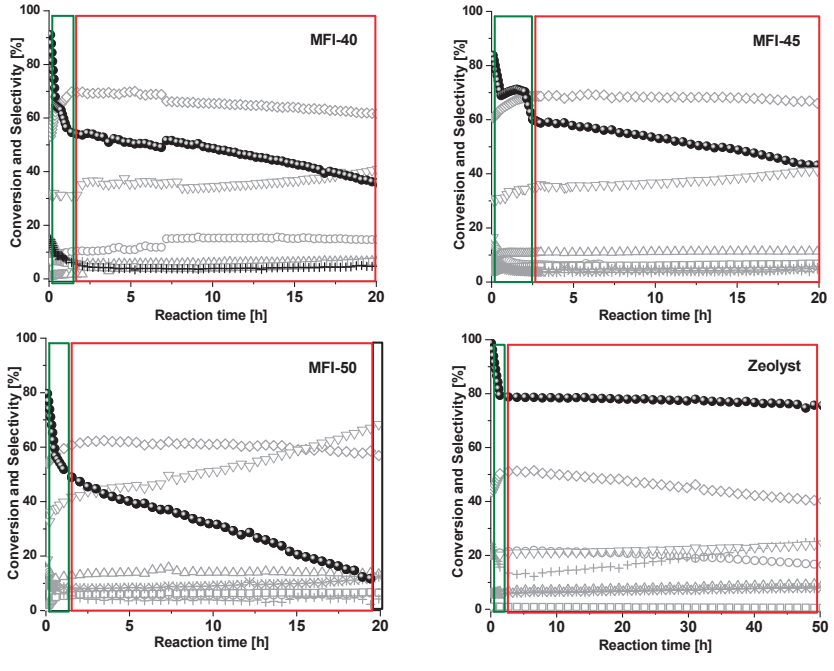

Figure 7. Methanol conversion and selectivity patterns of catalysts for the MTO reaction; reaction temperature: 500 °C and WHSV: 3 h^{-1}; (●) Methanol conversion, (○) $C_{2=}$, (◊) $C_{3=}$, (Δ) $C_{4=}$, (□) $C_{5=}$, (▽) DME, (*) paraffin, and (+) aromatics selectivity. The green region corresponds to the initial stage of reaction; where the products formation is initiated, the red region indicates to the stable/slower deactivation; where the products formation reaches to steady state, and the black region relates to the deactivated stage, where the products formation decreased drastically (below 20%).

After a short induction period, the Zeolyst sample offered 80% conversion at 500 °C. Synthesized H-ZSM-5 samples offered lower methanol conversions (maximum 72%) and low stability. Among the synthesized samples, MFI-45 exhibited better stability compared to MFI-40 and MFI-50 catalysts. The drastic decrease of methanol conversion at the initial stage could be related to accumulation of non-active hydrocarbon species in the pores of ZSM-5 structure [52,53]. The selectivity to propylene ($C_{3=}$), for all synthesized H-ZSM-5 samples is higher compared to Zeolyst sample. At the initial stage of reaction, the synthesized H-ZSM-5 samples showed different selectivity values; MFI-40 and MFI-50 samples offered 54%, while MFI-45 sample offered 60.7%, respectively. On the other hand, the Zeolyst sample offered only 43.5%. However, the selectivity towards ethylene ($C_{2=}$), is higher in the case of the Zeolyst sample compared to all synthesized H-ZSM-5 samples as shown in Figure 7. The Zeolyst sample showed $C_{2=}$ selectivity of about ~20%, while all synthesized H-ZSM-5 samples offered below 10%; therefore, synthesized H-ZSM-5 samples are more selective towards propylene formation.

The synthesized H-ZSM-5 samples showed higher propylene/ethylene ($C_{3=}/C_{2=}$) ratio in comparison to the Zeolyst sample (Figure S4). Propylene selectivity of all synthesized H-ZSM-5 samples remain stable in a steady state for 22 h and start to decrease with further increase of reaction time. Among the three samples, the MFI-45 sample showed higher and stable propylene selectivity. There are some other products, such as $C_{4=}$, $C_{5=}$, paraffins and aromatics, and their selectivity remains stable (lower than 15%). The Zeolyst sample exhibited slightly higher selectivity for $C_{4=}$, $C_{5=}$, aromatics and paraffins. This is most probably due to the fact that the Zeolyst sample possessed relatively high strong acid sites, which favors hydride transfer reactions to form C_1-C_5, paraffins, and aromatics [54,55]. Operando UV-vis spectroscopy is a very useful tool to detect the formation of carbonaceous species within the catalysts during the MTO reaction. When methanol passes through the catalyst bed, UV-vis spectra were collected for every 20 s (Figure S5). The growing of the UV-vis bands is an indication for the formation of hydrocarbon pool (HCP) species within the H-ZSM-5 structure. It was reported that the MTO reaction is an indirect reaction and the reaction pathway involved the formation of a methoxy species, protonated dimethyl ether, and water [56], followed by formation of HCP species to obtain aromatics and higher alkenes [57,58].

Due to the complexity and broadness of operando UV-vis spectra, a non-negative matrix factorization (NNMF) analysis was applied to obtain a better insight of different intermediate HCP species and their kinetic behavior [57]. The NNMF analysis of operando UV-vis spectra was divided into two groups—UV-vis Eigen spectra, and kinetic behavior of the HCP species. Figure 8 represents UV-vis Eigen spectra of different HCP species formed within ZSM-5 structure. The Zeolyst sample exhibited two major absorption bands of active species at 590 nm and 747 nm, which could be assigned to phenanthrene/anthracene carbocation and pyrenes species, respectively [57]. Meanwhile, synthesized H-ZSM-5 samples showed major absorption bands at 450 nm, 575 nm, and 710 nm corresponding to methylated naphthalene carbocations, phenanthrene/anthracene carbocation, and pyrenes, respectively. All the catalyst samples exhibiting broad bands correspond to deactivated species (poly-methylated and poly-cyclic aromatic species) [57].

The evolution of intermediate species as a function of reaction time is presented in Figure 9. It is clear that the formation of active HCP and coke species are initiated at different reaction times. The Zeolyst and MFI-40 samples require around ~0.1 h to initiate the HCP species, while MFI-45 and MFI-50 samples initiated these species at 0.14 and 0.18 h, respectively (Table 3). It can be observed that the Zeolyst sample needs around 1.3 h to initiate the formation of the coke species. However, in the case of the MFI-40 sample, the coke species are initiated along with the HCP species at around 0.1 h; on the other hand, MFI-45 and MFI-50 catalysts required ~0.3 h to initiate the formation of coke species. The formation rate of the HCP species was calculated using the evolution of the active group at a specific time (~0.3 h) and is presented in Table 3. We observed that the MFI-45 sample exhibited high rate in growth of HCP species (showing average rate ~61 cg/h).

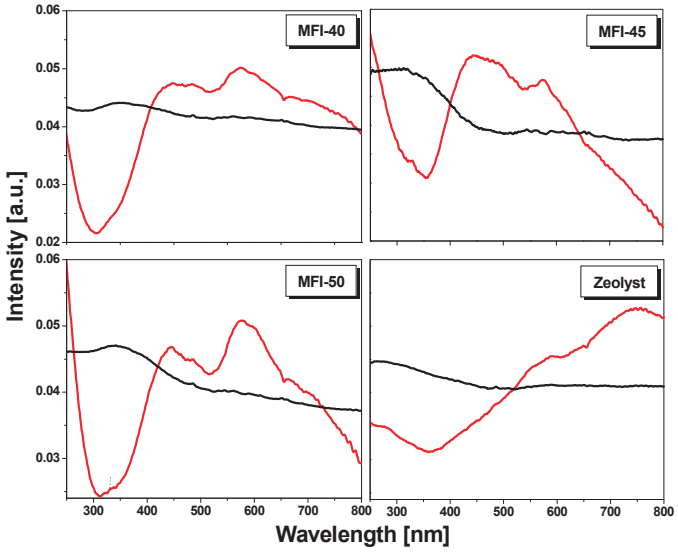

Figure 8. UV-vis Eigen spectra of investigated samples. Red colored spectra represent the active species, while black colored spectra represent the deactivated species, as determined by the NNMF method from operando UV-vis spectra.

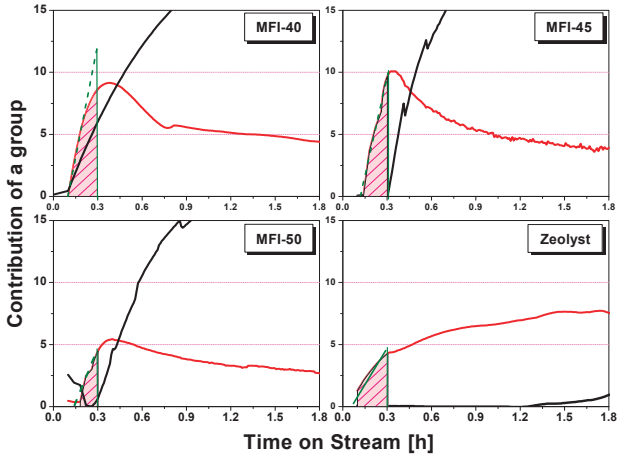

Figure 9. The evolution of intermediate species as a function of time; red represents the behavior of active species, while black represents the behavior of deactivated species.

Table 3. The average rate constant for the first formation of hydrocarbon pool and their initiation time [h].

Sample	Initiation Time for Active Species [h]	Initiation Time for Deactivating Species [h]	Average Rate for Growing of Active Species [cg/h^{-1}] [a]
MFI-40	0.10	0.1	45.5
MFI-45	0.14	0.3	61.5
MFI-50	0.18	0.3	37.0
Zeolyst	0.10	1.3	20.9

[a] cg/h: the contribution of active group per hour.

The dual-cycle concept is a widely accepted MTO mechanism for ZSM-5 materials, where ethylene is formed from an arene-based cycle, while propylene is formed from an olefin-based cycle [59] (Scheme S1) [60]. Therefore, the olefin distribution depends on which cycle is more dominant during the MTO reaction. It is well documented in the literature that the initiation of HCP species formation depends on the existence and the strength of Brønsted acid sites [61]. It was also observed that the generation of ethylene and formation of coke are dominant, if the catalyst possesses more strong Brønsted acid sites [54]. It was reported that both improved diffusion properties and lower acid strength are the reasons for observed high selectivity towards propylene in mesoporous ZSM-5 catalysts [62].

It is clear from the activity results that the active HCP species formation rate and the propylene selectivity are higher for all synthesized H-ZSM-5 samples, due to fact that these samples possessed low density of Brønsted acid sites. However, more Lewis acid sites ($EFAl^+$ species) were present in the synthesized samples compared to the Zeolyst sample. Corma et al. [14] and Mirodatos et al. [13] proposed that a synergistic effect exists between Brønsted and Lewis acid sites, and there is clear possibility that this synergistic effect played a role to obtain high rates of active HCP species formation in the case of synthesized H-ZSM-5 samples, especially in the MFI-45 sample. In addition, there is a limited hindrance from the structure in case of synthesized H-ZSM-5 samples. Therefore, the growth of HPC species was enhanced (from the intensity of bands of active HCP species). Presence of internal defect sites in synthesized samples is responsible for the formation of coke species along with the active HCP species at the beginning of the reaction. It was reported that the presence of internal defect sites enhances the accumulation of HCP species [38]. The propylene selectivity is higher at the beginning of the reaction in all the studied catalysts probably due to the fact that the intertwined alkene-arene-based cycle is dominant at this stage. By increasing the reaction time and more methanol exposure, the steady formation of propylene was observed in the case of synthesized H-ZSM-5 samples, which may be due to the domination of the alkene-based cycle. Consequently, the selectivity to other products for all synthesized H-ZSM-5 samples remains low in comparison with the Zeolyst sample. Therefore, we argue that the mechanism of the MTO reaction over synthesized H-ZSM-5 samples during the active stage is a cut-off dual-cycle process.

3. Experimental

3.1. Chemicals and Materials

The Si source, tetraethyl orthosilicate $SiC_8H_{20}O_4$ (>99%) and Al source, aluminum isopropoxide $C_9H_{21}O_3Al$ (>96%) were purchased from Aldrich, UK. The template tetrapropyl ammonium hydroxide solution $[(CH_3CH_2CH_2)_4N(OH)]$ (1.0 M in H_2O) was obtained from Sigma-Aldrich, while ammonium nitrate $[(NH_4)NO_3$, AR grade] for ion exchange was purchased from (Acros organics, Amsterdam, Netherlands Antilles). A commercial zeolite H-ZSM-5 (Si/Al = 40) catalyst material was provided by Zeolyst International. Methanol (99.9%) HPLC grade (Acros organics, Netherlands Antilles).

3.2. Catalyst Preparation

Synthesis of H-ZSM-5 Materials Embedded in Silica Matrix

ZSM-5 zeolites with different Si/Al ratios of 40, 45, and 50 were synthesized. The required amount of aluminum isopropoxide (0.5 g) was added to a 20 wt. % aqueous solution of 11 g tetrapropyl ammonium hydroxide (TPAOH). The mixture was placed in an ice bath under stirring to obtain a clear solution before adding the proper amount (20, 23, 26 ml for Si/Al ratios of 40, 45, and 50, respectively) of tetraethyl orthosilicate (TEOS). This mixture was stirred at room temperature for 24 h to hydrolyze TEOS completely. Thereafter, the solution was heated at 80 °C to remove water and alcohols. Finally, the obtained gel solution with 0.005 Al_2O_3:0.2 SiO_2:0.107 TPAOH:3.25 H_2O, 0.005 Al_2O_3:0.225 SiO_2:0.107 TPAOH:3.25 H_2O and 0.005 Al_2O_3:0.25 SiO_2:0.107 TPAOH:3.25 H_2O for the three synthesized samples of Si/Al ratio of 40, 45, and 50, respectively, was charged into a Teflon-lined stainless-steel autoclave and crystallized by thermal treatment under autogenous pressure

and static conditions at 120 °C for 16 h. After this treatment, the solid product was separated by centrifugation, washed several times with distilled water, dried overnight at 110 °C, and calcined in air at 550 °C for 6 h.

All synthesized ZSM-5 have been transformed into their protonic form, i.e., H-ZSM-5, by ion exchange with NH_4^+ ions and followed by calcination. The samples were heated before ion exchange procedure at 120 °C for 1 h. Then, the dried materials were added to 50 mL of 1.0 M NH_4NO_3 solution under continuous stirring. The samples were treated for 24 h at 60 °C. This step was repeated three times to achieve complete ion exchange. After completion of the ion exchange process, the samples were filtered using a polytetrafluoroethylene (PTFE) filter paper and washed with bi-distilled water. Finally, the obtained samples were calcined again in air at 550 °C for 6 h. The obtained samples were denoted as MFI-40, MFI-45, and MFI-50 with the number referring to the Si/Al ratios of 40, 45, and 50, respectively, of the materials under study. The commercial H-ZSM-5 sample from Zeolyst was also thermally treated at 550 °C for 6 h.

3.3. Characterization of Materials

The elemental composition of the zeolite materials under study was determined by inductively coupled plasma atomic emission spectroscopy (ICP-AES), Optima 7300DV, Perkin-Elmer Corporation, Waltham, MA, USA. Powder XRD studies were performed for all the prepared solid samples using a Bruker diffractometer (Bruker D8 advance target). The XRD patterns were obtained with a Co $K\alpha_{1,2}$ line and a monochromator (λ = 1.79026 Å) at 30 kV and 45 mA. The identification of different crystalline phases in the samples was performed by comparing the data with the Joint Committee for Powder Diffraction Standards (JCPDS) files. The lattice vibrations were measured by FT-IR spectroscopy in mid-range (400–4000 cm^{-1}), all the investigated samples were self-supported and not mixed with KBr. The morphology and particle size of the prepared ZSM-5 were investigated using a JEOL microscope and a model JSM-5600 SEM instrument. The textural properties of the prepared samples were determined from nitrogen adsorption/desorption measurements at −196 °C using ASiQ system (Quantachrome, Pleasanton, CA, USA). The specific surface area, S_{BET}, was calculated by applying the BET equation. The average pore radius was estimated from the relation $2V_{Total}/S_{BET}$, where V_{Total} is the total pore volume (at $P/P_0 = 0.975$). Pore-size distribution was generated by the NLDFT analysis of the adsorption branches, and the values for the average pore size were calculated. ^{27}Al and ^{29}Si MAS NMR spectra of the samples were obtained in single-pulse ("ZG") mode (3.5-ms pulses; 8-s delay between pulses) on a Bruker Avance 400 MHz spectrometer, operating at a frequency of 161.98 MHz. ^{29}Si chemical shifts were referenced to tetramethylsilane and the ^{27}Al chemical shifts were referenced to an aqueous solution of 0.5 M aluminum nitrate. The percentage of $Al^{IV}_{framework}$ and $Al^{VI}_{extra-framework}$ species were estimated from solid-state NMR spectral analysis and also by applying the formula; $(Si/Al)NMR = I/\sum 0.25n\ I_n$, where ($I$) represents the sum of the peak area of the NMR signals assigned to Si(nAl) building unit and (I_n) corresponds to the intensity of the resonance peak correspond to the $(AlO)_n\ Si(OSi)_{4-n}$ sites [63].

The acidic characteristic of the synthesized samples was determined by using NH_3-temperature-programmed desorption (NH_3-TPD) measurements performed on (Micrometric Autochem 2910 apparatus, Norcross, GA, USA). For the NH_3-TPD measurements, 100 mg of sample was crushed and sieved in a size of 212–425 μm. Subsequently, it was placed in a quartz tube reactor and packed with glass wool on both sides. The sample was preheated at 550 °C under helium gas flow (10 mL min^{-1}) for 15 min to remove any physiosorbed gases, and then the sample was saturated with NH_3 gas for 1 h at 100 °C. After that, the sample was flushed with helium gas for 1 h at 100 °C to remove any ammonia. Then, the desorption temperature increased from 100 to 600 °C under helium gas flow with a heating rate of 5 °C min^{-1} and NH_3-TPD patterns were collected by measuring the signal from a thermal conductivity detector (TCD). FT-IR spectra of the calcined catalysts obtained at room temperature using Perkin-Elmer Spectrum 100 FT-IR spectrometer. The CO adsorption FT-IR spectra collected in wavelength range of 4000–1000 cm^{-1} with 4 cm^{-1} resolution. For these experiments,

15–16 mg of catalyst sample was self-supported pressed into a pellet. The pellet was placed in the cryogenic cell (sample chamber), which was closed tightly. Then, the pellet was preheated from ambient temperature to 300 °C with rate of 5 °C min^{-1} and held for 1h under vacuum (6.9×10^{-6} mbar). Afterwards, the cell was cooled down to liquid nitrogen temperature (−196 °C) and first scan was collected before adsorption of CO start. The CO adsorption was carried out at −196 °C, start from 5.5×10^{-2} mbar till the pressure reach 10 mbar.

3.4. Catalytic MTO Reaction

All synthesized mesoporous H-ZSM-5 and the commercial Zeolyst H-ZSM-5 reference samples have been evaluated for the MTO reaction using an operando UV-vis spectroscopy reaction setup with online gas chromatography. Details of this setup can be found in recent literature [57]. Catalytic testing was done in a fixed-bed quartz reactor (4 cm in length, 0.1 mm thickness). The catalyst powder was pressed to give pellets, followed by crushing and sieving. The 212–425 µm fraction was used for catalytic testing. Prior to the reaction, ~50 mg of the catalyst was activated at 550 °C under the flow of 100% oxygen (10 mL h^{-1}) for 1 h and then cooled to the desired reaction temperature (500°C). The WHSV of methanol was kept at 3 h^{-1} by flowing helium gas through a methanol saturator. Analysis of the reactant and reaction products was performed with online gas chromatography (GC) by using an Interscience Compact GC instrument equipped with Rtx-1+Rtx-Wax, Rt-TCEP+Rtx-1 and Al_2O_3/Na_2SO_4 columns respectively and two flame ionization detectors (FIDs). The hydrocarbon pool intermediate species which generally forms during the MTO reaction was determined using an operando UV-vis absorption spectroscopy method. The measurements were performed in the wavelength range of 200–1800 nm using a high-temperature operando UV-vis probe manufactured by Avantes. The probe consists of one excitation and one collection fiber, which are connected to a Deuterium-Halogen light source and an Avaspec 2048 UV-vis spectroscope (Apeldoorn, NS, Netherlands).

4. Conclusions

H-ZSM-5 zeolites (Si/Al ratios of 40, 45, and 50) embedded in amorphous silica were successfully synthesized by a modified hydrothermal synthesis method. A set of characterization techniques were used to determine the structural, textural, and acidic properties of the synthesized materials. The synthesized H-ZSM-5 samples possessed the MFI structure, but exhibited lower Brønsted acid-site density and strength compared to a commercial microporous H-ZSM-5 sample. The variation of the Si/Al ratio affected the morphology, crystal size, and the porosity. The synthesized materials exhibited porosity comprising mesopores, thus showing substantially improved mass transport. The catalytic performance of the materials has been tested in the MTO process at 500 °C to understand the deactivation pattern of ZSM-5 catalysts. Interestingly, the synthesized materials offered high selectivity towards propylene ($C_{3=}$) in comparison with commercial Zeolyst sample under the same reaction conditions. The formation of hydrocarbon species during the MTO reaction has been studied with operando UV-vis spectroscopy in a fixed-bed reactor. The Zeolyst sample yielded phenanthrene/anthracene intermediate species, while the synthesized H-ZSM-5 samples majorly showed the presence of methylated naphthalene carbocations intermediate species. The synthesized H-ZSM-5 samples are favorable for forming active hydrocarbon species along with coke at the beginning of the reaction. The low density of Brønsted acid sites and the mesoporous nature of synthesized H-ZSM-5 catalysts are responsible for higher propylene selectivity.

Supplementary Materials: The following are available online at http://www.mdpi.com/2073-4344/9/4/364/s1, Figure S1: FT-IR spectra for investigated samples. Figure S2: NH_3-TPD patterns of the samples. Figure S3: FT-IR spectra of samples after CO adsorption in the region of 2260-2100 cm^{-1}, the band at 2230 cm^{-1} corresponding to the strong Lewis acid sites. Figure S4: Selectivity patterns for $C_{3=}/C_{2=}$ ratio of synthesized H-ZSM-5 and Zeolyst reference sample for the MTO reaction at a reaction temperature of 500 °C and WHSV of 3 h^{-1}; (a) MFI-40, (b) MFI-45, (c) MFI-50, and (d) Zeolyst reference. Figure S5: Operando UV-vis spectra collected during the MTO

reaction over (a) MFI-40; (b) MFI-45; (c) MFI-50 and (d) Zeolyst; WHSV: 3 h^{-1}, reaction temperature: 500 °C. The green colored spectra corresponds to the initial stage of reaction; where the products formation is initiated, the red colored spectra indicate to the stable/slower deactivation; where the products formation reach to the steady state, and the black colored spectra relates to the deactivated stage; where the products formation decreased drastically. Figure S6: The GC image for running MTO reaction of synthesized H-ZSM-5 (Si/Al = 50) sample. Scheme S1: The dual-cycle mechanistic concepts for conversion of methanol-to-olefins reaction over H-ZSM-5 catalysts. Table S1: Quantification data obtained from FT-IR spectra after CO adsorption (9.9 mbar pressure).

Author Contributions: H.S.K. carried out all the experiments, analyzed the data and the main responsible for writing-original draft of the paper; H.S.K., M.M. and K.N. writing-review and editing; S.N.B., M.M. and K.N. conceived the research project and designed the experiments; S.N.B., M.M. and K.N. supervised and directed the research project.

Funding: This research was funded by the Deanship of Scientific Research (DSR) of King AbdulAziz University, Jeddah, Saudi Arabia (grant number T-002-431) and the King AbdulAziz City for Science and Technology, Riyadh, Saudi Arabia (grant number PGP-36-266).

Acknowledgments: The authors acknowledge the support from Bert M. Weckhuysen, Javier Ruiz-Martinez and Elena Borodina (Utrecht University, The Netherlands) for valuable discussions and allowing us to use their facilities as a part of research collaboration. Florain Meirer and Joris Goetze (Utrecht University, The Netherlands) also acknowledged for assistance in performing the NNMF analysis.

Conflicts of Interest: The authors declare no conflict of interest.

References

1. Mei, C.; Wen, P.; Liu, Z.; Liu, H.; Wang, Y.; Yang, W.; Xie, Z.; Hua, W.; Gao, Z. Selective production of propylene from methanol: Mesoporosity development in high silica HZSM-5. *J. Catal.* **2008**, *258*, 243–249. [CrossRef]
2. Corma, A.; Mengual, J.; Miguel, P. IM-5 zeolite for steam catalytic cracking of naptha to produce propene and ethane. An alternative to ZSM-5 zeolite. *J. Appl. Catal. A Gen.* **2013**, *460–461*, 106–115. [CrossRef]
3. Meng, T.; Mao, D.; Guo, Q.; Lu, G. The effect of crystal sizes of HZSM-5 zeolites in ethanol conversion to propylene. *Catal. Commun.* **2012**, *21*, 52–57. [CrossRef]
4. Yang, G.; Wei, Y.; Xu, S.; Chen, J.; Li, J.; Liu, Z.; Yu, J.; Xu, R. Nanosize-Enhaned Lifetime of SAPO-34 Catalysts in Methanol-to-Olefin Reaction. *J. Phys. Chem. C* **2013**, *117*, 8214–8222. [CrossRef]
5. Jo, C.; Jung, J.; Shin, H.S.; Kim, J.; Ryoo, R. Capping with Multivalent Surfactants for Zeolite Nanocrystal Synthesis. *Angew. Chem. Int. Ed.* **2013**, *52*, 10014–10017. [CrossRef]
6. Tian, P.; Wei, Y.; Ye, M.; Liu, Z. Methanol to Olefins (MTO): From Fundamentals to Commercialization. *ACS Catal.* **2015**, *5*, 1922–1938. [CrossRef]
7. Hong, Y.; Gruver, V.; Fripiat, J.J. Role of Lewis Acidity in the Isomerization of n-Pentane and o-Xylene on Dealuminated H-Mordenites. *J. Catal.* **1994**, *150*, 421–429. [CrossRef]
8. Goetze, J.; Meirer, F.; Yarulina, I.; Gascon, I.; Kapteijn, F.; Ruiz-Martínez, J.; Weckhuysen, B.M. Insights into the Activity and Deactivation of the Methanol-to-Olefins Process over Different Small-Pore Zeolites As Studied with Operando UV–vis Spectroscopy. *ACS Catal.* **2017**, *7*, 4033–4046. [CrossRef]
9. Catizzone, E.; Cirelli, Z.; Aloise, A.; Lanzafame, P.; Migliori, M.; Giordano, G. Methanol conversion over ZSM-12, ZSM-22 and EU-1 zeolites: From DME to hydrocarbons production. *Catal. Today* **2018**, *304*, 39–50. [CrossRef]
10. Palčić, A.; Ordomsky, V.V.; Qin, Z.; Georgieva, V.; Valtchev, V. Tuning Zeolite Properties for a Highly Efficient Synthesis of Propylene from Methanol. *Chem. Eur. J.* **2018**, *24*, 13136–13149. [CrossRef]
11. Losch, P.; Boltz, M.; Bernardon, C.; Louis, B.; Palčić, A.; Valtchev, V. Impact of external surface passivation of nano-ZSM-5 zeolites in the methanol-to-olefins reaction. *Appl. Catal. A Gen.* **2016**, *509*, 30–37. [CrossRef]
12. Ibáñez, M.; Epelde, E.; Aguayo, A.T.; Gayubo, A.G.; Bilbao, J.; Castaño, P. Selective dealumination of HZSM-5 zeolite boosts propylene by modifying 1-butene cracking pathway. *Appl. Catal. A Gen.* **2017**, *543*, 1–9. [CrossRef]
13. Mirodatos, C.; Barthomeuf, D. Superacid sites in zeolites. *J. Chem. Soc. Chem. Commun.* **1981**, 39–40. [CrossRef]
14. Corma, A.; Fornés, V.; Rey, F. Extraction of extra-framework aluminium in ultrastable Y zeolites by $(NH_4)2SiF_6$ treatments: I. Physicochemical Characterization. *Appl. Catal.* **1990**, *59*, 267–274. [CrossRef]

15. Däumer, D.; Räuchle, K.; Reschetilowski, W. Experimental and Computational Investigations of the Deactivation of H-ZSM-5 Zeolite by Coking in the Conversion of Ethanol into Hydrocarbons. *ChemCatChem* **2012**, *4*, 802–814. [CrossRef]
16. Hadi, N.; Niaei, A.; Nabavi, S.R.; Farzi, A.; Shirazia, M.N. Development of a New Kinetic Model for Methanol to Propylene Process on Mn/H-ZSM-5 Catalyst. *Chem. Biochem. Eng. Q.* **2014**, *28*, 53.
17. Bleken, F.L.; Chavan, S.; Olsbye, U.; Boltz, M.; Ocampo, F.; Louis, B. Conversion of methanol into light olefins over ZSM-5 zeolite: Strategy to enhance propene selectivity. *Appl. Catal. A Gen.* **2012**, *447–448*, 178–185. [CrossRef]
18. Xi, D.; Sun, Q.; Xu, J.; Cho, M.; Cho, H.S.; Asahina, S.; Li, Y.; Deng, F.; Terasaki, O.; Yu, J. In situ growth-etching approach to the preparation of hierarchically macroporous zeolites with high MTO catalytic activity and selectivity. *J. Mater. Chem. A* **2014**, *2*, 17994–18004. [CrossRef]
19. Perez-Ramirez, J.; Christensen, C.H.; Egeblad, K.; Christensen, C.H.; Groen, J.C. Hierarchical zeolites: Enhanced utilisation of microporous crystals in catalysis by advances in materials design. *Chem. Soc. Rev.* **2008**, *37*, 2530–2542. [CrossRef]
20. Li, L.; Cui, X.; Li, J.; Wang, J. Synthesis of SAPO-34/ZSM-5 Composite and Its Catalytic Performance in the Conversion of Methanol to Hydrocarbonsc. *J. Braz. Chem. Soc.* **2014**, *26*, 290–296. [CrossRef]
21. Conte, M.; Xu, B.; Davies, T.E.; Bartley, J.K.; Carley, A.F.; Taylor, S.H.; Khalid, K.; Hutchings, G.J. Enhanced selectivity to propene in the methanol to hydrocarbons reaction by use of ZSM-5/11 intergrowth zeolite. *Microporous Mesoporous Mater.* **2012**, *164*, 207–213. [CrossRef]
22. Lonstad Bleken, B.-T.; Mino, L.; Giordanino, F.; Beato, P.; Svelle, S.; Lillerud, K.P.; Bordiga, S. Probing the surface of nanosheet H-ZSM-5 with FTIR spectroscopy. *Phys. Chem. Chem. Phys.* **2013**, *15*, 13363–13370. [CrossRef] [PubMed]
23. Müller, S.; Liu, Y.; Vishnuvarthan, M.; Sun, X.; van Veen, A.C.; Haller, G.L.; Sanchez-Sanchez, M.; Lercher, J.A. Coke formation and deactivation pathways on H-ZSM-5 in the conversion of methanol to olefins. *J. Catal.* **2015**, *325*, 48–59. [CrossRef]
24. Zhang, S.; Gong, Y.; Zhang, L.; Liu, Y.; Dou, T.; Xu, J.; Deng, F. Hydrothermal treatment on ZSM-5 extrudates catalyst for methanol to propylene reaction: Finely tuning the acidic property. *Fuel Process. Technol.* **2015**, *129*, 130–138. [CrossRef]
25. Wu, W.; Guo, W.; Xiao, W.; Luo, M. Dominant reaction pathway for methanol conversion to propene over high silicon H-ZSM-5. *Chem. Eng. Sci.* **2011**, *66*, 4722–4732. [CrossRef]
26. Yarulina, I.; Bailleul, S.; Pustovarenko, A.; Martinez, J.R.; De Wispelaere, K.; Hajek, J.; Weckhuysen, B.M.; Houben, K.; Baldus, M.; Van Speybroeck, V.; et al. Suppression of the Aromatic Cycle in Methanol-to-Olefins Reaction over ZSM-5 by Post-Synthetic Modification Using Calcium. *ChemCatChem* **2016**, *8*, 3057–3063. [CrossRef]
27. Yarulina, I.; De Wispelaere, K.; Bailleul, S.; Goetze, J.; Radersma, M.; Abou-Hamad, E.; Vollmer, I.; Goesten, M.; Mezari, B.; Hensen, E.J.M.; et al. Structure–performance descriptors and the role of Lewis acidity in the methanol-to-propylene process. *Nat. Chem.* **2018**, *10*, 804–812.
28. Jacobs, P.A.; Derouane, E.G.; Weitkamp, J. Evidence for X-ray-amorphous zeolites. *Chem. Commun.* **1981**, 591–593. [CrossRef]
29. Nicolaides, C. A novel family of solid acid catalysts: Substantially amorphous or partially crystalline zeolitic materials. *Appl. Catal. A Gen.* **1999**, *185*, 211–217. [CrossRef]
30. Triantafyllidis, K.S.; Nalbandian, L.; Trikalitis, P.N.; Ladavos, A.K.; Mavromoustakos, T.; Nicolaides, C.P. Structural, compositional and acidic characteristics of nanosized amorphous or partially crystalline ZSM-5 zeolite-based materials. *Microporous Mesoporous Mater.* **2004**, *75*, 89–100. [CrossRef]
31. Corma, A.; Díaz-Cabañas, M.J. Amorphous microporous molecular sieves with different pore dimensions and topologies: Synthesis, characterization and catalytic activity. *Microporous Mesoporous Mater.* **2006**, *89*, 39–46. [CrossRef]
32. Tago, T.; Masuda, Y. Zeolite nanocrystals-synthesis and applications. In *Nanocrystals*; IntechOpen: London, UK, 2010; pp. 8–206.
33. Kim, W.J.; Kim, S.D. Method of Preparing zsm-5 Using Variable Temperature without Organic Template. U.S. Patent 7,361,328, 22 April 2008.
34. Yeong, Y.F.; Abdullah, A.Z.; Ahmad, A.L.; Bhatia, S. Propylsulfonic acid-functionalized partially crystalline silicalite-1 materials: Synthesis and characterization. *J. Porous Mater.* **2011**, *18*, 147–157. [CrossRef]

35. Mostafa, M.M.M.; Rao, K.N.; Harun, H.S.; Basahel, S.N.; El-Maksod, I.H.A. Synthesis and characterization of partially crystalline nanosized ZSM-5 zeolites. *Ceram. Int.* **2013**, *39*, 683–689. [CrossRef]
36. Haw, K.-G.; Gilson, J.-P.; Nesterenko, N.; Akouche, M.; El Siblani, H.; Goupil, J.-M.; Rigaud, B.; Minoux, D.; Dath, J.-P.; Valtchev, V. Supported Embryonic Zeolites and their Use to Process Bulky Molecules. *ACS Catal.* **2018**, *8*, 8199–8212. [CrossRef]
37. Cheng, Y.; Wang, L.-J.; Li, J.-S.; Yang, Y.-C.; Sun, X.-Y. Preparation and characterization of nanosized ZSM-5 zeolites in the absence of organic template. *Mater. Lett.* **2005**, *59*, 3427–3430. [CrossRef]
38. Barbera, K.; Bonino, F.; Bordiga, S.; Janssens, T.V.W.; Beato, P. Structure–deactivation relationship for ZSM-5 catalysts governed by framework defects. *J. Catal.* **2011**, *280*, 196–205. [CrossRef]
39. Bjørgen, M.; Svelle, S.; Joensen, F.; Nerlov, J.; Kolboe, S.; Bonino, F.; Palumbo, L.; Bordiga, S.; Olsbye, U. Conversion of methanol to hydrocarbons over zeolite H-ZSM-5: On the origin of the olefinic species. *J. Catal.* **2007**, *249*, 195–207. [CrossRef]
40. Robson, H.; Lillerud, K.P. *Verified Synthesis of Zeolitic Materials*; Elsevier: Amsterdam, The Netherlands, 2001.
41. Coster, D.; Blumenfeld, A.L.; Fripiat, J.J. Lewis Acid Sites and Surface Aluminum in Aluminas and Zeolites: A High-Resolution NMR Study. *J. Phys. Chem.* **1994**, *98*, 6201–6211. [CrossRef]
42. Corma, A.; Fornés, V.; Martínez, A.; Sanz, J. Tetrahedral and Octahedral Extraframework Aluminum in Ultrastable Y Zeolites. In *Fluid Catalytic Cracking*; American Chemical Society: Washington, DC, USA, 1988; pp. 2–17.
43. Kunkeler, P.J.; Zuurdeeg, B.J.; van der Waal, J.C.; van Bokhoven, J.A.; Koningsberger, D.C.; van Bekkum, H. Zeolite Beta: The Relationship between Calcination Procedure, Aluminum Configuration, and Lewis Acidity. *J. Catal.* **1998**, *180*, 234–244. [CrossRef]
44. Thomas, J.M.; Klinowski, J. The Study of Aluminosilicate and Related Catalysts by High-Resolution Solid-State NMR Spectroscopy. *Adv. Catal.* **1985**, *33*, 199–374.
45. Fyfe, C.A.; Gobbi, G.C.; Kennedy, G.J.; Graham, J.D.; Ozubko, R.S.; Murphy, W.J.; Bothner-By, A.; Dadok, J.; Chesnick, A.S. Detailed interpretation of the 29Si and 27Al high-field MAS n.m.r. spectra of zeolites offretite and omega. *Zeolites* **1985**, *5*, 179–183. [CrossRef]
46. Zhu, L.; Yin, S.; Wang, X.; Liu, Y.; Wang, S. The catalytic properties evolution of HZSM-5 in the conversion of methanol to gasoline. *RSC Adv.* **2016**, *6*, 82515–82522. [CrossRef]
47. Jacobsen, C.J.H.; Madsen, C.; Janssens, T.V.W.; Jakobsen, H.J.; Skibsted, J. Zeolites by confined space synthesis—Characterization of the acid sites in nanosized ZSM-5 by ammonia desorption and ^{27}Al/29Si-MAS NMR spectroscopy. *Microporous Mesoporous Mater.* **2000**, *39*, 393–401. [CrossRef]
48. Costa, C.; Dzikh, I.P.; Lopes, J.M.; Lemos, F.; Ribeiro, F.R. Activity–acidity relationship in zeolite ZSM-5. Application of Brönsted-type equations. *J. Mol. Catal. A Chem.* **2000**, *154*, 193–201. [CrossRef]
49. Kondo, J.N.; Nishitani, R.; Yoda, E.; Yokoi, T.; Tatsumi, T.; Domen, K. A comparative IR characterization of acidic sites on HY zeolite by pyridine and CO probes with silica-alumina and [gamma]-alumina references. *Phys. Chem. Chem. Phys.* **2010**, *12*, 11576–11586. [CrossRef] [PubMed]
50. Leydier, F.; Chizallet, C.; Costa, D.; Raybaud, P. CO adsorption on amorphous silica-alumina: Electrostatic or Bronsted acidity probe? *Chem. Commun.* **2012**, *48*, 4076–4078. [CrossRef] [PubMed]
51. Hattori, H.; Ono, Y. *Solid Acid Catalysis: From Fundamentals to Applications*; Tylor & Francis Group: Boca Raton, FL, USA, 2015.
52. Tanabe, K.; Misono, M.; Ono, Y.; Hattori, H. *New Solid Acids and Bases: Their Catalytic Properties (Studies in Surface Science and Catalysis)*; Elsevier Science Ltd.: Amsterdam, The Netherlands, 1989.
53. Moreno-Piraján, J.C.; Garcia-Cuello, V.S.; Giraldo, L. Synthesis of HMOR and HZSM-5 and their Behaviour in the Catalytic Conversion of Methanol to Propylene (MTP). *J. Thermodyn. Catal.* **2010**, *1*, 101. [CrossRef]
54. Lin, L.; Qiu, C.; Zhuo, Z.; Zhang, D.; Zhao, S.; Wu, H.; Liu, Y.; He, M. Acid strength controlled reaction pathways for the catalytic cracking of 1-butene to propene over ZSM-5. *J. Catal.* **2014**, *309*, 136–145. [CrossRef]
55. Castaño, P.; Gayubo, A.G.; Pawelec, B.; Fierro, J.L.G.; Arandes, J.M. Kinetic modelling of methylcyclohexane ring-opening over a HZSM-5 zeolite catalyst. *Chem. Eng. J.* **2008**, *140*, 287–295. [CrossRef]
56. Qian, Q.; Vogt, C.; Mokhtar, M.; Asiri, A.M.; Al-Thabaiti, S.A.; Basahel, S.N.; Ruiz-Martínez, J.; Weckhuysen, B.M. Combined Operando UV/Vis/IR Spectroscopy Reveals the Role of Methoxy and Aromatic Species during the Methanol-to-Olefins Reaction over H-SAPO-34. *ChemCatChem* **2014**, *6*, 3396–3408. [CrossRef]

57. Borodina, E.; Meirer, F.; Lezcano-González, I.; Mokhtar, M.; Asiri, A.M.; Al-Thabaiti, S.A.; Basahel, S.N.; Ruiz-Martinez, J.; Weckhuysen, B.M. Influence of the reaction temperature on the nature of the active and deactivating species during methanol to olefins conversion over H-SSZ-13. *ACS Catal.* **2015**, *5*, 992–1003. [CrossRef]
58. Borodina, E.; Kamaluddin, H.S.H.; Meirer, F.; Mokhtar, M.; Asiri, A.M.; Al-Thabaiti, S.A.; Basahel, S.N.; Ruiz-Martinez, J.; Weckhuysen, B.M. Influence of the Reaction Temperature on the Nature of the Active and Deactivating Species During Methanol-to-Olefins Conversion over H-SAPO-34. *ACS Catal.* **2017**, *7*, 5268–5281. [CrossRef]
59. Sun, X.; Mueller, S.; Shi, H.; Haller, G.L.; Sanchez-Sanchez, M.; van Veen, A.C.; Lercher, J.A. On the impact of co-feeding aromatics and olefins for the methanol-to-olefins reaction on HZSM-5. *J. Catal.* **2014**, *314*, 21–31. [CrossRef]
60. Bjørgen, M.; Joensen, F.; Lillerud, K.-P.; Olsbye, U.; Svelle, S. The mechanisms of ethene and propene formation from methanol over high silica H-ZSM-5 and H-beta. *Catal. Today* **2009**, *142*, 90–97. [CrossRef]
61. Campbell, S.M.; Jiang, X.-Z.; Howe, R.F. Methanol to hydrocarbons: Spectroscopic studies and the significance of extra-framework aluminium. *Microporous Mesoporous Mater.* **1999**, *29*, 91–108. [CrossRef]
62. Westgård Erichsen, M.; De Wispelaere, K.; Hemelsoet, K.; Moors, S.L.C.; Deconinck, T.; Waroquier, M.; Svelle, S.; Van Speybroeck, V.; Olsbye, U. How zeolitic acid strength and composition alter the reactivity of alkenes and aromatics towards methanol. *J. Catal.* **2015**, *328*, 186–196. [CrossRef]
63. Song, C.; Wang, M.; Zhao, L.; Xue, N.; Peng, L.; Guo, X.; Ding, W.; Yang, W.; Xie, Z. Synergism between the Lewis and Brönsted acid sites on HZSM-5 zeolites in the conversion of methylcyclohexane. *Chin. J. Catal.* **2013**, *34*, 2153–2159. [CrossRef]

catalysts

MDPI

Article

Direct Synthesis of Ti-Containing CFI-Type Extra-Large-Pore Zeolites in the Presence of Fluorides

Yichen Wang [1], Hongjuan Wang [1], Yuanchao Shao [1], Tianduo Li [1,*], Takashi Tatsumi [2] and Jin-Gui Wang [1,*]

[1] Shandong Provincial Key Laboratory of Molecular Engineering, School of Chemistry and Pharmaceutical Engineering, Qilu University of Technology (Shandong Academy of Sciences), Jinan 250353, China; wangyc610@163.com (Y.W.); hongjuanwang2015@163.com (H.W.); sychao629@163.com (Y.S.)

[2] Institute of Innovative Research, Tokyo Institute of Technology, 4259 Nagatsuta, Midori-ku, Yokohama 226-8503, Japan; tacchan.tatsumi@gmail.com

* Correspondence: ylpt6296@vip.163.com (T.L.); JGWang@qlu.edu.cn (J.-G.W.); Tel.: +86-531-89631208 (T.L.); +86-531-89631212 (J.-G.W.)

Received: 18 February 2019; Accepted: 12 March 2019; Published: 14 March 2019

Abstract: Ti-containing zeolites showed extremely high activity and selectivity in numerous friendly environmental oxidation reactions with hydrogen peroxide as a green oxidant. It will be in high demand to synthesize Ti-containing crystalline extra-large-pore zeolites due to the severe restrictions of medium-pore and/or large-pore zeolites for bulky reactant oxidations. However, the direct synthesis of extra-large-pore Ti-zeolites was still challengeable. Here, we firstly report a strategy to directly synthesize high-performance Ti-containing CFI-type extra-large-pore (Ti-CFI) zeolites assisted with fluorides. The well-crystallized Ti-CFI zeolites with framework titanium species could be synthesized in the hydrofluoric acid system with seed or in the ammonium fluoride system without seed, which showed higher catalytic activity for cyclohexene oxidation than that synthesized from the traditional LiOH system.

Keywords: Ti-CFI; Ti-CIT-5; extra-large-pore; zeolites; fluorides; titanosilicates; oxidation

1. Introduction

Zeolite, a type of crystalline microporous aluminosilicate, has wide applications in adsorption, separation, and catalysis, especially in oil refining and producing petrochemicals as solid-acid catalysts [1–6]. Incorporation of isolated titanium ions into a high-silica zeolite to achieve a Ti-containing zeolite, called titanosilicate, was a milestone in zeolites and heterocatalysis due to its extremely high activity and selectivity in numerous friendly environmental oxidation reactions with hydrogen peroxide as a green oxidant [7]. The discovered MFI-type and MWW-type zeolites were successfully applied in the industrial processes of the hydroxylation of phenol, the ammoximation of cyclohexanone/butanone, and the liquid-phase epoxidation of propylene to propylene oxide [8–11].

Subsequently, a series of Ti-containing zeolites with different topologies were synthesized including 10-ring medium-micropore (~0.55 nm in diameter) [12–14] and 12-ring large-micropore (~0.75 nm in diameter) zeolites [15–21]. However, considering the severe restrictions for the oxidation of bulky reactants in these 10-ring and 12-ring micropores, it would be in high demand to synthesize Ti-containing three-dimensionally crystalline extra-large-pore (larger than 12 rings) zeolites.

It was very difficult to directly crystallize the starting gel (containing silicon source, titanium source, and structure-directing agents) to form Ti-containing extra-large-pore zeolites because the titanium ion proved no structure-directing ability and its ionic radius was larger than that of the silicon ion, which led to difficulties in the crystallization of raw materials and the incorporation of titanium into the zeolite framework [22,23]. Until now, only a few Ti-containing extra-large-pore

zeolites were directly synthesized, including aluminophosphate (Ti-VPI-5) with an 18-ring [24], Ti-UTL with a 14-ring extra-large pore [25], Ti-UTD-1 (DON-type) with a 14-ring extra-large pore [26], and Ti-CIT-5 with a 14-ring extra-large pore [27]. So as to crystallize the raw materials, special and expensive structure-directing agents, i.e., bis(pentamethyl-cylcopentadienyl)cobalt(III) hydroxide for Ti-UTD-1 and lithium hydroxide as an accelerator for Ti-CIT-5 were required. However, the accelerator of lithium hydroxide for the crystallization of Ti-CIT-5 resulted in large amounts of extra-framework titanium species. For activating this extra-large-pore catalyst, further post-treatment processes were required. Therefore, effective strategies to prepare Ti-containing extra-large-pore zeolites were still desirable and significant.

Here, we firstly report a strategy to directly synthesize the high-performance Ti-containing CFI-type extra-large-pore (Ti-CFI) zeolites in the presence of fluorides. The influence factors such as the type of fluoride source, water content, and the additive of seed for the crystallization of Ti-CFI were investigated. The well-crystallized Ti-CFI zeolites with framework titanium species could be synthesized in the HF system with seed or in the NH_4F system without seed, which both showed higher catalytic activity for cyclohexene oxidation than that synthesized from the LiOH system.

2. Results and Discussion

2.1. Zeolite Characterization

Powder X-ray diffraction (PXRD) patterns (Figure 1) showed that Ti-containing CFI-type extra-large-pore zeolites could crystallize in the presence of fluorides. The crystallinity was very low after a 13-day crystallization if hydrofluoric acid was used as the fluoride source (Figure 1a), suggesting some amorphous materials present in the sample. When the concentration of the raw materials increased by decreasing the water content in the raw materials, the crystallinity was slightly increased as indicated by the increased diffraction intensity in Figure 1b. However, crystallinity was still very slow. The broad peak around 20–25° implied the presence of amorphous raw materials in this sample. This indicated that well-crystallized Ti-CFI was difficult to achieve when hydrofluoric acid was used as a fluoride source, although pure silica CFI-type zeolite could be fully crystallized in the HF system (Figure S1, Supplementary Materials). This was also evidence that the synthesis of titanium-containing zeolite was more difficult than synthesis of Ti-free pure silica zeolite. If ammonium fluoride was employed as a fluoride source, as shown in Figure 1c, a sample with good crystallinity could be achieved after a 13-day crystallization. Moreover, all the peaks were consistent with the reported CFI-type topology [27], indicating as-synthesized zeolite without other impure phases. The addition of pure silica CFI-type seeds could accelerate the crystallization process, leading to the formation of a well-crystallized sample even within seven days, as indicated in Figure 1d.

SEM images indicated the presence of amorphous raw materials among the rod-like large crystals of Ti-CIT-5[HF]-13d synthesized in the HF system without seeds, which was consistent with the low diffraction intensity as shown in the PXRD pattern. Samples of Ti-CFI[NH_4F]-13d from the ammonium fluoride system possessed a rod-like crystalline shape with tens of micrometers in length as indicated in Figure 2b. Moreover, the crystal was large and was composed of the small rods. Interestingly, plate-like crystals with 5–10 μm in length, 1–2 μm in width, and 0.2–0.4 μm in thickness could be formed if the seeds were added. No amorphous raw materials or other impure particles were found in the sample of Ti-CFI[HF]-seed-13d. Moreover, the crystal size was smaller than the samples synthesized with only HF and NH_4F, suggesting the role of the seed in accelerating the crystallization rate and decreasing the crystal size.

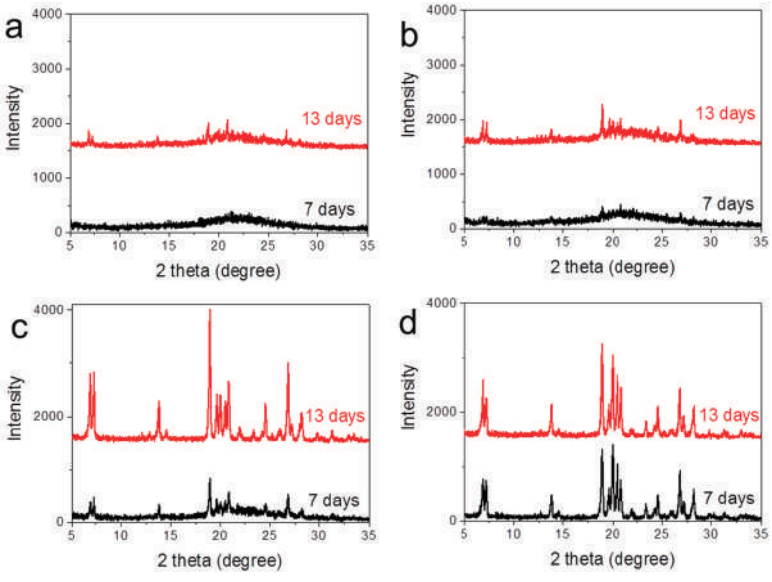

Figure 1. Powder X-ray diffraction (PXRD) patterns of extra-large-pore Ti-CFI zeolites synthesized under different conditions with different crystallization time. (**a**) Ti-CFI[HF] synthesized using hydrofluoric acid as a fluoride source; (**b**) Ti-CFI[HF]-L synthesized by decreasing the water content from 20 to 5 in the H_2O/SiO_2 molar ratio in the HF system; (**c**) Ti-CFI[NH_4F] using ammonium fluoride as a fluoride source; (**d**) Ti-CFI[HF]-seed by adding pure silica CFI-type zeolite as seeds in the HF system.

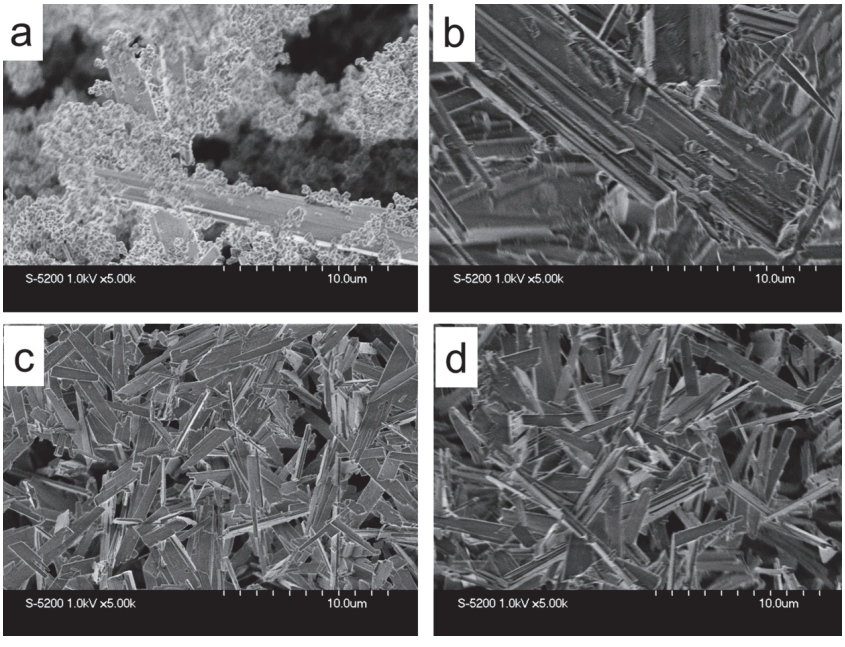

Figure 2. SEM images of (**a**) Ti-CIT-5[HF]-13d, (**b**) Ti-CFI[NH_4F]-13d, (**c**) Ti-CFI[HF]-seed-7d, and (**d**) Ti-CFI[HF]-seed-13d.

Nitrogen adsorption characterization showed that all the samples synthesized in the presence of fluorides had ~400 $m^2 \cdot g^{-1}$ specific surface area. Comparing Ti-CFI[HF]-seed-13d and Ti-CFI[NH_4F]-13d, samples of seed-assisted synthesis in the HF system showed higher specific surface area, micropore volume, and external surface area than those of samples from the NH_4F synthetic system. The higher external surface area implied a small crystal size, which was consistent with the abovementioned SEM characterization. Comparing Ti-CFI[HF]-seed-7d and Ti-CFI[HF]-seed-13d, the long-time crystallization led to a slight increase in specific surface area and micropore volume. Meanwhile, the Ti content was effectively increased after long-time crystallization. Unlike the fluoride system, Ti-CFI[LiOH], which was directly synthesized from the LiOH system without further post-treatment, showed extremely low Brunauer–Emmett–Teller (BET) specific surface area and micropore volume. Post-treatment by washing with acid significantly increased the BET specific surface area and micropore volume of Ti-CFI[LiOH]-post, but decreased the Ti content. In addition, Ti-CFI synthesized in the presence of fluorides always showed a higher pore volume and lower external specific surface area than those of samples synthesized in the presence of LiOH. The larger amounts of external specific surface suggested a smaller crystal size of samples synthesized in the presence of LiOH (Figure S2, Supplementary Materials).

Titanium was the catalytic center in the Ti-containing zeolite for the epoxidation of olefins, which is of great important processes for producing fine chemicals. The state of Ti would greatly affect the catalytic performance. There are several types of Ti species in the presence of the zeolite, including tetrahedral coordinated and octahedral coordinated titanium species, and anatase-like TiO_2 tiny particles. Furthermore, it was proven that only tetrahedral (framework) Ti showed catalytic performance for the selective oxidation of olefins. The presence of octahedral (extra-framework) Ti and tiny TiO_2 particles would adversely affect the catalytic activity and decrease the utilization efficiency of hydrogen peroxide. Diffuse reflectance ultraviolet/visible light (UV/Vis) (DRUV/Vis) spectroscopy is an effective technique to detect the coordination states of Ti species. The absorbance peak at about 210 nm attributed to $Ti^{4+}O^{2-} \rightarrow Ti^{3+}O^{-}$ ligand-to-metal charge transfer was assigned to the framework Ti species. The broad absorbance peak at about 250 nm was assigned to the extra-framework Ti species. The peak at about 330 nm was assigned to the formation of tiny anatase-like TiO_2 particles [7]. As indicated in the Figure 3A, all the samples synthesized in the fluoride system showed the main band at about 210 nm, indicating that most of the titanium was present as framework Ti species. The presence of a shoulder peak at 250 nm indicated the presence of small amounts of extra-framework Ti species in these samples. In addition, Ti-CFI[NH_4F]-13d showed small amounts of anatase-like TiO_2 as indicated by the presence of a 330-nm band. Prolonging the crystallization period from seven to 13 days, the intensity of the 210-nm band related to the framework Ti increased greatly as compared Ti-CFI[HF]-seed-7d and Ti-CFI[HF]-seed-13d, which was consistent with the results of the ICP test (Table 1). As indicated in the Figure 3B, the sample Ti-CFI[LiOH] synthesized in the LiOH system without post-treatment processes showed the main absorbance band at about 250 nm, indexed as extra-framework Ti species. After post-treatment with acid, the sample Ti-CFI[LiOH]-post only displayed absorbance at about 210 nm, indexed as framework Ti species; however, the intensity decreased greatly.

Table 1. Product yields, chemical compositions, and porosity properties of Ti-CFI zeolites from the different synthetic systems.

Samples	Yields (%)	Si/Ti (mol/mol)	S_{BET} [1] ($m^2 \cdot g^{-1}$)	Pore Volume ($m^3 \cdot g^{-1}$)	$S_{ext.}$ [2] ($m^2 \cdot g^{-1}$)
Ti-CFI[HF]-seed-7d	~90	247	395	0.14	33
Ti-CFI[HF]-seed-13d	~90	189	413	0.15	36
Ti-CFI[NH_4F]-13d	~92	220	385	0.14	22
Ti-CFI[LiOH]	~85	46	280	0.08	84
Ti-CFI[LiOH]-post	-	183	393	0.11	101

[1] Brunauer–Emmett–Teller (BET) specific surface area. [2] External specific surface areas were calculated from the t-plot curve.

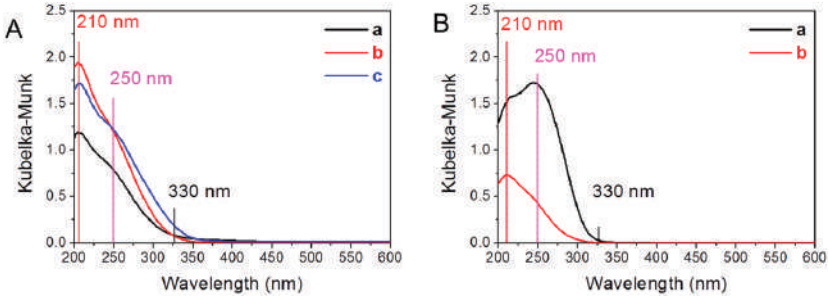

Figure 3. Diffuse reflectance ultraviolet/visible light (DRUV/Vis) spectra of Ti-CFI extra-large-pore zeolites synthesized in fluoride system (**A**): (**a**) Ti-CFI[HF]-seed-7d, (**b**) Ti-CFI[HF]-seed-13d, and (**c**) Ti-CFI[NH_4F]-13d, and synthesized in LiOH system (**B**): (**a**) Ti-CFI[LiOH] and (**b**) Ti-CFI[LiOH]-post.

2.2. Catalytic Tests

The characterization showed that well-crystallized Ti-CFI zeolites with framework titanium species could be synthesized in the HF system with seed or in the NH_4F system without seed. Here, catalytic oxidation of cyclohexene using H_2O_2 as an oxidant was employed to test their catalytic performance, while the samples synthesized in the LiOH system were used as controls. Table 2 shows the results of epoxidation of cyclohexene. The reaction routes are shown in Scheme 1. The cyclohexene oxide (I), generated by the heterolytic epoxidation of the cyclohexene C=C double bond, and the 1,2-cyclohexanediol (II) side product, formed by hydrolysis of epoxide ring, generally reflect a concerted process. In contrast, the allylic oxidation side products, 2-cyclohexen-1-ol (III) and 2-cyclohexen-1-one (IV), are often ascribed to a homolytic radical pathway [28]. Others including V, VI, VII, and VIII are the products of further oxidation.

Table 2. Catalytic oxidation of cyclohexene over various Ti-CFI zeolites using H_2O_2 aqueous solution as an oxidant.

Samples	Si/Ti (mol/mol)	Conversion (%)	Selectivity (%)					TON (mol/mol-Ti)	H_2O_2 Efficiency [1] (%)
			I	II	III	IV	Others		
Ti-CFI[HF]-seed-7d	247	8.2	17.0	68.9	4.2	6.1	3.8	49	>99
Ti-CFI[HF]-seed-13d	189	9.0	14.7	69.9	4.6	4.5	11.9	41	>99
Ti-CFI[NH_4F]-13d	220	5.3	8.7	74.8	4.3	6.9	5.3	28	>99
Ti-CFI[LiOH]	46	2.0	73.9	14.9	4.2	4.3	2.7	2	12
Ti-CFI[LiOH]-post	183	4.8	14.1	62.3	11.9	4.5	7.2	21	34

[1] H_2O_2 utilization efficiency % = (I + II + III + IV × 2 + (others) × 2) / converted H_2O_2 × 100.

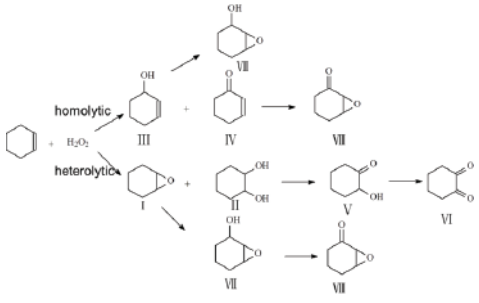

Scheme 1. The possible reaction routes for oxidation of cyclohexene with H_2O_2 as an oxidant.

Table 2 shows the results of catalytic oxidation of cyclohexene over Ti-CFI zeolites using H_2O_2 aqueous solution as an oxidant. Ti-CFI[LiOH] from the LiOH system showed extremely low

catalytic activity, as indicated by the low cyclohexene conversion and low turnover numbers (TON). The catalytic activity was increased after post-treatment to remove extra-framework Ti species. Significantly, all the Ti-CFI synthesized with fluorides showed high cyclohexene conversion, TON and higher H_2O_2 utilization efficiency than those of samples synthesized with LiOH. Moreover, comparing Ti-CFI[NH_4F]-13d with Ti-CFI[LiOH]-post, they had similar cyclohexene conversions; however, sample Ti-CFI[NH_4F]-13d from the fluoride system generated more heterolytic products of I and II. Comparing samples of Ti-CFI[HF]-seed-13d and Ti-CFI[NH_4F]-13d, sample Ti-CFI[HF]-seed-13d showed higher catalytic performance than that of Ti-CFI[NH_4F]-13d. The higher catalytic performance was attributed to higher Ti content, small crystal size, and higher micropore volume, which was consistent with the above results from DRUV/Vis spectra, nitrogen adsorption analysis, and SEM characterizations.

3. Materials and Methods

3.1. Synthesis of Titanium-Containing CFI-Type Extra-Large-Pore Zeolites in the Fluoride System

The Ti-CFI zeolites were synthesized under hydrothermal conditions in a rotating Teflon-lined autoclave (50 revolutions per minute) at 448 K for 7–13 days from the following composition: 1 SiO_2/0.01 TiO_2/0.5 N(16)-methylsparteinium hydroxide/0.5 HF (NH_4F)/5–15 H_2O/0.1 H_2O_2. In a typical run, titanium tetra-*n*-butoxide was added to an H_2O_2 aqueous solution to form a stable Ti source of Ti-peroxo complexes, which were added into an aqueous solution of N(16)-methylsparteinium hydroxide. Then, tetraethylorthosilicate was added into the above mixture under stirring. After stirring for 30 minutes, the resultant solution was heated to 353 K to evaporate the alcohol generated during the hydrolysis of the Ti and Si precursors. After completely evaporating the alcohol, the mixture was cooled down, and HF or NH_4F was carefully dropped. Then, 5 wt.% seeds of pure silica CFI zeolite synthesized as reported [29] in the presence of fluoride were added if required. The final mixture was transferred into an autoclave and treated at 448 K under rotation. The solid product was centrifuged, washed with distilled water, and dried at 373 K, before being calcined at 823 K for 6 h to remove the organic templates. The obtained Ti-CFI zeolites using HF and NH_4F as fluoride sources were denoted as Ti-CFI[HF]-*x*d and Ti-CFI[NH_4F]-*x*d, respectively, where *x* represents the time of hydrothermal synthesis. The obtained Ti-CFI zeolites upon adding seeds were denoted as Ti-CFI[HF]-seed.

3.2. Synthesis of Titanium-Containing CFI-Type Extra-Large-Pore Zeolites in the LiOH System

In a typical run, titanium tetra-*n*-butoxide was added to an H_2O_2 aqueous solution to form a stable Ti source of Ti-peroxo complexes, which were added into an aqueous solution of N(16)-methylsparteinium hydroxide. Then tetraethylorthosilicate was added into above mixture under stirring. After stirring for 30 minutes, the resultant solution was heated to 353 K to evaporate the alcohol generated during the hydrolysis of the Ti and Si precursors. After completely evaporating the alcohol, the clear solution was cooled down, and LiOH was added. The final mixture with the composition of 0.05 Li_2O/1 SiO_2/0.02 TiO_2/0.3 N(16)-methylsparteinium hydroxide/40 H_2O/0.1 H_2O_2 was transferred into an autoclave and treated at 423 K under rotation for 10 days. The solid product was centrifuged, washed with distilled water, dried at 373 K, and calcined at 823 K for 6 h to remove the organic templates. The obtained sample was denoted as Ti-CFI[LiOH]. If the sample was further treated by washing with 1.0 M HCl at room temperature for 24 hours to remove the extra-framework Ti species, the obtained Ti-CFI zeolites were denoted as Ti-CFI[LiOH]-post.

3.3. Catalytic Reaction

Epoxidation reactions were performed in a 10-mL glass reactor immersed in a 60 °C oil bath, using H_2O_2 (35 wt.% in water) as an oxidant. In a typical run, the reactions were carried out with 25 mg of catalyst, 1.0 mmol of cyclohexene, and 1.0 mmol of H_2O_2 in 2.0 mL of acetonitrile with vigorous stirring for 4 h. Reaction mixtures were analyzed by gas chromatography (GC) using a Shimadzu GC-2014 (Kyoto, Japan) equipped with a 60-m TC-1 capillary column and a flame ionization

detector (FID). The amount of the unconverted H_2O_2 was determined by titrating with 0.1 M $Ce(SO_4)_2$ aqueous solution. The products were verified using authentic chemicals commercially available.

3.4. Characterization

Powder X-ray diffraction (PXRD) patterns were measured by a Rigaku Ultima III instrument (Beijing, China) equipped with a Cu-Kα X-ray source (40 kV and 20 mA). Nitrogen adsorption–desorption measurements were measured at 77 K on a BELSORP-Mini II, (MicrotracBEL Corp., Osaka, Japan). Microporous volume and external surface area were calculated from *t*-plot curves. Field-emission scanning electron microscope (SEM) images were obtained on a Hitachi S-5200 microscope (Tokyo, Japan) operated at 1 kV and 10 μA. The content of Si and Ti was tested on a Shimadzu ICPE-9000 (Kyoto, Japan) inductively coupled plasma-atomic emission spectrometer (ICP). Diffuse reflectance UV/Vis spectra (DRUV/Vis) were recorded on a V-650DS spectrophotometer (JASCO, Tokyo, Japan). The diffuse reflectance spectra were converted into the absorption spectra using the Kubelka–Munk function.

4. Conclusions

Ti-containing CFI-type extra-large-pore zeolites were directly synthesized in a fluoride system. The addition of a seed could accelerate the crystallization process and decrease the crystal size. Prolonging the crystallization process could increase the Ti content and pore volume, which was beneficial to the catalytic performance. Compared with the Ti-CFI sample synthesized in the LiOH system, Ti-CFI synthesized in the presence of fluorides showed higher catalytic performance and higher H_2O_2 utilization efficiency. This indicated that the fluoride synthetic system was a good synthetic system for the synthesis of Ti-containing CFI-type extra-large-pore zeolites, which could be extended to the synthesis of other types of Ti-containing zeolites.

Supplementary Materials: The following are available online at http://www.mdpi.com/2073-4344/9/3/257/s1: Figure S1: (A) PXRD and (B) SEM image of the pure silica CFI-type zeolite synthesized in the HF system, which was used as a seed for the preparation of Ti-CFI; Figure S2: SEM image of as-synthesized Ti-CFI[LiOH].

Author Contributions: Conceptualization, J.-G.W. and T.L.; material preparation, Y.W. and Y.S.; synthesis and data analysis, Y.W., H.W., and J.-G.W.; writing—original draft, Y.W. and J.-G.W.; writing—review and editing, Y.W., H.W., Y.S., T.L., T.T., and J.-G.W.; funding acquisition, T.L., and J.-G.W. All authors gave approval for the final version of the manuscript.

Funding: This research was funded by the National Natural Science Foundation of China, grant numbers 51602164 and 21776143, the Program for Scientific Research Innovation Team in Colleges and Universities of Shandong Province, and the Japan Society for the Promotion of Science (JSPS) fellowship.

Conflicts of Interest: The authors declare no conflicts of interest.

References

1. Martinez, C.; Corma, A. Inorganic molecular sieves: Preparation, modification and industrial application in catalytic processes. *Coord. Chem. Rev.* **2011**, *255*, 1558–1580. [CrossRef]
2. Choi, M.; Na, K.; Kim, J.; Sakamoto, Y.; Terasaki, O.; Ryoo, R. Stable single-unit-cell nanosheets of zeolite MFI as active and long-lived catalysts. *Nature* **2009**, *461*, 246–249. [CrossRef] [PubMed]
3. Zhang, X.; Liu, D.; Xu, D.; Asahina, S.; Cychosz, K.A.; Agrawal, K.V.; Al Wahedi, Y.; Bhan, A.; Al Hashimi, S.; Terasaki, O.; et al. Synthesis of self-pillared zeolite nanosheets by repetitive branching. *Science* **2012**, *336*, 41. [CrossRef]
4. Ding, K.; Corma, A.; Macia-Agullo, J.A.; Hu, J.G.; Kramer, S.; Stair, P.C.; Stucky, G.D. Constructing Hierarchical Porous Zeolites via Kinetic Regulation. *J. Am. Chem. Soc.* **2015**, *137*, 11238–11241. [CrossRef]
5. Feng, G.; Cheng, P.; Yan, W.; Boronat, M.; Li, X.; Su, J.H.; Wang, J.; Li, Y.; Corma, A.; Xu, R.; et al. Accelerated crystallization of zeolites via hydroxyl free radicals. *Science* **2016**, *351*, 1188–1191. [CrossRef] [PubMed]
6. Prech, J.; Pizarro, P.; Serrano, D.P.; Cejka, J. From 3D to 2D zeolite catalytic materials. *Chem. Soc. Rev.* **2018**, *47*, 8263–8306. [CrossRef] [PubMed]

7. Taramasso, M.; Perego, G.; Notari, B. Preparation of porous crystalline synthetic material comprised of silicon and titanium oxides. U.S. Patent 4,410,501, 18 October 1983.
8. Lin, M.; Xia, C.; Zhu, B.; Li, H.; Shu, X. Green and efficient epoxidation of propylene with hydrogen peroxide (HPPO process) catalyzed by hollow TS-1 zeolite: A 1.0 kt/a pilot-scale study. *Chem. Eng. J.* **2016**, *295*, 370–375. [CrossRef]
9. Wang, J.G.; Wang, Y.B.; Tatsumi, T.; Zhao, Y.L. Anionic polymer as a quasi-neutral medium for low-cost synthesis of titanosilicate molecular sieves in the presence of high-concentration alkali metal ions. *J. Catal.* **2016**, *338*, 321–328. [CrossRef]
10. Zhao, H.; Yokoi, T.; Kondo, J.N.; Tatsumi, T. Hydrophobicity enhancement of Ti-MWW catalyst and its improvement in oxidation activity. *Appl. Catal. A-Gen.* **2015**, *503*, 156–164. [CrossRef]
11. Zhao, S.; Xie, W.; Liu, Y.; Wu, P. Methyl Ethyl Ketone Ammoximation over Ti-MWW in a Continuous Slurry Reactor. *Chinese J. Catal.* **2011**, *32*, 179–183. [CrossRef]
12. Reddy, J.S.; Kumar, R.; Ratnasamy, P. ChemInform Abstract: Titanium Silicalite-2: Synthesis, Characterization, and Catalytic Properties. *Appl. Catal.* **1990**, *58*, L1–L4. [CrossRef]
13. Serrano, D.P.; Li, H.X.; Davis, M.E. Synthesis of titanium-containing ZSM-48. *J. Chem. Soc. Chem. Commun.* **1992**, *10*, 745–747. [CrossRef]
14. Wu, P.; Tatsumi, T.; Komatsu, T.; Yashima, T. A novel titanosilicate with MWW structure. I. Hydrothermal synthesis, elimination of extraframework titanium, and characterizations. *J. Phys. Chem. B* **2001**, *105*, 2897–2905. [CrossRef]
15. Camblor, M.A.; Corma, A.; Martínez, A.; Pérez-Pariente, J. Synthesis of a titaniumsilicoaluminate isomorphous to zeolite beta and its application as a catalyst for the selective oxidation of large organic molecules. *J. Chem. Soc. Chem. Commun.* **1992**, 589–590. [CrossRef]
16. Blasco, T.; Camblor, M.; Corma, A.; Esteve, P.; Guil, J.; Martinez, A.; Perdigon-Melon, J.; Valencia, S. Direct synthesis and characterization of hydrophobic Aluminum-free Ti−beta zeolite. *J. Phys. Chem. B* **1998**, *102*, 75–88. [CrossRef]
17. Van der Waal, J.; Kooyman, P.; Jansen, J.; Van Bekkum, H. Synthesis and characterization of aluminum-free zeolite titanium beta using di (cyclohexylmethyl) dimethylammonium as a new and selective template. *Micropor. Mesopor. Mater.* **1998**, *25*, 43–57. [CrossRef]
18. Tuel, A. Synthesis, characterization, and catalytic properties of the new TiZSM-12 zeolite. *Zeolites* **1995**, *15*, 236–242. [CrossRef]
19. Wu, P.; Komatsu, T.; Yashima, T. Characterization of titanium species incorporated into dealuminated mordenites by means of IR spectroscopy and 18O-exchange technique. *J. Phys. Chem.* **1996**, *100*, 10316–10322. [CrossRef]
20. Díaz-Cabañas, M.-J.; Villaescusa, L.A.; Camblor, M.A. Synthesis and catalytic activity of Ti-ITQ-7: a new oxidation catalyst with a three-dimensional system of large pore channels. *Chem. Commun.* **2000**, 761–762. [CrossRef]
21. Fan, W.; Wu, P.; Namba, S.; Tatsumi, T. A titanosilicate that is structurally analogous to an MWW-type lamellar precursor. *Angew. Chem. Int. Ed.* **2004**, *43*, 236–240. [CrossRef]
22. Tamura, M.; Chaikittisilp, W.; Yokoi, T.; Okubo, T. Incorporation process of Ti species into the framework of MFI type zeolite. *Microporous Mesoporous Mater.* **2008**, *112*, 202–210. [CrossRef]
23. Wang, J.G.; Yokoi, T.; Kondo, J.N.; Tatsumi, T.; Zhao, Y.L. Titanium(IV) in the Organic-Structure-Directing-Agent-Free Synthesis of Hydrophobic and Large-Pore Molecular Sieves as Redox Catalysts. *ChemSuschem* **2015**, *8*, 2476–2480. [CrossRef]
24. Luna, F.J.; Ukawa, S.E.; Wallau, M.; Schuchardt, U. Cyclohexane oxidation using transition metal-containing aluminophosphates (MAPO-VFI). *J. Mol. Catal. A-Chem.* **1997**, *117*, 405–411. [CrossRef]
25. Prech, J.; Cejka, J. UTL titanosilicate: An extra-large pore epoxidation catalyst with tunable textural properties. *Catal. Today* **2016**, *277*, 2–8. [CrossRef]
26. Balkus, K., Jr.; Gabrielov, A.; Zones, S. The synthesis of UTD-1, Ti-UTD-1 and Ti-UTD-8 using CP* 2CoOH as a structure directing agent. *Stud. Surf. Sci. Catal.* **1995**, *97*, 519–525.
27. Přech, J.; Kubů, M.; Čejka, J. Synthesis and catalytic properties of titanium containing extra-large pore zeolite CIT-5. *Catal. Today* **2014**, *227*, 80–86. [CrossRef]

28. Sever, R.R.; Alcala, R.; Dumesic, J.A.; Root, T.W. Vapor-phase silylation of MCM-41 and Ti-MCM-41. *Micropor. Mesopor. Mater.* **2003**, *66*, 53–67. [CrossRef]
29. Barrett, P.A.; Díaz-Cabañas, M.J.; Camblor, M.A.; Jones, R.H. Synthesis in fluoride and hydroxide media and structure of the extra-large pore pure silica zeolite CIT-5. *J. Chem. Soc. Faraday Trans.* **1998**, *94*, 2475–2481. [CrossRef]

catalysts

MDPI

Article

Zn-Co@N-Doped Carbon Derived from ZIFs for High-Efficiency Synthesis of Ethyl Methyl Carbonate: The Formation of ZnO and the Interaction between Co and Zn

Ya-Nan Miao, Yuan Wang, Dong-Hui Pan, Xiang-Hai Song, Si-Quan Xu, Li-Jing Gao and Guo-Min Xiao *

School of Chemistry and Chemical Engineering, Southeast University, Nanjing 211189, China; mmiaoyanan@163.com (Y.-N.M.); wangyuan9108@126.com (Y.W.); ppandonghui@163.com (D.-H.P.); tju109@126.com (X.-H.S.); siquanxu@163.com (S.-Q.X.); gaolj@seu.edu.cn (L.-J.G.)

* Correspondence: xiaogm426@gmail.com; Tel./Fax: +86-25-5209-0612

Received: 12 December 2018; Accepted: 14 January 2019; Published: 17 January 2019

Abstract: In this work, a series of Zn-Co@N-doped carbon materials were prepared by pyrolysis of Co/Zn-ZIF precursors under a N_2 atmosphere and used for high-efficiency synthesis of ethyl methyl carbonate (EMC) from dimethyl carbonate (DMC) and diethyl carbonate (DEC). The Co to Zn molar ratio and calcination temperature were varied to study the physical and chemical properties of Zn-Co@N-doped carbon materials identified by X-ray diffraction (XRD), scanning electron microscopy (SEM), transmission electron microscopy (TEM), X-ray photoelectron spectroscopy (XPS), Brunauer-Emmett-Teller (BET), inductively coupled plasma (ICP), thermogravimetric analysis (TG) and temperature programmed desorption (TPD) analysis. It was deduced that the formation of a ZnO crystalline structure and the interaction between zinc and cobalt providing weak basic sites and strong basic sites, respectively, in different samples significantly affected their catalytic performance. The catalyst activated the reaction most effectively when the Co to Zn molar ratio was 1.0 and calcination temperature was 600 °C. With the DMC to DEC molar ratio controlled at 1:1, a superior yield of around 51.50% of product EMC can be gained over catalyst ZnCo/NC-600 at 100 °C with 1 wt% catalyst loading in 7 h.

Keywords: zeolitic imidazolate frameworks; Zn-Co@N-doped carbon; transesterification

1. Introduction

Ethyl methyl carbonate (EMC) is the simplest asymmetric ester and an important intermediate in organic synthesis. Recently, EMC has received extensive attention as an excellent co-solvent in the electrolyte of lithium ion batteries [1–5]. Considering security and environmental issues, the traditional method of producing EMC by methyl chloroformate and ethanol was abandoned. Instead, transesterification between dimethyl carbonate (DMC) and ethanol with mild reaction conditions and a high utilization rate of atoms is the most common method for the preparation of EMC [6–8]. However, the by-product methanol should be removed in a timely way to achieve high EMC yield, and the formation of an azeotropic system increases the difficulty of separation and energy consumption [9]. The disadvantages of the above route have contributed to the development of alternative methods, such as the transesterification reaction between dimethyl carbonate and diethyl carbonate (DEC), which is environmentally-friendly, with high atom utilization and mild reaction conditions. Moreover, in the transesterification system, reactants and products can be directly used as co-solvents in the electrolyte without further separation [10,11].

Initially, most catalysts applied to the transesterification reaction between DMC and DEC were homogeneous [12], bringing about separation problems. Subsequently, a number of more economical and environmentally friendly heterogeneous catalysts have been reported. A series of solid base catalysts, including MgO, ZnO, La_2O_3 and CeO_2, were prepared by Shen et al. [13], among which MgO showed best catalytic performance, followed by ZnO. However, the activity of a single metal oxide as the catalyst was not particularly good. Hence, supporter or new metals promoting the transformation of the composition or structure of the available catalyst were introduced to enhance catalytic activity. Zhao et al. [14] prepared carbon-supported catalysts (MgO/NC-2) with an impregnation method in which active sites were effectively dispersed on the surface of supporter, and the EMC yield reached up to 49.3% at optimum conditions. Furthermore, a few bimetallic catalysts were reported, presenting relatively higher EMC yields compared with single metal catalysts due to the interaction between different metals [15,16]. For instance, acid-base bifunctional mesoporous catalysts, which combined specific properties of the acid-base materials and the chemical stability of the mesoporous structure, were prepared with varying metal types (Mg or Al) and the catalysts promoted equilibrium of the transesterification reaction being approached in 30 min [17].

Recently, metal organic frameworks (MOFs) made up of metal ions and organic ligands have attracted widespread attention in different fields, such as gas adsorption and storage [18,19], molecular separation [20,21], catalysts [22,23] as well as drug delivery [24,25], due to their porous structures and high thermal stability [26–28]. Meanwhile, several groups applied MOF materials, in which metal ions acted as acid sites, to transesterification between DMC and DEC since the reaction was essentially an acid-base catalyzed process. Zhou et al. [29] reported that MOF-5 [$Zn_4(O)(BDC)_3$] (BDC = benzene-1, 4-dicarboxylate) showed superior catalytic performance in this reaction, with 50.1% DEC conversion and almost 100% EMC selectivity. Moreover, zeolitic imidazolate frameworks (ZIFs) consisting of metal ions (Zn^{2+}, Co^{2+}), imidazole and derivatives were also active catalysts for the transesterification, providing not only acid sites but also basic sites compared with general MOF materials. Chizallet et al. [30] proved theoretically that Zn^{2+} performed as acid sites, combined with N^- moieties and OH groups as basic sites, determining the catalytic performance of ZIF-8. For further experimental verification, Zhou et al. [31] found that ZIF-8 synthesized at room temperature showed excellent activity, selectivity and stability. The yield of the target product, EMC, reached 50.7% under moderate conditions (0.208 g catalyst, 100 °C and 3 h).

As reported, ZIF materials rich in metallic elements also act as precursors to prepare metal/C or metal oxide/C for further treatment [32–34]. For corresponding derivatives, the porous morphology of ZIF materials can be maintained after low-temperature pyrolysis under an inert atmosphere [35]. Besides, it has been proved that porous N-doped carbon derived from ZIF materials can be applied to alkali catalytic reactions due to the presence of basic sites [36]. Hence, we proposed a new material combining the structure, as well as the properties, of ZIFs and the coordination of two metals. In this study, bimetallic Co/Zn-ZIFs were firstly synthesized using the one-pot method and utilized as the precursor to prepare Zn-Co@N-doped carbon. A series of materials were prepared with different metal molar ratios and calcination temperatures to study the role of Zn and Co and their impact on the formation of active sites. Then, Zn-Co@N-doped carbon as a catalyst was applied to the transesterification reaction between DMC and DEC. Reaction conditions were optimized on the basis of EMC yield and selectivity.

2. Results and Discussion

2.1. Characterization of Catalysts

Zn-Co@N-doped carbon materials labeled as $ZnCo_x$/NC-T (x represents the molar ratio, T is the mark of calcined temperature) were synthesized at room temperature using a simple method, as shown in Scheme 1. In the preparation process, Co/Zn-ZIF with uniform cubic shapes was successfully obtained, as displayed in the SEM images in Figure S1. The XRD pattern of prepared

Co/Zn-ZIF shown in Figure S2 is consistent with the reported literature and there was no marked difference in the pattern of synthesized ZIF-8 [37], implying that the incorporation of cobalt resulted in hardly any destruction of the structure of the ZIF materials. Then, a pre-determined amount of the above light purple powder was transformed into bimetallic particles supported by porous carbon.

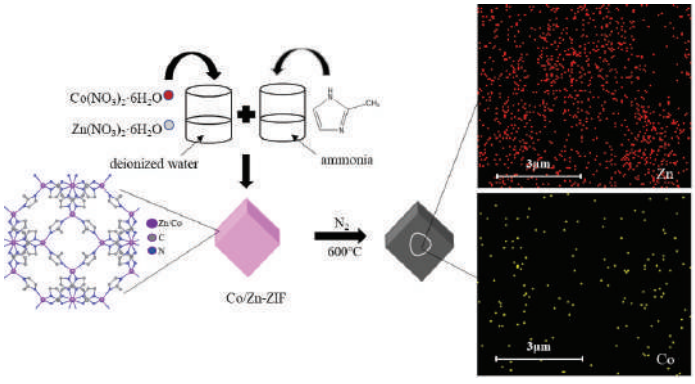

Scheme 1. Synthesis process of Zn-Co@N-doped carbon.

Characteristics of the calcined products were determined by XRD, and the patterns of catalysts calcined under N_2 atmosphere with different molar ratios and calcination temperature are shown in Figure 1. Clearly, $ZnCo_{0.6}$/NC-600 and $ZnCo_{1.4}$/NC-600 are amorphous (Figure 1A). The catalysts (ZnCo/NC-550, ZnCo/NC-650, ZnCo/NC-700) with calcination temperatures above or below 600 °C, and the molar ratio fixed at 1.0, also failed in the formation of crystalline structures, which agrees with a previous report [38]. Instead, a crystalline structure formed when the Co to Zn molar ratio was controlled from 0.8 to 1.2 with a calcined temperature of 600 °C. As shown in Figure 1B, the characteristic peak of ZnO with hexagonal wurtzite crystal structures (JCPDS card No. 36-1451) can be observed in all the crystalline samples. This suggests that zinc elements of the precursor have changed to zinc oxides after heat treatment, even under a nitrogen atmosphere, probably attributed to the higher electrode potential of Zn^{2+}/Zn than −0.27 eV [36]. More importantly, it was demonstrated that the ZnO crystalline structure is essential to the catalytic activity of Zn-Co materials (this will be discussed later). Although the molar ratio of Co to Zn was close to 1.0, no obvious signals of metallic cobalt and oxides of cobalt can be detected for catalysts $ZnCo_{0.8}$/NC-600 after local enlargement of patterns (Figure 1C). As the molar ratio increased up to 1.0, a weak peak at around 44.22° can be observed corresponding to the (1 1 1) plane of the metallic cobalt phase (JCPDS card No.15-0806). Further enhancement of the cobalt amount results in the stronger intensity of this catalyst $ZnCo_{1.2}$/NC-600. However, no peak assigned to oxides of cobalt can be found in any samples. These results suggest that the Co to Zn molar ratio in all samples was far lower than the theoretical value. Cobalt particles are probably uniformly distributed on the surface of the carrier. On the other hand, the crystallinity of cobalt is relatively low at 600 °C [39]. It is also worth noting that the characteristic peaks (Zn 2p) of catalysts doped with cobalt shift to lower diffraction angles compared with calcined products of ZIF-8. This may be attributable to the interaction between zinc and cobalt [40].

Moreover, XPS analyses of catalysts were conducted to identify their chemical composition. The existence of elements including cobalt, zinc, carbon, oxygen and nitrogen was confirmed by XPS spectra (Figure 2A). Zn 2p patterns of catalysts with different metal molar ratios are shown in Figure 2B. Two peaks centered at the binding energy of 1044.9 eV and 1021.9 eV are apparent in the patterns, implying the presence of zinc oxides in accordance with XRD analysis. With the addition of cobalt

elements, the binding energy of Zn $2p_{1/2}$ and $2p_{3/2}$ increased a little, probably due to the chemical environment of zinc and the interaction between zinc and cobalt [40].

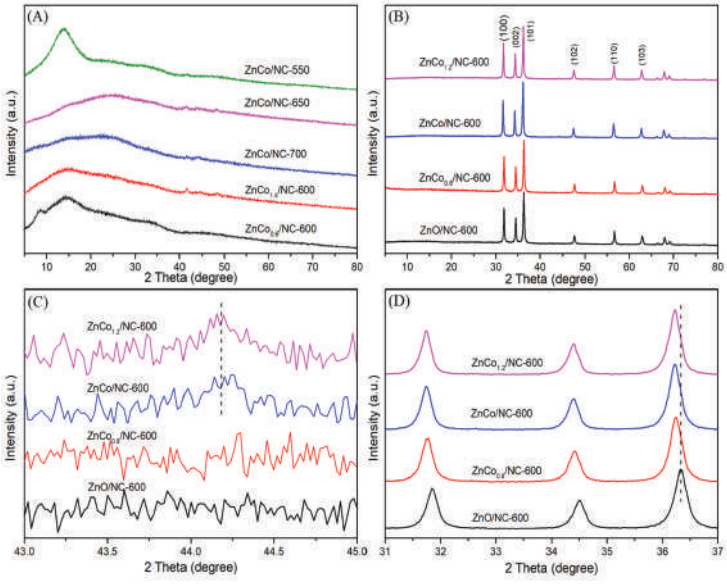

Figure 1. XRD patterns of: (**A**) catalysts with amorphous structure; (**B**) catalysts with crystalline structure. Local enlargement of XRD patterns: (**C**) 43–45°, (**D**) 31–37°.

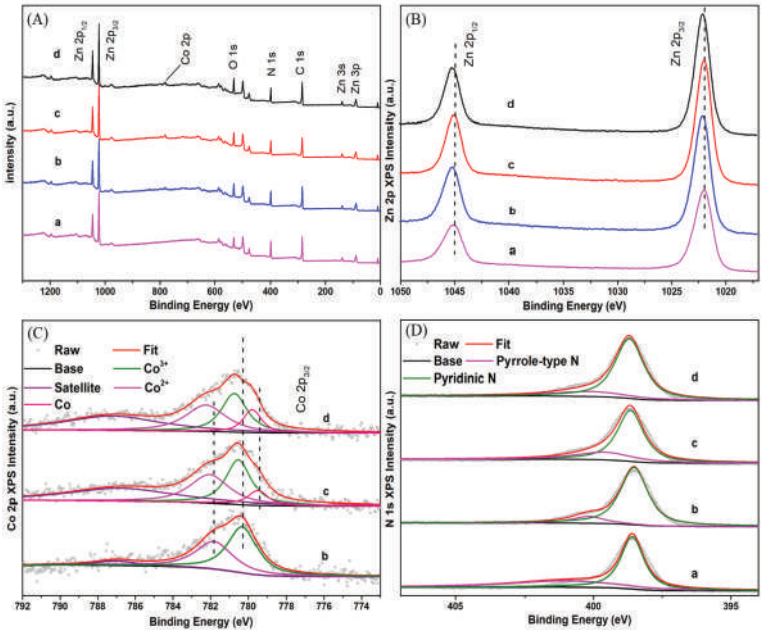

Figure 2. XPS spectra of (a) ZnO/NC-600, (b) $ZnCo_{0.8}$/NC-600, (c) ZnCo/NC-600 and (d) $ZnCo_{1.2}$/NC-600: (**A**) full range XPS spectra; (**B**) Zn 2p spectra; (**C**) Co 2p spectra; (**D**) N 1s spectra.

Calcined products display complicated valence sates of cobalt in the Co 2p patterns (Figure 2C). Two peaks located at around 782 eV and 780.4 eV were detected in all samples, ascribed to the different valence states (Co^{2+}, Co^{3+}) of cobalt oxides. Meanwhile, the satellite peaks at around 786.9 eV in all samples also indicated the presence of cobalt oxides [41]. Banerjee et al. [42] proposed that only metal ions with their electrode potential higher than −0.27 V contained in MOFs could be reduced to zero-valent metals under an inert atmosphere. Thus, it is suggested that the neutral electrode potential of Co^{2+}/Co (−0.27 V) probably accounts for the complex valence sates of cobalt. With the increase of Co elements in catalysts ZnCo/NC-600 and $ZnCo_{1.2}$/NC-600, the peak of metallic cobalt appears and the binding energy of cobalt in all valence states shown in Figure 2C, remarkably, shifts to higher positions [43]. Clearly, the cobalt incorporation leads to the shift of the characteristic peak both in Zn 2p and Co 2p patterns. Hence, the XRD and XPS results together illustrate that the interaction between zinc and cobalt may generate in calcined catalysts, and further are probably linked with catalytic performance.

Most nitrogen elements of the precursor Co/Zn ZIF were preserved after heat treatment under a nitrogen atmosphere. The N 1s spectra of different samples were decomposed into different peaks according to the different chemical states of N (Figure 2D). Apart from the peak centered at around 398.4 eV as evidence of pyridinic-N, a weak peak can also be observed at 400.4 eV implying that a pyrrolic-N exists in the catalyst [39]. Pels et al. [44] reported that pyrrolic-N (N-5) was stable at temperatures as high as 600 °C and above that temperature N-5 disappeared, gradually converting to pyridinic-N (N-6) and quaternary-N (N-Q). Moreover, the preserved N not only acted as a carrier to avoid the agglomeration of particles but also bonded with metal atoms [39,45].

SEM was carried out to investigate morphology and microstructure characteristics of the bimetallic Zn-Co catalysts with different metal molar ratios. As can been seen from Figure 3A,B, the cubic structure of the precursor ZIF-8 was maintained after calcination at 600 °C under a nitrogen atmosphere. The SEM patterns shown in Figure 3C,D of catalyst ZnCo/NC-600 cannot be well distinguished from the above ZnO/NC-600, indicating that the addition of the Co element apparently did not destroy the morphology and microstructure of the ZIFs. The preservation of N was further verified by SEM/EDX mapping (Figure S3 A-2) which displays the dispersion of different elements in catalyst ZnO/NC-600. Additionally, it is remarkable that the distribution density of cobalt was less than that of zinc (Figure S3 B-1,B-2), suggesting that the Co to Zn molar ratio was probably less than 1, in accordance with the XRD results. Combined with ICP analysis (Table S2), we speculate that cobalt nitrate may partly react with ammonia, producing cobalt ammine complexes during the catalyst preparation, which lead to the decrease of cobalt.

To further characterize particle dispersion and the average size of calcined catalysts, HRTEM experiments were also performed. Similar to the SEM results, Zn/Co bimetallic catalysts after thermal treatment also had cubic shapes dimly visible in the HRTEM images (Figure 4A). In ZnCo/NC-600, uniform dispersion of zinc and cobalt particles embedded in carbon matrix can be clearly observed (Figure 4B). Lattice spacings of 0.26 nm, 0.25 nm and 0.20 nm in Figure 4C correspond to the interplanar spacings of ZnO (0 0 2), ZnO (1 0 1) and Co (1 1 1), which correlates with the XRD analysis. Moreover, the particle size distribution image of ZnCo/NC-600 is listed in Figure 4D and the mean size is about 24 nm, which shows it undergoes an obvious increase compared with that of ZnO/NC-600 (Figure 4F).

The BET surface area, pore volume and average pore size of five samples are illustrated in Table 1 to identify the porosity of catalysts determined by nitrogen adsorption–desorption isotherms. The precursor Co/Zn-ZIF displays a relatively high BET surface area of around 1168.3 m^2/g. After calcination, there is a sharp decline in BET surface area. Compared to ZnO/NC-600 (BET surface area 715.6 m^2/g and average pore size 5.38 nm), the incorporation of cobalt results in a decrease of BET surface area and the increase of average pore size. Furthermore, it (Entry 2–5) reveals a positive variation trend between BET surface area and Co loading amount, but a negative one between average pore size and Co loading amount, suggesting that excessive cobalt may lead to the collapse of the catalyst structure.

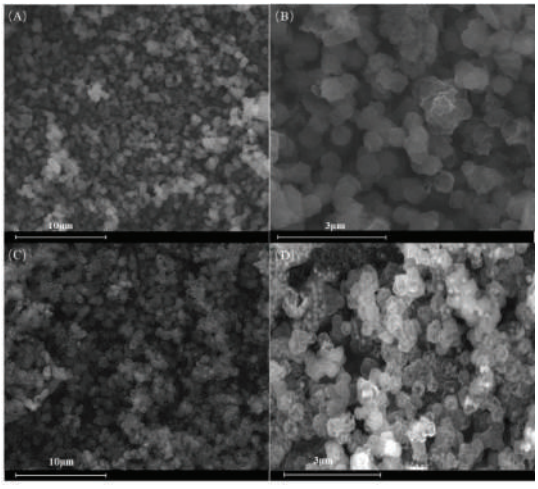

Figure 3. SEM images of: (**A,B**) ZnO/NC-600; (**C,D**) ZnCo/NC-600.

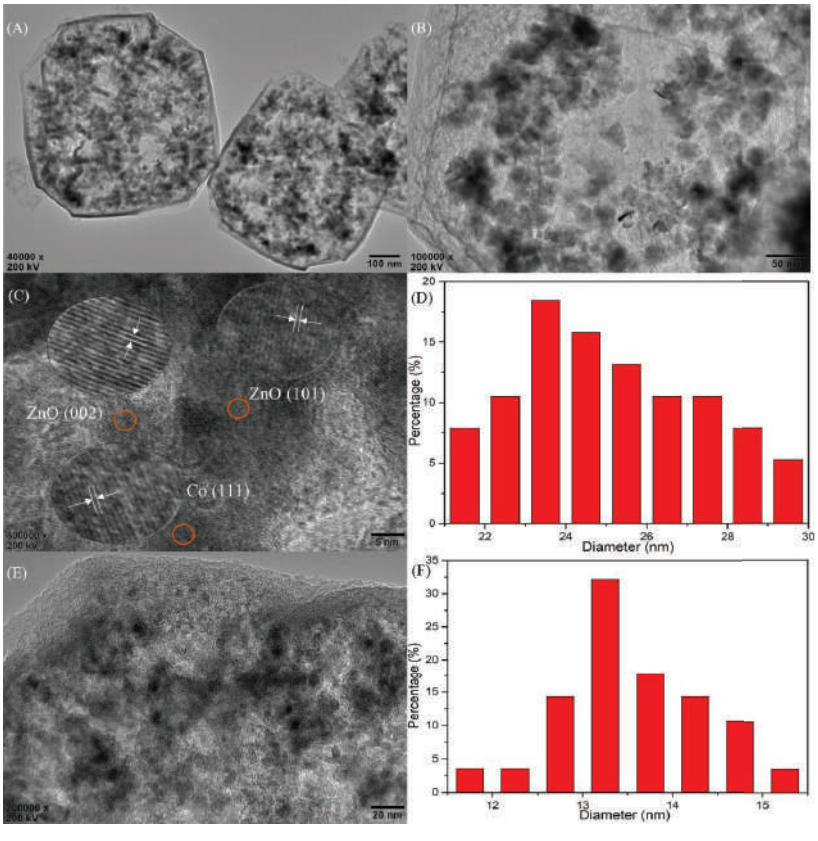

Figure 4. (**A**–**C**) HRTEM images of ZnCo/NC-600; (**D**) particle size distributions of ZnCo/NC-600; (**E**) HRTEM images of ZnO/NC-600; (**F**) particle size distributions of ZnO/NC-600.

Table 1. Surface area, pore volume and average pore size of catalysts.

Entry	Catalyst	S_{BET} (m^2/g)	V_p (cm^3/g)	d_p (nm)
1	Co/Zn-ZIF	1168.3	0.074	10.15
2	ZnO/NC-600	715.6	0.144	5.38
3	$ZnCo_{0.8}$/NC-600	275.0	0.295	11.15
4	ZnCo/NC-600	254.8	0.274	11.72
5	$ZnCo_{1.2}$/NC-600	200.8	0.535	12.18

The CO_2-TPD profiles of different samples to determine the base properties of catalysts are exhibited in Figure 5. As can be seen, curves of samples clearly drift upward over 500 °C, probably due to the decomposition of minor Co/Zn-ZIF. For further verification, a blank run of ZnO/NC-600 without CO_2 adsorption (Figure 5g) was investigated. It shows that the curve displays an up-trend with two peaks clearly centered between 400 °C and 500 °C, and around 746 °C, respectively. In addition, the TG curves of ZnCo/NC-600 obtained in N_2 reveal that the compound suffered from weight loss at a similar temperature (Figure S4). Hence, the above two peaks can be attributed to catalyst decomposition and should be ignored in TPD analysis. Extra peaks, with the exception of decomposition peaks, cannot be detected in the NH_3-TPD profiles (Figure S5), implying the absence of acid sites in the Zn-Co samples. For catalyst ZnO/NC-600 (Figure 5c), a single desorption peak appears around 100 °C and extends into a broad peak, indicating a single alkali type and weak basic sites. A peak centered at a similar temperature can also be observed in other samples (Figure 5c–f), which can be ascribed to the presence of ZnO [30]. With the incorporation of cobalt, the peak centered over 600 °C, as the symbol of strong basic sites, was detected. For comparison, samples calcined from single ZIF-67 and a mechanical mixture of ZIF-67 and ZIF-8 (1:1) were identified by TPD analysis and the results (Figure 5a,b) showed that the peak centered over 600 °C was missing. To sum up, strong basic sites over 600 °C cannot generate in the absence of Zn or Co, and the mechanical mixing of two elements also prevents their formation. Cosimo et al. [46,47] discovered in similar experimental research that Li/MgO exhibited the strongest basic properties, and further assumed that the appearance of these basic sites resulted from the addition of lithium, causing a structural promotion of the MgO sample by replacing the Mg^{2+} ions with Li^+ in the MgO lattice. Based on this foundation, Song et al. [39] proposed a hypothesis that the strong basic sites in catalyst Li/ZnO originated from [Li^+ O^-] attributing to the substitution of Zn^{2+} by Li^+ in the ZnO lattice. In this work, it has been proved in the above analysis that Co together with Zn simultaneously exist in the framework of the Co/Zn-ZIF precursor instead of simply being attached to the surface. Hence, it can be inferred that the interaction between Zn and Co in the lattice promotes the generation of strong basic sites. Furthermore, compared with $ZnCo_{0.8}$/NC-600 and $ZnCo_{1.2}$/NC-600, the peak ascribed to strong basic sites in ZnCo/NC-600 is located at the higher temperature. Hence, we speculate that ZnCo/NC-600 may show the best catalytic performance in the reaction between DMC and DEC, for the reason that stronger basic sites promote interesterification more effectively [39].

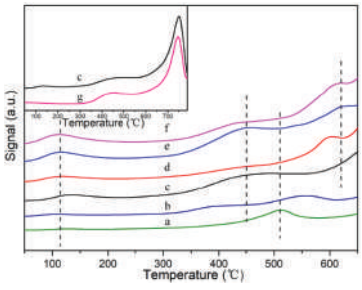

Figure 5. CO_2-TPD profiles of: (a) CoO_x/NC-600 calcined from ZIF-67; (b) $CoZnO_x$/NC-600 calcined from the mechanical mixture of ZIF-67 and ZIF-8 (1:1); (c) ZnO/NC-600; (d) $ZnCo_{0.8}$/NC-600; (e) ZnCo/NC-600; (f) $ZnCo_{1.2}$/NC-600; (g) ZnO/NC-600 without CO_2 adsorption.

2.2. Synthesis of EMC across Different Zn-Co@N-Doped Carbon Materials

Mild transesterification between dimethyl carbonate (DMC) and diethyl carbonate (DEC) was carried out, the reactants of which mainly convert into ethyl methyl carbonate (EMC). Table 2 shows EMC yield under unified conditions catalyzed by a series of catalysts with different metal molar ratios and calcination temperatures.

Table 2. Catalytic performance of different catalysts [a].

Entry	Catalysts	n(DMC):n(DEC)	Yield (%)	Selectivity (%)
1	ZnO/NC-600	1:1	29.50	~100
2	$ZnCo_{0.6}$/NC-600	1:1	2.26	~100
3	$ZnCo_{0.8}$/NC-600	1:1	43.58	~100
4	ZnCo/NC-600	1:1	51.50	~100
5	$ZnCo_{1.2}$/NC-600	1:1	42.53	~100
6	$ZnCo_{1.4}$/NC-600	1:1	–	–
7	ZnCo/NC-550	1:1	0.91	~100
8	ZnCo/NC-650	1:1	9.33	~100
9	ZnCo/NC-700	1:1	1.82	~100

[a] Reaction conditions: 100 °C, 7 h, 1 wt% catalyst amount.

With almost no by-product generated, the EMC selectivity can reach close to 100% when catalyzed by all samples displayed in the Table 2. Unsatisfactory EMC yield was obtained using the mono-metallic catalyst ZnO/NC-600 in which ZnO acted as the single alkali site, as confirmed by TPD results, although the 29.5% yield was a little higher than previously reported for ZnO catalysts probably due to the increase of surface area and the presence of N interacted with metals as active sites [13]. Afterwards, cobalt elements in the form of nitrate were added into the mother liquor for the reason that the synergy between different metals can improve the activity and selectivity of catalysts [48,49]. For catalyst ZnCo/NC-600, the EMC yield dramatically reached 51.5%, twice that of the reaction catalyzed by ZnO/NC-600. The TPD results show that the interaction between Zn and Co in the lattice promotes the generation of strong basic sites in Zn-Co catalysts, suggesting that apart from ZnO active sites, the interaction between zinc and cobalt can also remarkably enhance catalyst activity.

Metal molar ratios of Co to Zn were varied from 0.6 to 1.4 in order to achieve catalysts with superior catalytic performance. It deserves to be mentioned that the EMC yield decreased regardless of whether Co to Zn molar ratios increased or decreased from 1:1. Hence, adding a moderate amount of cobalt activated the catalyst, instead of simply assuming that the more cobalt loading the better the catalytic performance would be. It is probable that the basic sites of ZnO, which have been proved to be the main catalytic active sites, were covered with the improvement of cobalt elements. It can be seen from Table 2 that as Co to Zn molar ratios increased to 1.4 or decreased to 0.6, the EMC yield underwent a rapid decline from 51.5% to 2.26% even 0%.

Additionally, for different catalysts with the Co to Zn molar ratio fixed at 1.0 and calcined under temperatures from 550 °C to 700 °C, ZnCo/NC-600 has the best catalytic performance. Combined with XRD results, when catalysts with no crystalline structure formed on the surface of the carrier were added, the reaction suffered from an unexpectedly lower EMC yield. Based on the above experiments, it is reasonable to infer that the non-formation of a crystalline structure may be responsible for the less active performance of these catalysts, even compared to ZnO/NC-600 calcined directly from ZIF-8. Hence, the presence of zinc oxides, together with the interaction between zinc and cobalt, can be further proved to play the role of catalytic sites in these materials.

2.3. Effects of Reaction Conditions

In order to optimize reaction conditions, the effects of reaction time, temperature and catalyst loading on the yield of EMC were investigated over catalyst ZnCo/NC-600. As shown in Figure 6A,

the EMC yield increased steadily as the reaction time lengthened from 0 to 7 h and reached 51.5% in 7 h. However, no remarkable increase of EMC yield can be observed over 7 h, or even up to 10 h, suggesting that equilibrium can almost be reached in 7 h. Thus, the optimum reaction time is 7 h.

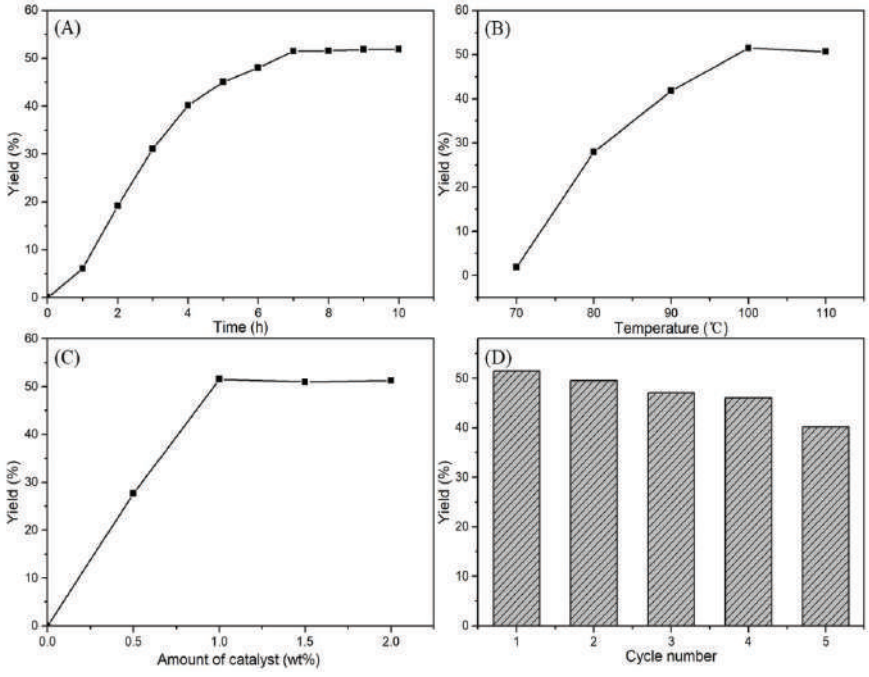

Figure 6. (**A**) Effect of time (100 °C, 1 wt% catalyst amount); (**B**) effect of temperature (7 h, 100 °C, 1 wt% catalyst amount); (**C**) effect of catalyst amount (7 h, 100 °C); (**D**) reusability of the catalyst ZnCo/NC-600 (7 h, 100 °C, 1 wt% catalyst amount).

The impact of temperatures ranging from 70 °C to 110 °C on the EMC yield was studied. Figure 6B illustrates that ZnCo/NC-600 performed unsatisfactory catalytic activity with the EMC yield lower than 5% at 70 °C. Also, it was found that the yield of EMC increased with the increase of the reaction temperature, and the maximum yield (51.5%) was obtained at 100 °C. However, the EMC yield declined slightly when the temperature was elevated to 110 °C. It is likely that sustained loss of DMC, due to its relatively low boiling point (90 °C), may result in the decrease of EMC yield with the raising of the reaction temperature.

As can be seen from Figure 6C, the yield of EMC was also strongly influenced by catalyst loading. Obviously, no EMC can be detected in the absence of any catalyst. With the lower addition of catalyst ZnCo/NC-600, 27.68% of EMC yield is achieved at the same reaction conditions. The yield of EMC increases sharply when the catalyst loading increases from 0.5 wt% to 1 wt%. However, the EMC yield undergoes a slight decline with further increasing of catalyst loading. It is reasonable to infer that excessive catalyst loading may influence the rate of mass transfer which resulted in the relatively slightly lower yield in 7 h. These results may suggest that sufficient catalytic sites provided by appropriate loading of catalyst promote the transesterification between DMC and DEC. Hence, 1 wt% catalyst of reactants is optimum for this reaction considering both EMC yield and industrial cost.

Figure S7 also presents the comparative results of different DMC to DEC molar ratios over catalyst ZnCo/NC-600. Consistent with theoretical analysis, the yield of EMC improved with the increase of the DMC to DEC molar ratio, and even rose to 81.56% with the ratio controlled at 5:1. This discovery

has great industrial significance by increasing the use of low-cost reactants to achieve higher product yield. However, the EMC percentage after reaction undergoes an obvious decline, which increases the difficulty of separation and purification. Hence, the above two results should be taken into consideration in combination.

2.4. Recycling of the Catalyst

Considering the cost, it is important to study the reusability of the heterogeneous catalyst in order to determine the applicability to industrial processes. After the completion of reaction, used catalyst was separated simply by filtration, washed with ethanol three times, and then dried at 80 °C in an oven overnight. Then, the reaction was conducted using 1 wt% amount of catalyst ZnCo/NC-600 at 100 °C for 7 h. The recycle process was conducted five times, and the catalytic performance of the reused catalyst is exhibited in Figure 6D. It reveals that the yield of EMC decreased from 51.5% to 40.19% after five cycles of reaction, indicating that ZnCo/NC-600 displayed relatively good stability during the recycles. Then, the used catalyst was characterized to verify the reasons for the small loss of EMC yield. As shown in Figure 7A, catalyst ZnCo/NC-600, after five recycles, has the same characteristic peaks ascribed to ZnO as the fresh one. Furthermore, combined with TG analysis (Figure S4), this suggests that the structure of the catalyst has not been damaged. However, local enlargement of the XRD (Figure 7A) shows that the characteristic peak of spent ZnCo/NC-600 shifts to a higher position, implying a decreased interaction between zinc and cobalt. Moreover, the intensity of peaks ascribed to ZnO, and the interaction between zinc and cobalt, becomes lower than the fresh catalyst (Figure 7B). Also, it can be proved from ICP analysis (Table S2) that Zn and Co suffered a nearly one-half mass loss after five cycles. Hence, the leaching of metal elements may lead to deactivation of the catalyst.

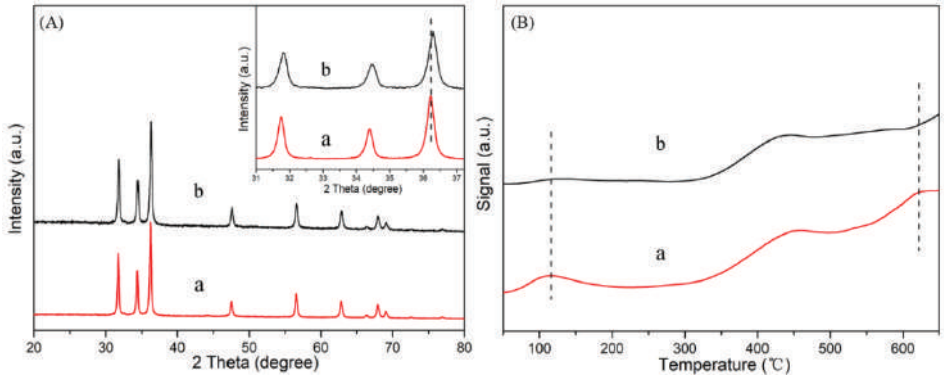

Figure 7. (**A**) XRD patterns of: (a) fresh ZnCo/NC-600 and (b) ZnCo/NC-600 after five cycles; (**B**) CO_2-TPD profiles of: (a) fresh ZnCo/NC-600 and (b) ZnCo/NC-600 after five cycles.

To further understand the reason for catalyst deactivation, a leaching experiment was performed. A transesterification process where the reaction was stopped after 3 h, and then continued after filtering out the solid catalyst, was conducted in comparison to another reaction with its equilibrium approached in 7 h. The results (Figure 8) illustrate that the EMC yield increased slightly, within 5%, for another 4 h in spite of the removal of catalysts, implying the presence of a small amount of active component in the reaction system. Hence, we further believe that the leaching of active sites may account for the deactivation of the catalyst in the reaction and recycle process.

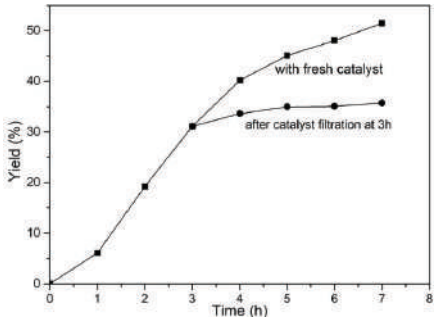

Figure 8. Leaching test in the transesterification of DMC with DEC over fresh ZnCo/NC-600 and after catalyst filtration at 3 h. Reaction conditions: 100 °C, 7 h, 1 wt% catalyst amount.

2.5. Reaction Mechanism

The mechanism of this reaction has been well-studied and reported in previous literature [10,29]. Based on the above analysis in this study, a possible reaction mechanism for the transesterification between DMC and DEC is proposed as shown in Scheme 2. DMC and DEC were firstly absorbed on the basic sites of Zn-Co catalyst, and then intermediates were formed on the surface. The carbonyl of DMC was attacked by ethoxy ion and the carbonyl of DEC was attacked by methoxy ion. The steps were affected by the base properties of the catalyst and other reaction conditions, such as temperature and catalyst amount. Finally, product EMC was detached from the catalyst surface.

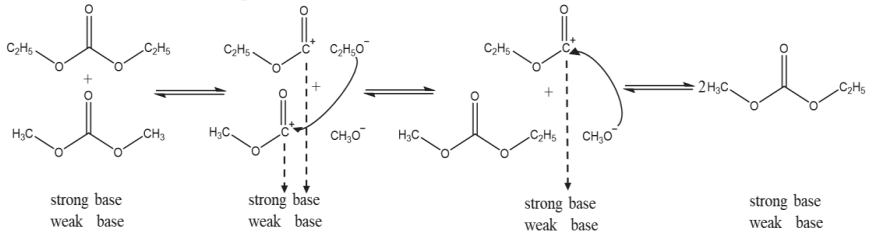

Scheme 2. Possible reaction mechanism over Zn-Co@N-doped carbon.

3. Materials and Methods

3.1. Catalyst Preparation

All chemical reagents were of analytical grade and used as received without further purification. Co/Zn-ZIFs were synthesized from an aqueous solution according to the previous literature with a little modification [37]. Typically, 2 mmol mixture of $Zn(NO_3)_2{\cdot}6H_2O$ (≥99%, Sinopharm Chemical Reagent Co., Ltd, Shanghai, China) and $Co(NO_3)_2{\cdot}6H_2O$ (≥98.5%, Sinopharm Chemical Reagent Co., Ltd, Shanghai, China) with designed molar ratio, and 4 mmol 2-methylimidazole (99%, Sinopharm Chemical Reagent Co., Ltd, Shanghai, China) were separately dissolved in 3 mL deionized water and 4.2 mL ammonia (25–28 wt%, Sinopharm Chemical Reagent Co., Ltd, Shanghai, China). Then, two solutions were quickly mixed and changed into brown. The mixture was stirred continuously for 6 h at room temperature. After centrifugation, the product was washed with deionized water and methanol several times until pH of around 7 was reached, and dried at 80 °C overnight. Then, Co/Zn-ZIF was prepared.

In order to synthesize bimetallic Zn-Co@N-doped carbon materials, Co/Zn-ZIF was calcined in nitrogen for 2 h at a predefined temperature. The heating rate of the pipe furnace was set at 5 °C/min. After cooling to room temperature, a black solid was obtained and labeled $ZnCo_x$/NC-T, where x

represents the molar ratio of Co to Zn ranging from 0.6 to 1.4 and T is the mark of calcined temperature between 550 °C and 700 °C.

For comparison, ZIF-8 was synthesized by the same method and sent to the pipe furnace calcined at 600 °C to obtain ZnO/NC-600.

3.2. Characterization of Catalysts

X-ray diffraction (XRD) patterns of the catalysts were recorded on an X-ray diffractometer (Ultima IV, Rigaku, Kyoto, Japan) using Cu Kα as the radiation source (40 kV and 40 mA). The scanning range (2θ) was from 5° to 80°, with a scanning rate of 20°·min^{-1}.

The morphologies and microstructures of prepared catalysts were investigated using a FESEM scanning electron microscopy (SEM, FEI Inspect F50, Hillsborough, OR, USA) with an accelerating voltage of 15.0 kV. Additionally, the mapping of energy dispersive X-ray spectrometer (EDX, Quanta 250, Hillsborough, OR, USA) was conducted to measure the dispersion of different elements.

High-resolution transmission electron microscopy (HRTEM) was performed on a transmission electron microscopy (JEM-2100F, JEOL, Kyoto, Japan) operated at 200.0 kV.

The X-ray photoelectron spectroscopy (XPS) was recorded with a spectrometer (ESCALAB-250Xi, Thermo Scientific, Waltham, MA, USA) with Al Kα (1486.6 eV) radiation. The obtained element binding energy was calibrated and corrected using the peak of C (1s) at 284.6 eV as references.

The nitrogen adsorption-desorption isotherms were recorded with an analyzer (3H-2000, Beishide, Beijing, China). Prior to measurement, the samples were degassed under vacuum at 200 °C for 12 h. The surface area was obtained using the multipoint Brunauer-Emmett-Teller (BET) method while pore volume and pore size were calculated using the Barrett-Joyner-Halenda (BJH) method.

The concentration of elements was measured by an inductively coupled plasma optical emission spectrometer (ICP-OES, Varian 720-ES, Palo Ato, CA, USA).

Thermogravimetric analysis (TG) was conducted with a thermogravimetric analyzer (STA 449C FS, NETZSCH, Bavaria, Germany). The experiment was performed under N_2 atmosphere and the samples were heated from room temperature to 900 °C at a heating rate of 20 °C per minute.

Temperature programmed desorption (TPD) was carried out to determine the properties of the samples, using a catalyst analyzer (TP-5076, Xianquan, Tianjin, China) equipped with a thermal conductivity detector (TCD). Typically, 0.1 g sample was pretreated under an He atmosphere at 300 °C for 1 h to exclude moisture and other adsorbed gases at the flow rate of 30 mL·min^{-1}. After cooling to room temperature, the catalyst was exposed to pure CO_2 or ammonia gas to conduct the adsorption process for 0.5 h, and then flushed again with He flow (30 mL·min^{-1}) for at least 50 min to remove redundant and physically adsorbed gas. Then, the sample was heated to 800 °C at a rate of 10 °C min^{-1} under a constant He flow to obtain the CO_2 or ammonia gas desorption curve.

3.3. Reaction Procedure

Interesterification between dimethyl carbonate (DMC) and diethyl carbonate (DEC) was carried out in a 50 ml three-necked flask equipped with a reflux condenser and a magnetic stirring. In a typical reaction, 9 g (0.1 mol) DMC (99.5%, Sinopharm Chemical Reagent Co., Ltd, Shanghai, China), 11.8 g (0.1 mol) DEC (99.5%, Sinopharm Chemical Reagent Co., Ltd, Shanghai, China) and 0.2 g (1 wt% of reactants) catalysts were mixed into the flask. Then the mixture was heated to a predetermined temperature with continuous stirring for the given time. After cooling to room temperature, the product was analyzed using a gas chromatograph (GC-6890, Ouhua, Shanghai, China) equipped with a flame ionization detector (FID) and a capillary column (SE-30, 30 m × 0.25 mm, Agilent, CA, USA). Used catalysts were separated by filtration, washed with ethanol several times and finally dried at 80 °C overnight. Then, the above reaction was repeated using the regenerated catalyst to examine the reusability of catalysts.

4. Conclusions

In summary, bimetallic Zn-Co catalysts carbonized by zeolitic imidazolate frameworks were prepared for high-efficient synthesis of ethyl methyl carbonate. It was demonstrated that the cobalt loading and calcined temperature had a great impact on the catalyst microstructure, particle size, chemical states and further catalytic performance. When the DMC to DEC molar ratio was controlled at 1:1, the best catalytic performance, with 51.50% EMC yield, was obtained over 1 wt% catalyst ZnCo/NC-600 of total reactants at a temperature of 100 °C for 7 h. Combined with the characterization results, it can be inferred that the superior catalytic performance is mainly attributed to the formation of a ZnO crystalline structure, and the interaction between zinc and cobalt providing weak basic sites and strong basic sites, respectively. Moreover, with a simple method, Zn-Co catalysts can be reused for five recycles with only a slight decline in the yield of EMC.

Supplementary Materials: The following are available online at http://www.mdpi.com/2073-4344/9/1/94/s1. Figure S1, SEM images of Co/Zn-ZIF; Figure S2, XRD patterns of different ZIF materials; Figure S3, SEM/EDX mapping of (A) ZnO/NC-600, (A-1) the dispersion of Zn, (A-2) the dispersion of N, (B) ZnCo/NC-600, (B-1) the dispersion of Zn, (B-2) the dispersion of Co, (C) samples calcined from mechanical mixture of ZIF-67 and ZIF-8, (C-1) the dispersion of Zn, (C-2) the dispersion of Co; Figure S4. the TG analysis of ZnCo/NC-600 catalysts, (a) fresh, (b) spent; Figure S5, NH_3-TPD profiles of ZnO/NC-600 and ZnCo/NC-600; Figure S6, the GC analysis of liquid products; Figure S7, effect of molar ratio of DMC to DEC:EMC yield, EMC molar percentage after reaction; Table S1, particle sizes calculated from XRD; Table S2, ICP results of the materials; Table S3, results of CO_2-TPD over catalysts.

Author Contributions: Y.-N.M. and Y.W. conceived and designed the experiments; Y.-N.M. performed the experiments; Y.-N.M. and X.-H.S. analyzed the data; S.-Q.X., L.-J.G. and D.-H.P. provided reagents, materials and analysis tools; Y.-N.M. mainly wrote the paper and all authors revised the paper. All authors have read the final version of the manuscript.

Funding: This work was financially supported by the National Natural Science Foundation of China (Nos. 21276050, 21676054 and 21406034), the Fundamental Research Funds for the Central Universities (Nos. 3207045414, 3207045426) and the Natural Science Foundation of Jiangsu (No. BK20161415).

Conflicts of Interest: The authors declare no conflict of interest.

References

1. Ding, M.S.; Xu, K.; Zhang, S.S.; Amine, K.; Henriksen, G.L.; Jow, T.R. Change of Conductivity with Salt Content, Solvent Composition, and Temperature for Electrolytes of LiPF6 in Ethylene Carbonate-Ethyl Methyl Carbonate. *J. Electrochem. Soc.* **2001**, *148*, A1196–A1204. [CrossRef]
2. Ding, M.S. Liquid Phase Boundaries, Dielectric Constant, and Viscosity of PC-DEC and PC-EC Binary Carbonates. *J. Electrochem. Soc.* **2003**, *150*, A455–A462. [CrossRef]
3. Ue, M.; Mori, S. Mobility and Ionic Association of Lithium Salts in a Propylene Carbonate-Ethyl Methyl Carbonate Mixed Solvent. *J. Electrochem. Soc.* **1995**, *142*, 2577–2581. [CrossRef]
4. Hall, D.S.; Self, J.; Dahn, J.R. Dielectric Constants for Quantum Chemistry and Li-Ion Batteries: Solvent Blends of Ethylene Carbonate and Ethyl Methyl Carbonate. *J. Phys. Chem. C* **2015**, *119*, 22322–22330. [CrossRef]
5. Zhou, H.; Fang, Z.; Li, J. LiPF6 and lithium difluoro (oxalato) borate/ethylene carbonate + dimethyl carbonate + ethyl(methyl)carbonate electrolyte for $Li_4Ti_5O_{12}$ anode. *J. Power Sources* **2013**, *230*, 148–154. [CrossRef]
6. Keller, T.; Holtbruegge, J.; Górak, A. Transesterification of dimethyl carbonate with ethanol in a pilot-scale reactive distillation column. *Chem. Eng. J.* **2012**, *180*, 309–322. [CrossRef]
7. Murugan, C.; Bajaj, H.C. Synthesis of diethyl carbonate from dimethyl carbonate and ethanol using KF/Al_2O_3 as an efficient solid base catalyst. *Fuel Process. Technol.* **2011**, *92*, 77–82. [CrossRef]
8. Zielinska-Nadolska, I.; Warmuzinski, K.; Richter, J. Zeolite and other heterogeneous catalysts for the transesterification reaction of dimethyl carbonate with ethanol. *Catal. Today* **2006**, *114*, 226–230. [CrossRef]
9. Zhang, X.; Zuo, J.; Jian, C. Experimental Isobaric Vapor-Liquid Equilibrium for Binary Systems of Ethyl Methyl Carbonate + Methanol, + Ethanol, + Dimethyl Carbonate, or + Diethyl Carbonate at 101.3 kPa. *J. Chem. Eng. Data* **2010**, *55*, 4896–4902. [CrossRef]

10. Palani, A.; Gokulakrishnan, N.; Palanichamy, M.; Pandurangan, A. Transesterification of dimethyl carbonate with diethyl carbonate over Al-Zn-MCM-41 and Al-MCM-41 molecular sieves. *Appl. Catal. A* **2006**, *304*, 152–158. [CrossRef]
11. Yang, L.; Yu, L.; Sun, M.; Gao, C. Zeolitic imidazole framework-67 as an efficient heterogeneous catalyst for the synthesis of ethyl methyl carbonate. *Catal. Commun.* **2014**, *54*, 86–90. [CrossRef]
12. Zhuo, G.; Shen, Z.; Jiang, X. Synthesis of ethyl methyl carbonate by homogeneous catalysis. *Chin. J. Catal.* **2004**, *25*, 171–172.
13. Shen, Z.; Jiang, X.; Zhao, W. A New Catalytic Transesterification for the Synthesis of Ethyl Methyl Carbonate. *Catal. Lett.* **2003**, *91*, 63–67. [CrossRef]
14. Zhao, G.; Shi, J.; Liu, G.; Liu, Y.; Wang, Z.; Zhang, W.; Jia, M. Efficient porous carbon-supported MgO catalysts for the transesterification of dimethyl carbonate with diethyl carbonate. *J. Mol. Catal. A Chem.* **2010**, *327*, 32–37. [CrossRef]
15. Wang, P.; Liu, S.; Ma, X.; He, Y.; Alshammari, A.S.; Deng, Y. Binary Mg–Fe oxide as a highly active and magnetically separable catalyst for the synthesis of ethyl methyl carbonate. *RSC. Adv.* **2015**, *5*, 25849–25856. [CrossRef]
16. Chen, Y.; Han, J.; Zhang, H. Facile synthesis and characterization of acid-base bifunctionalized mesoporous silica. *Appl. Surf. Sci.* **2008**, *254*, 5967–5974. [CrossRef]
17. Wang, J.; Han, L.; Wang, S.; Zhang, J.; Yang, Y. Magnesium Aluminum Spinel as an Acid-Base Catalyst for Transesterification of Diethyl Carbonate with Dimethyl Carbonate. *Catal. Lett.* **2014**, *144*, 1602–1608. [CrossRef]
18. Chen, F.; Bai, D.; Wang, Y.; Jiang, D.; He, Y. A family of ssa-type copper-based MOFs constructed from unsymmetrical diisophthalates: Synthesis, characterization and selective gas adsorption. *Mater. Chem. Front.* **2017**, *1*, 2283–2291. [CrossRef]
19. Xue, Z.Z.; Zhang, D.; Pan, J.; Han, S.D.; Li, J.H.; Wang, G.M. A porous copper-organic framework with intersecting channels and gas adsorption properties. *Dalton Trans.* **2017**, *46*, 13952–13956. [CrossRef]
20. Khan, N.A.; Jhung, S.H. Adsorptive removal and separation of chemicals with metal-organic frameworks: Contribution of pi-complexation. *J. Hazard. Mater.* **2017**, *325*, 198–213. [CrossRef]
21. Luo, F.; Yan, C.; Dang, L.; Krishna, R.; Zhou, W.; Wu, H.; Dong, X.; Han, Y.; Hu, T.L.; O'Keeffe, M.; et al. UTSA-74: A MOF-74 Isomer with Two Accessible Binding Sites per Metal Center for Highly Selective Gas Separation. *J. Am. Chem. Soc.* **2016**, *138*, 5678–5684. [CrossRef] [PubMed]
22. Verma, S.; Nasir Baig, R.B.; Nadagouda, M.N.; Varma, R.S. Titanium-based zeolitic imidazolate framework for chemical fixation of carbon dioxide. *Green Chem.* **2016**, *18*, 4855–4858. [CrossRef]
23. Chen, B.L.; Yang, Z.X.; Zhu, Y.Q.; Xia, Y.D. Zeolitic imidazolate framework materials: Recent progress in synthesis and applications. *J. Mater. Chem. A* **2014**, *2*, 16811–16831. [CrossRef]
24. Cai, W.; Chu, C.C.; Liu, G.; Wang, Y.X. Metal-Organic Framework-Based Nanomedicine Platforms for Drug Delivery and Molecular Imaging. *Small* **2015**, *11*, 4806–4822. [CrossRef] [PubMed]
25. Zheng, H.; Zhang, Y.; Liu, L.; Wan, W.; Guo, P.; Nystrom, A.M.; Zou, X. One-pot Synthesis of Metal-Organic Frameworks with Encapsulated Target Molecules and Their Applications for Controlled Drug Delivery. *J. Am. Chem. Soc.* **2016**, *138*, 962–968. [CrossRef] [PubMed]
26. Yin, H.; Kim, H.; Choi, J.; Yip, A.C.K. Thermal stability of ZIF-8 under oxidative and inert environments: A practical perspective on using ZIF-8 as a catalyst support. *Chem. Eng. J.* **2015**, *278*, 293–300. [CrossRef]
27. Park, K.; Ni, Z.; Côté, A.P.; Choi, J.; Huang, R.; Uribe-Romo, F.J.; Chae, H.K.; O'Keeffe, M.; Yaghi, O.M. Exceptional chemical and thermal stability of zeolitic imidazolate frameworks. *Proc. Natl. Acad. Sci. USA* **2006**, *103*, 10186–10191. [CrossRef]
28. Banerjee, R.; Phan, A.; Wang, B.; Knobler, C.; Furukawa, H.; O'Keeffe, M.; Yaghi, O.M. High-Throughput Synthesis of Zeolitic Imidazolate Frameworks and Application to CO_2 Capture. *Science* **2008**, *319*, 939–943. [CrossRef]
29. Zhou, Y.; Song, J.; Liang, S.; Hu, S.; Liu, H.; Jiang, T.; Han, B. Metal-organic frameworks as an acid catalyst for the synthesis of ethyl methyl carbonate via transesterification. *J. Mol. Catal. A Chem.* **2009**, *308*, 68–72. [CrossRef]
30. Chizallet, C.; Lazare, S.; Bazer-Bachi, D.; Bonnier, F.; Lecocq, V.; Soyer, E.; Quoineaud, A.; Bats, N. Catalysis of Transesterification by a Nonfunctionalized Metal-Organic Framework: Acido-Basicity at the External Surface of ZIF-8 Probed by FTIR and ab Initio Calculations. *J. Am. Chem. Soc.* **2010**, *132*, 12365–12377. [CrossRef]

31. Zhou, X.; Zhang, H.P.; Wang, G.Y.; Yao, Z.G.; Tang, Y.R.; Zheng, S.S. Zeolitic imidazolate framework as efficient heterogeneous catalyst for the synthesis of ethyl methyl carbonate. *J. Mol. Catal. A Chem.* **2013**, *366*, 43–47. [CrossRef]
32. Gai, P.; Zhang, H.; Zhang, Y.; Liu, W.; Zhu, G.; Zhang, X.; Chen, J. Simultaneous electrochemical detection of ascorbic acid, dopamine and uric acid based on nitrogen doped porous carbon nanopolyhedra. *J. Mater. Chem. B* **2013**, *1*, 2742. [CrossRef]
33. Xia, W.; Mahmood, A.; Zou, R.; Xu, Q. Metal-Organic Frameworks and their derived nanostructures for Electrochemical Energy Storage and Conversion. *Energy Environ. Sci.* **2015**, *8*, 1837–1866. [CrossRef]
34. Wu, M.; Ye, H.L.; Zhao, F.Q.; Zeng, B.Z. High-Quality Metal-Organic Framework ZIF-8 Membrane Supported on Electrodeposited ZnO/2-methylimidazole Nanocomposite: Efficient Adsorbent for the Enrichment of Acidic Drugs. *Sci. Rep.* **2017**, *7*, 39778. [CrossRef] [PubMed]
35. Chaikittisilp, W.; Hu, M.; Wang, H.; Huang, H.S.; Fujita, T.; Wu, K.C.; Chen, L.C.; Yamauchi, Y.; Ariga, K. Nanoporous carbons through direct carbonization of a zeolitic imidazolate framework for supercapacitor electrodes. *Chem. Commun. (Camb.)* **2012**, *48*, 7259–7261. [CrossRef]
36. Jiang, H.L.; Liu, B.; Lan, Y.Q.; Kuratani, K.; Akita, T.; Shioyama, H.; Zong, F.; Xu, Q. From metal-organic framework to nanoporous carbon: Toward a very high surface area and hydrogen uptake. *J. Am. Chem. Soc.* **2011**, *133*, 11854–11857. [CrossRef] [PubMed]
37. He, M.; Yao, J.; Liu, Q.; Wang, K.; Chen, F.; Wang, H. Facile synthesis of zeolitic imidazolate framework-8 from a concentrated aqueous solution. *Microporous Mesoporous Mater.* **2014**, *184*, 55–60. [CrossRef]
38. Han, Y.; Qi, P.; Li, S.; Feng, X.; Zhou, J.; Li, H.; Su, S.; Li, X.; Wang, B. A novel anode material derived from organic-coated ZIF-8 nanocomposites with high performance in lithium ion batteries. *Chem. Commun. (Camb.)* **2014**, *50*, 8057–8060. [CrossRef] [PubMed]
39. Wang, X.; Li, Y. Chemoselective hydrogenation of functionalized nitroarenes using MOF-derived co-based catalysts. *J. Mol. Catal. A Chem.* **2016**, *420*, 56–65. [CrossRef]
40. Song, X.; Wu, Y.; Cai, F.; Pan, D.; Xiao, G. High-efficiency and low-cost Li/ZnO catalysts for synthesis of glycerol carbonate from glycerol transesterification: The role of Li and ZnO interaction. *Appl. Catal. A* **2017**, *532*, 77–85. [CrossRef]
41. Wang, Y.; Miao, Y.; Li, S.; Gao, L.; Xiao, G. Metal-organic frameworks derived bimetallic Cu-Co catalyst for efficient and selective hydrogenation of biomass-derived furfural to furfuryl alcohol. *Mol. Catal.* **2017**, *436*, 128–137. [CrossRef]
42. Das, R.; Pachfule, P.; Banerjee, R.; Poddar, P. Metal and metal oxide nanoparticle synthesis from metal organic frameworks (MOFs): Finding the border of metal and metal oxides. *Nanoscale* **2012**, *4*, 591–599. [CrossRef] [PubMed]
43. Collinge, G.; Xiang, Y.; Barbosa, R.; McEwen, J.S.; Kruse, N. CO-induced inversion of the layer sequence of a model CoCu catalyst. *Surf. Sci.* **2016**, *648*, 74–83. [CrossRef]
44. PELs, J.R.; Kapteijn, F.; Moulijn, J.A.; Zhu, Q.; Thomas, K.M. Evolution of nitrogen functionalities in carbonaceous materials during pyrolysis. *Carbon* **1995**, *33*, 1641–1653. [CrossRef]
45. Zhang, L.; Wang, A.; Wang, W.; Huang, Y.; Liu, X.; Miao, S.; Liu, J.; Zhang, T. Co-N-C Catalyst for C-C Coupling Reactions: On the Catalytic Performance and Active Sites. *ACS Catal.* **2015**, *5*, 6563–6572. [CrossRef]
46. Di Cosimo, J.I.; Díez, V.K.; Apesteguía, C.R. Base catalysis for the systhesis of α, β-unsaturated ketones from the vapor-phase aldol consendation of acetone. *Appl. Catal. A* **1996**, *137*, 149–166. [CrossRef]
47. Díez, V.K.; Apesteguía, C.R.; Di Cosimo, J.I. Acid-base properties and active site requirements for elimination reactions on alkali-promoted MgO catalysts. *Catal. Today* **2000**, *63*, 53–62. [CrossRef]
48. Seemala, B.; Cai, C.M.; Kumar, R.; Wyman, C.E.; Christopher, P. Effects of Cu-Ni Bimetallic Catalyst Composition and Support on Activity, Selectivity, and Stability for Furfural Conversion to 2-Methyfuran. *ACS Sustain. Chem. Eng.* **2018**, *6*, 2152–2161. [CrossRef]
49. Verma, S.; Nasir Baig, R.B.; Nadagouda, M.N.; Varma, R.S. Hydroxylation of Benzene via C–H Activation Using Bimetallic CuAg@g-C_3N_4. *ACS Sustain. Chem. Eng.* **2017**, *5*, 3637–3640. [CrossRef]

catalysts

MDPI

Review

Review on the Macro-Transport Processes Theory for Irregular Pores able to Perform Catalytic Reactions

Iván Santamaría-Holek [1,*,†], Saúl I. Hernández [1,†], Consuelo García-Alcántara [1,†] and Aldo Ledesma-Durán [2,*,†]

[1] Unidad Multidiscliplinaria de Docencia e Investigación-Juriquilla, Facultad de Ciencias, Universidad Nacional Autónoma de México, Juriquilla, Querétaro CP 76230, Mexico; saul.ivan.hernandez@ciencias.unam.mx (S.I.H.); consuelo.garcia@unam.mx (C.G.-A.)

[2] Centro de Física Aplicada y Tecnología Avanzada CFATA, Universidad Nacional Autónoma de México (UNAM), Juriquilla, Querétaro CP 76230, Mexico

* Correspondence: isholek.fc@gmail.com (I.S.-H.); aldo_ledesma@ciencias.unam.mx (A.L.-D.)

† These authors contributed equally to this work.

Received: 22 February 2019; Accepted: 15 March 2019; Published: 19 March 2019

Abstract: We review and generalize a recent theoretical framework that provides a sound physicochemical basis to describe how volume and surface diffusion are affected by adsorption and desorption processes, as well as by catalytic conversion within the space defined by the irregular geometry of the pores in a material. The theory is based on two single-dimensional mass conservation equations for irregular domains deduced for the volumetric (bulk) and surface mass concentrations. It offers a powerful tool for analyzing and modeling mass transport across porous media like zeolites or artificially build materials, since it establishes how the microscopic quantities that refer to the internal details of the geometry, the flow and the interactions within the irregular pore can be translated into macroscopic variables that are currently measured in experiments. The use of the theory in mass uptake experiments is explained in terms of breakthrough curves and effective mass diffusion coefficients which are explicitly related to the internal geometry of the pores.

Keywords: generalized macro-transport theory; adsorbent and non-adsorbent membranes; bulk and surface diffusion; heterogeneous catalysis; mass transfer and effectiveness factor

1. Introduction

The Shaphiro–Brenners's theory for macrotransport processes was an outstanding contribution to the understanding of macrotransport processes in applied chemistry. The theory offered simplified equations with effective transport coefficients suitable to reduce the time and computational necessities for predicting the optimal conditions of different experimental or technological situations. The theory was inspired on the classical Taylor–Aris dispersion problem, in which the three-dimensional diffusion of a particle in the presence of a flow in a pipe is reduced to a single dimensional problem along the longitudinal coordinate of the pipe [1,2]. The main consequence of this contraction or projection of the mathematical description implies that the microscopic structure of the system is incorporated in the value or possible dependence of the corresponding transport coefficients, like the diffusivity, on the essential parameters of the problem. That is, after the microscopic structure is suitably abstracted, the local "microscopic" transport coefficients become "macrotransport" coefficients. In this way, the theory emphasizes the fact that the macroscopic character of well known three-dimensional transport equations, for instance, the diffusion equation with its boundary conditions, implies an inherently complex and heterogeneous system that cannot be ignored. The enormous merit of the theory is that it offers a rigorous mathematical formulation for doing this contraction of the description along with the incorporation of chemical aspects related with chemical kinetics [3].

The Shaphiro–Brenners's macrotransport processes theory focuses on the effect of flow in regular domains, as the Taylor–Aris problem set. Nonetheless, in real life regular geometries are scarce. Most practical situations involving mass or charge transport across membranes or porous media involve irregular domains and, therefore, require a more general treatment than the one offered by the original macrotransport processes theory. For instance, the mass transport inside confined geometries addressed interesting problems that should be studied in order to improve our understanding of several processes occurring on Biology, Chemistry and many industrial applications ranging from metallurgy to food processing [4–6]. Some of the most important examples of this type of transport occurs in biological membranes, zeolites, carbon nanotubes, transformation of hydrocarbons, soil filtration, chemical reactors and artificial thin films. A few examples are mentioned in Refs. [7–10].

Most experimental techniques related with porous materials pertain to the macro-scale, defined in terms of the global characteristic length of the system like, for instance, a reaction cell [11–14]. In those techniques, the quantities of flowing reagents and products are measured at the ends of the material. These properties have to reflect several processes taking place at the micro-scale, defined in terms of the transversal characteristic length of the pores, the real length and other internal properties [15–20]. The relation between the microscopic details of the shape of the pores and the longitudinal effective mass transport across porous materials can be established accurately when the pores are long enough compared with their average width [21]. When this assumption holds, the microscopic scale description based on the three-dimensional diffusion equation can be simplified onto a coarse grained description along the main transport direction, that is, onto a one dimensional diffusion equation having effective transport coefficients [22–25].

Some of the advantages that follow from this coarse graining of the description are technical, like the reduction of computing time when solving the time evolution equations with their corresponding (non-equilibrium) boundary conditions. However, also interesting physical chemistry concepts emerge from this contraction of the description. Concepts like entropic forces as a result of entropic restrictions, or effective reaction velocity constants and their influence on the overall behavior of the system allow to have simplified interpretations of the processes involved that are consistent with the microscopic details, in similar form as other branches of physics, like in the case of statistical mechanics and thermodynamics [26–29].

The present article generalizes to three dimensionsa novel approach to this problem that was recently formulated for the case of non-regular domains in two dimensions [16,18,21,30,31]. In this alternative or generalized macrotransport process theory, the non-regularity of the geometry of the pores is explicitly taken into account when the description is contracted. It leads to contributions correcting the transport coefficients and the effective chemical rates that may be very useful in practical applications, especially when the perspective on 3D printing is emerging as a very promising membrane fabrication technique [32].

This new approach enriches the view offered by the Shaphiro–Brenners's theory for macrotransport processes, and can lead to an improvement of the theoretical description and understanding of several processes taking place in constrained transport problems. It makes accessible the connection between the microscopic details of the geometrical and chemical structure of the pore with the result of macroscopic experiments. This will be illustrated by considering a series of examples that show the main features and richness of the theoretical description and its capacities to design technological devices able to perform, optimally, specific functions.

This work is organized as follows. In Section 2 we will present the main features of the generalized macrotransport process theory for irregular geometries and then, in Sections 3 and 4 we will extend it to the case when adsorption–desorption kinetics takes place at the pores surface and to the case when the adsorbed phase can diffuse on the surface, respectively. The case of heterogeneous catalysis is considered in Section 5, and the effective diffusion coefficient of adsorbent and non- adsorbent membranes is studied in the Section 6. In Section 7 we discuss how our theory can be used together

with experiments, in order to infer some general characteristics of pores from uptake experiments. Finally, the Summary and Conclusions are presented in Section 8.

2. A Generalized Macrotransport Process Theory for Irregular Domains

Consider the transport of a gas of a pure substance across a pore like the one illustrated in Figure 1. The molecules of the gas may interact among them and with the walls of the pore and, in general, they may be adsorbed and desorbed. At the local level and with isothermal conditions the spatial and temporal evolution of the state of the gas of a pure substance can be characterized by the following general mass balance equation inside the pore [33]

$$\frac{\partial C}{\partial t} + \nabla \cdot \mathbf{j} = G(r, \phi, z, t), \tag{1}$$

where $C(r, \phi, z, t)$ represents the concentration of molecules in mol·cm^{-3} (or ·cm^{-2} in the 2D case) and $G(r, \phi, z, t)$ is the chemical production or consumption inside the bulk of the fluid, having dimensions of mol·cm^{-2}·s^{-1}. In addition ∇ represents the gradient operator in cylindrical coordinates.

When one considers that the molecules can be adsorbed and desorbed at the pore walls, the total diffusion current $\mathbf{j}(r, \phi, z, t)$, having dimensions of mol·cm^{-2}·s^{-1}, can be written as the sum of two contributions

$$\mathbf{j}(r, \phi, z, t) = \mathbf{j}^{diff} + \mathbf{j}^{surf}, \tag{2}$$

where $\mathbf{j}^{diff}$ is the diffusive current in the bulk and $\mathbf{j}^{surf}$ is the surface current of material due the existence of adsorption and desorption processes implying the transport of molecules through the pore's surface. The bulk diffusion follows the Fick law

$$\mathbf{j}^{diff}(r, \phi, z, t) = -D \nabla C(r, \phi, z, t), \tag{3}$$

where D is the Fickean-diffusion coefficient [34]. The explicit form of the surface contribution, $\mathbf{j}^{surf}(r, \phi, z, t)$, will depend on the particular chemical kinetics associated with the heterogeneous chemistry. However, in general this quantity should vanish in every internal point of the bulk domain

$$\mathbf{j}^{surf}(r, \phi, z, t) = 0 \qquad r < R(z), \tag{4}$$

whereas, when evaluated at the boundaries, it takes the form

$$\mathbf{j}^{surf}(r = R, \phi, z, t) = \dot{\rho}(z, t) \hat{\mathbf{n}}(R, z), \qquad i = 1, 2, \tag{5}$$

where $\dot{\rho}$ is proportional to the velocity of the corresponding heterogeneous chemical reaction, that is, the input or output of material at the pore's surface. Here, the unit vector normal to the pore surface at position z is $\hat{\mathbf{n}}_{\perp}(R, z)$, see Figure 1. The units of $\dot{\rho}$ are mol·cm^{-2}·s^{-1}. The detailed analysis on the properties of the bulk and surface contributions of the total diffusion current at the boundaries, is provided in Ref. [21].

2.1. Contraction of the Description for Diffusion Processes

The formulation of a theory for macro-transport processes in irregular domains starts by the contraction of the 3D description offered by Equation (1) along the coordinates which are transversal to the main transport direction. Here, for simplicity in the presentation we will assume that this direction coincides with the z-axis, see Figure 1, and that no adsorption and desorption processes or chemical reactions are present ($\mathbf{j}^{surf} = 0$ and $G = 0$).

In this form, the average diffusion *flow* along the main transport direction can be obtained by using the well known relation: $J^{diff} = \int (\mathbf{j}^{diff} \cdot \hat{e}_z) dA$, with $dA = r dr d\phi$ the element of cross section area

with normal vector along the direction of main transport z. Using Equation (3) in the last expression we have

$$J^{diff} = -D \int_0^{2\pi} \int_0^{R(z)} \frac{\partial C}{\partial z} \, r dr d\phi, \tag{6}$$

where we have assumed that D does not depend on r and ϕ. Integration over r can be done using the Leibniz rule due to the irregular boundaries. One obtains

$$J^{diff} = -2\pi D \left[\frac{\partial}{\partial z} \int_0^{R(z)} C(R,z,t) r \, dr - R(z) \, C(R,z,t) \, \frac{\partial R}{\partial z} \right]. \tag{7}$$

Now, it is worth to define the averaged bulk concentration $C_b(x,t)$

$$C_b(z,t) = \frac{1}{\mathcal{A}(z)} \int_0^{R(z)} C(r,\phi,z,t) \, r dr d\phi, \tag{8}$$

having the same units as $C(r,\phi,z,t)$, that is mol·cm^{-3}. Here, we have introduced the transversal area of the pore $\mathcal{A}(z) \equiv \pi R^2(z)$. For non-twisted and large enough ($L >> R$) pores we can assume $C(R,z,t) \simeq C_b(z,t)$, meaning that homogeneity along the radial direction is rapidly reached [21]. Thus, after integrating and performing some algebraic manipulations at the right hand side of Equation (7), we obtain

$$J^{diff} = -D\mathcal{A}(z) \frac{\partial C_b}{\partial z}. \tag{9}$$

In similar form, the integration of the mass conservation equation (Equation (1)) over the transversal coordinates r and ϕ yields

$$\frac{\partial}{\partial t} \left[\mathcal{A}(z) C_b \right] + \frac{\partial}{\partial z} J^{diff} = 0, \tag{10}$$

where we have used Equation (8), the Leibniz rule: $\int_0^{2\pi} \int_0^{R(z)} \frac{\partial}{\partial z} \left(\mathbf{j}^{diff} \cdot \hat{e}_z \right) \, r dr d\phi = \frac{\partial}{\partial z} J^{diff} - J^{diff}|_{r=R} \frac{dR}{dz}$, and assumed non-adsorbing boundary conditions for the diffusion flow at the walls of the pore: $J^{diff}|_{r=R} = 0$. In the following section we will indicate how the projected description has to be modified when adsorbing boundary conditions are considered.

In this way, by substituting Equation (7) into Equation (10) we finally obtain the evolution equation of the averaged bulk concentration $C_b(z,t)$ along the main transport coordinate,

$$\frac{\partial C_b}{\partial t} = \frac{1}{\mathcal{A}(z)} \frac{\partial}{\partial z} \left[D(z) \mathcal{A}(z) \frac{\partial C_b}{\partial z} \right]. \tag{11}$$

This equation is the appropriate one-dimensional mass conservation relation for a diffusion process that originally takes place in a three-dimensional irregular domain with fixed and reflective boundaries. It should be noticed that the presence of the position dependent transversal area $\mathcal{A}(z)$, introduces important modifications to the differential operator associated with the diffusion process. Furthermore, it is convenient to stress that, in general, the diffusion coefficient entering into Equation (11) is a position dependent quantity, see Equation (15) below. The justification of this fact and an explicit form of this dependence in terms of the geometry of the pore are given in the next subsection.

These differences with respect to the usual diffusion equation imply that, when one approximates the description of a three-dimensional diffusion process with a simple diffusion equation of the form:

$$\frac{\partial C_{1D}}{\partial t} = D_m \frac{\partial^2 C_{1D}}{\partial z^2}, \tag{12}$$

then careful should be put on what the constant effective diffusivity D_m implies. An equation like Equation (12) was rigorously derived from Equation (11) in Ref. [30], where the connection between the molecular diffusion coefficient D and the effective membrane diffusivity D_m was given in terms of the geometry of the pores. The final expression is consistent with the experimental inference

$$D_m = D_0 \frac{\varphi}{\tau} \delta, \tag{13}$$

where D_0 is the molecular diffusion coefficient of the particles in the bulk phase in absence of confinement, and φ and τ are the *porosity* and *tortuosity* of the membrane, respectively. The symbol δ is called the *constriction factor* since it quantifies, in an averaged form, the effect of the internal corrugation of the pores on the mass flux. In particular, the inverse $1/\delta$ is a measure of the intrinsic resistance of a pore to the flow. The theoretical deduction of Equation (13) in Ref. [30] establishes rigorous mathematical relations for the experimental macroscopic parameters φ, τ and δ, in terms of the geometrical parameters of the pores, in such a way that they can be useful for pore design.

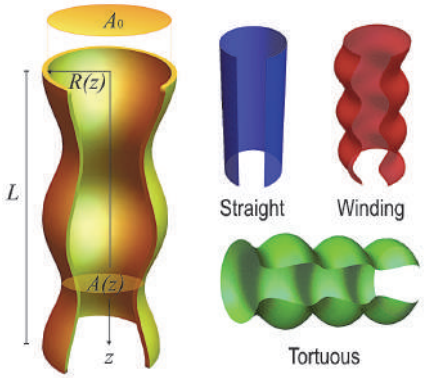

Figure 1. Geometry of an irregular tortuous pore of radius $R(z)$, transversal area $A(z)$ and length L. Also shown are the three types of pores that will be used for numerical experiments. These experiments will consist on the study of the bulk and surface diffusion dynamics and its interplay with the adsorption–desorption and catalytic processes at the surface of the pore. The mathematical details of their geometries are summarized in Appendix A, in particular the values of the geometric parameters used in simulations are provided in Table A1.

The mass balance equation Equation (11) has many advantages since it is written in terms of the volumetric concentration. The first one is that it is easy to connect it with the boundary conditions which are of practical importance in the chemical reaction engineering. For example, the cases when an external gradient is imposed on the porous material: $C_b(0) \neq C_b(L)$, with $z = 0$ and $z = L$ the extremes of the pore, see Figure 1. Another example is when saturation conditions are imposed on an initially empty material: $C_b(0) = C_b(L) = C_0$ with C_0 a constant. This quality of Equation (11) is very important because in an experimental setup these conditions are usually the measurable or controllable parameters. Therefore, the Equation (11) allows one to establish in a detailed way the concentration profile (usually not measured) in terms only of the external condition, as long as the internal shape of the pore is known.

2.2. The Diffusion Coefficient in the Contracted Description

The contracted description we have already presented, can be related with the Fick–Jacobs–Zwanzig description of Brownian motion at irregular domains [22]. In this case, valid for equilibrium situations, one should assume a very diluted gas in such a way that the probability density is proportional to the concentration of molecules: $P \propto C$. When this assumption is valid,

the Equation (11) can be rewritten in terms of the reduced probability p: $P \simeq p/\mathcal{A}(z)$, which is a linear density. The result is the Fick–Jacobs–Zwanzig equation

$$\frac{\partial p}{\partial t} = \frac{\partial}{\partial z}\left[D(z)\mathcal{A}\frac{\partial}{\partial z}\left(\frac{p}{\mathcal{A}}\right)\right]. \tag{14}$$

The interesting point here is that the diffusion coefficient entering in Equation (14) is position dependent, i.e., $D = D(z)$. Several expressions for the functional form of this coefficient have been obtained for the two-dimensional problem [22,23,29,35]. However, in three dimensions, and only for illustrative purposes, it is convenient to write down the form reported in Ref. [36] for a three-dimensional cylindrical tube:

$$D(z) = \frac{D_0}{1 + h_z^2(z) + \frac{R_z^2(z)}{2}}. \tag{15}$$

Here $h(z)$ is the middle line of the pore, $R(z)$ its local width and the subscript z denotes derivation respect to this coordinate. Therefore, in the contracted description, the diffusion coefficient is reduced by the constriction (proportional to R_z^2) and by the sinuosity (proportional to h_z^2) of the pore. These parameters are involved in the definitions of φ, τ and δ. For more details, see Refs. [18,30,31].

3. Adsorption–Desorption Kinetics in Macrotransport Process Theory for Irregular Domains

When the internal surface of a pore is chemically active there is a probability per unit time that a particle which approaches to the wall becomes adsorbed or desorbed. This probability is measured by the contribution $\mathbf{j}^{surf}$ given in Equation (5) and therefore the adsorption–desorption rate por unit area of the pore's surface, $\mathbf{j}^{surf} \cdot \hat{\mathbf{n}} = \dot{\rho}$, is proportional to the velocity of reaction $\dot{\rho}$ which measures how rapidly the particles are leaving the bulk and stay attached at the wall, and vice versa.

Assuming that the adsorbed layer does not modify in an noticeable extent the available volume of particles diffusing in the bulk, one can proceed along the same lines of the last section in order to obtain (see Ref. [21] for details)

$$\frac{\partial C_b}{\partial t} = \frac{1}{\mathcal{A}(z)}\frac{\partial}{\partial z}\left[D(z)\mathcal{A}(z)\frac{\partial C_b}{\partial z}\right] + \frac{\Gamma}{\mathcal{A}}\dot{\rho} \tag{16}$$

where $\Gamma(z)$ is an area density, that is, a purely geometric factor which measures the local surface area of the pore since $\int_0^L \Gamma(z)dz = A_{surf}$; for surfaces of revolution, it has the explicit form $\Gamma(z) = 2\pi R(z)\gamma(z)$, where the length density is $\gamma(z) = \sqrt{1 + R_z^2(z)}$. The factor $\Gamma\dot{\rho}/\mathcal{A}$ has therefore the dimensions of $\mathrm{mol{\cdot}cm^{-3}{\cdot}s^{-1}}$.

The Equation (16) accounts for the spatial and temporal evolution of the bulk concentration of a gas inside a pore having an adsorbing irregular surface. The adsorption–desorption process is therefore weighted by the control parameter $\Gamma(z)/\mathcal{A}(z)$, see the left panel of Figure 2. This means that an increase in the amount of active sites over the wall of the pore [or equivalently, increasing $\Gamma(z)$] produces in turn an increased efficiency of the adsorption–desorption process as it is expected, this is shown in the right panel of Figure 2.

The Equation (16) is the generalization of the macro-transport processes theory to the case when diffusion and adsorption–desorption chemical kinetics may occur. It gives a clue of how to relate the detailed process occurring at the wall with the measurements that only consider the internal volume of the pore. For example, if in a given system the adsorption–desorption process is the slower step of the dynamics, then one can ignore the diffusion process and therefore Equation (16) reduces to

$$\frac{\partial C_b}{\partial t} = 2\gamma(z)\mathcal{R}_b(z,t), \tag{17}$$

where we have identified the reaction velocity $\mathcal{R}_b$ (in mol·cm^{-3}·s^{-1}) of the respective chemical kinetics through the expression

$$\frac{\pi R(z)}{\mathcal{A}(z)}\dot{\rho}(z) = \frac{\dot{\rho}(z)}{R(z)} = \mathcal{R}_b(z,t), \tag{18}$$

in which we made use of the explicit form of the cross area $\mathcal{A}(z)$. This relation quantifies how fast the material is adsorbed-desorbed at position z at time t over the pore surface and therefore, is crucial for understanding the role of the geometric irregularity of the pore when quantifying the adsorption–desorption macroscopic reaction rates. Integration over the length L of the pore yields the macrotransport relation

$$\frac{d\overline{C_b}}{dt} = \overline{\mathcal{R}_b}(t). \tag{19}$$

where we have defined $\overline{C_b} = L^{-1}\int_0^L C_b(z,t)dz$ and $\overline{\mathcal{R}_b} = 2L^{-1}\int_0^L \mathcal{R}_b(z)\gamma(z)dz$. This last expression for the chemical rate is exclusively a time dependent function, but implicitly contains the details of the internal geometry of the pores.

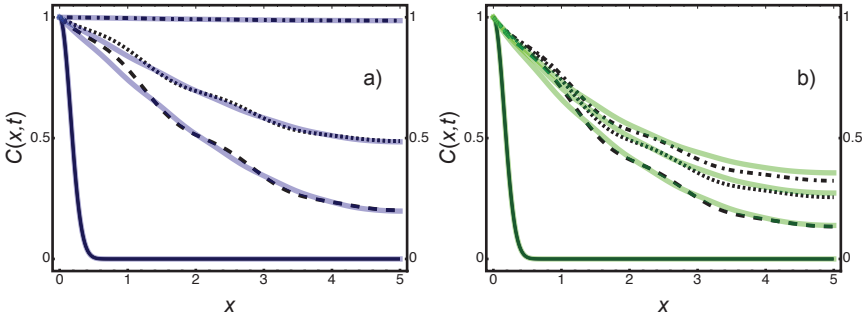

Figure 2. Evolution of the non-equilibrium concentration profiles of the tortuous (black lines) and winding pores (colour lines) in two different situations. In (**a**) we present the diffusion dynamics in the absence of adsorption. Since we have designed the pores for having the same effective diffusion coefficient $D_b(z)$, then the concentration profile evolves equally in both pores. However, in (**b**) we show that the adsorption efficiency is different in both pores because it depends on the length of the walls (proportional to their enhancement factor γ) which is larger in the tortuous pore (black lines) than in the winding pore (colour lines). This fact causes that less particles reach the exit side of the pore (at the right). See Appendix A for details of the simulations.

3.1. The Thiele Modulus

The Equation (16) shows that a porous material of irregular shape increases the efficiency of an adsorption–desorption process by the combination of two factors. In first place, the corrugation and sinuosity of the pore make slower the effective diffusion process along the longitudinal direction, since the diffusion is reduced by a factor of D/D_0 compared with a cylindrical pore. In second place, the corrugation of the pore makes that the surface of the walls is increased by a factor Γ, augmenting in principle the amount of active sites.

Traditionally, both factors can be taken into account in a single characteristic parameter of a chemical reactor called the Thiele modulus, which is defined as the square root of the ratio between the characteristic time of diffusion and the characteristic time of the adsorption–desorption kinetics [16]

$$\Phi^2 = \frac{\text{characteristic time of diffusion}}{\text{characteristic time of adsorption}}. \tag{20}$$

From this definition it is possible to show how the irregularity of the pores locally increases the Thiele modulus Φ with respect to Thiele modulus Φ_0 of a cylindrical pore of radius R_0 with the same

length and no irregularities. Let us assume a first order adsorption process with velocity constant κ $(1/s)$, that is,

$$\mathcal{R}_b(z,t) = -\kappa C_b. \tag{21}$$

Then, from Equation (16) in the stationary state the expression of the Thiele modulus for a cylindrical pore is ($\gamma = 1$): $\Phi_0 = \sqrt{2\kappa \frac{L^2}{D_0}}$. The corresponding expression of the position dependent Thiele modulus for an irregular pore can also be obtained from Equation (16). Introducing the scaled variable $\zeta = z/L$, in the stationary state Equation (16) becomes

$$\frac{\partial^2 C_b}{\partial \zeta^2} = \left(2\gamma\kappa \cdot \frac{L^2}{D}\right) C_b - \frac{\partial C_b}{\partial \zeta} \cdot \frac{\partial}{\partial \zeta} \ln |D\,\mathcal{A}|, \tag{22}$$

where we have used Equation (21) and made some rearrangements. Noticing that the characteristic time of diffusion can be defined by $\tau_{diff} = L^2/D$ and the characteristic time of adsorption by $\tau_{ads} = (2\gamma\kappa)^{-1}$, then the local Thiele modulus $\Phi(z)$ can be defined in complete analogy with Φ_0 by

$$\Phi(z) = \sqrt{2\kappa\gamma \cdot \frac{L^2}{D}}, \tag{23}$$

implying that

$$\frac{\Phi(z)}{\Phi_0} = \sqrt{\gamma \frac{D_0}{D}} = \sqrt{\gamma(z)\left[1 + h_z^2(z) + \frac{R_z^2(z)}{2}\right]} \geq 1, \tag{24}$$

where in the second equality we have used Equation (15). The inequality follows from the fact that $D_0/D(z) \geq 1$ and $\gamma = \sqrt{1 + R_z^2(z)} \geq 1$. Additionally, one may introduce an averaged Thiele modulus which can be defined in the usual form

$$\overline{\Phi} = \frac{\Phi_0}{L} \int_0^L \sqrt{\gamma(z)\left[1 + h_z^2(z) + \frac{R_z^2(z)}{2}\right]}\, dz. \tag{25}$$

The results of the present theory seem to go deeper in the modeling and comprehension of the processes taking place in the system than previous theories. The corrected expressions depending on the corrugations and sinuosity of the pores, show how the internal geometry of the pore affects the amount of material adsorbed or transferred across a membrane. This could be a very relevant knowledge in the cases when one looks for programmed performance properties of a membrane.

Equation (22) predicts that the mass distribution inside the pore will only depend on the Thiele modulus, which becomes corrected by the local values of the length density $\gamma(z)$ and of the diffusion coefficient $D(z)$. From this information and taking into account the definitions of the *mass transfer coefficient* and *effectiveness factor* a very complete description can be achieved. Very detailed examples in two dimensions were previously analyzed in Ref. [16,21]. We will show this in the following section for the case of conical pores.

3.2. An Application: Conic Pores

The utility of the previous results may be illustrated by considering some interesting situations of practical interest, like nano-filtration, among others [37–41]. As an example, consider first that the porous material is a membrane subject to a concentration difference between both ends. In this case, the proportionality k between the net flux and the net concentration difference is called the *coefficient of mass transference* and usually augments with the Thiele modulus. The Equation (22) allows to predict that the presence of throats of specific slopes can increase the transferred material across the membranes and, therefore, increase k in a very appreciable way. At the other hand if we are interested in an equilibrium process where the fluid can enter at both sides of the membrane saturating the membrane, then the internal effectiveness factor η is usually measured [16]. This parameter measures

the ratio between the amount of gas actually adsorbed and that which would be adsorbed if all the internal surface of the pore were exposed to the external concentration. It is known that this parameter η usually decreases with the Thiele modulus. Once more time, the use of Equation (22) allows to predict that the existence of bottlenecks can increase the effectiveness factor in two ways, since the reduction of the volume caused by the funnel causes in turn accumulation of material making the adsorption more efficient, see Figure 3.

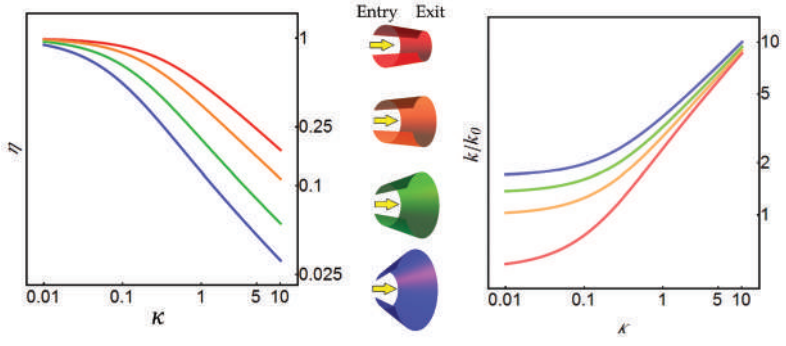

Figure 3. Predictions for the normalized mass transfer coefficient k/k_0 (**left**) and effectiveness factor η (**right**) as a function of the pore geometry, for the four conical pores depicted in the figure using the reduced scheme. See Appendix A.

4. Effect of Diffusion of the Adsorbed Phase over the Internal Pore Surface

When a particle is physically adsorbed at the internal surface of the pore it enters in a very narrow region that is called the *adsorption field*. The length and deepness of the adsorption field is dictated by the type of interaction between host and guest molecules of the solid porous material [42]. In this situation, and adsorbed particle can change its position by two ways. One of them is a simple desorption process which can be described with the same models than adsorption as before, or by other way, it can move along the surface of the pore. This second mechanism is called *surface diffusion* and is caused by short-length interactions among the molecules and the surface. From the practical point of view, it has been suggested that the surface diffusion coefficient is larger than the bulk diffusion, and that can be responsible for most of the effective transport inside porous materials [43–45]. However, as the traditional models for quantifying surface diffusion usually depend of the reactor used, it is hard to deduce general conclusions of this process [46].

In order to establish a one-dimensional description of the concentration of the adsorbed phase along the main transport coordinate, we will assume that the pore surface is non-twisted, i.e., it is independent of the azimuthal coordinate and therefore describable by a single parametric coordinate. This assumption allows us to write, in the limit of zero loading, the parametric coordinate [31]

$$q(z) = \int_0^z \sqrt{1 + R_z^2(z)}dz. \tag{26}$$

The coordinate $q(z)$ can be understood as a measure of the real length traveled by the molecules in the main transport direction. The significance is clear when analyzing the case of a conic pore, see Figure 4a. The diffusion over the surface of the cone is approximately equal to the diffusion over the two dimensional domain indicated in Figure 4b, where the effective length of this domain is defined by $\tilde{L} = \int_0^L \sqrt{1 + R_z^2(z)}dz$.

Hence, the projected concentration of adsorbed molecules along the coordinate q is $s(q,t)$, having dimensions of mol·cm^{-1} along the surface. This concentration satisfies a one-dimensional mass balance equation which comes from the projection of the corresponding two dimensional diffusion equation along the coordinate $q(z)$. This equation is similar to the so-called generalized Fick-Jacobs equation, see Ref. [18,31]

$$\frac{\partial s}{\partial t} = \frac{\partial}{\partial q}\left[D_s\, w \frac{\partial}{\partial q}\left(\frac{s}{w}\right)\right] + g_s, \tag{27}$$

where $w = 2\pi R(q)$ is the width of the two dimensional domain, and g_s (in mol·cm^{-1}·s^{-1}) quantifies the interchange of molecules between the adsorbed phase and the bulk by means of the adsorption–desorption process. Equation (27) is relevant because it provides a clear physical meaning to the surface diffusion coefficient D_s as the proportionality constant between the current density of molecules and the concentration of adsorbed molecules when measured only along the surface. Therefore, this diffusion coefficient can be directly deduced, independently of the type of reactor, from the measurements of the mean square displacement in the limit of zero loading.

From the experimental point of view, the details about the spatial and temporal distribution of the adsorption process are usually ignored. Thus, the theoretical description is done by assuming a general mechanism for the adsorption–desorption kinetics from which one adjusts the chemical rates in terms of the internal concentrations measured. However, these bulk and surface concentrations are known in terms of the internal volume of the pore and, therefore, are measured in mol by unit of internal volume. In this way, for practical purposes, it is necessary to express Equation (27) in terms of volumetric concentrations and of the bare coordinate z, instead of the effective coordinate q. Let us define the concentration of the adsorbed phase C_s (in mol by unit of volume) through the relation

$$C_s = \frac{\gamma}{\mathcal{A}} s, \tag{28}$$

where the length density γ takes into account the re-scaling due to the projection over the effective defined coordinate q. Substituting the last relation into Equation (27) and using the geometric relation Equation (26), we obtain the single dimensional diffusion equation for the concentration of the adsorbed phase C_s

$$\frac{\partial C_s}{\partial t} = \frac{1}{\mathcal{A}}\frac{\partial}{\partial z}\left[4\pi D_s \frac{\mathcal{A}}{\gamma\, w}\frac{\partial}{\partial z}\left(\frac{\mathcal{A}}{\gamma\, w} C_s\right)\right] + \gamma \mathcal{R}_s, \tag{29}$$

where $\mathcal{R}_s = r_s/\mathcal{A}$, and we used the expression for the transversal area $\mathcal{A} = \pi R^2$. The Equation (29) quantifies the concentration distribution of the adsorbed phase as the result of the surface diffusion and the interchange of particles with the bulk phase. In the case when the projection of the dynamics is performed from a two dimensional channel [31], the corresponding mathematical form of the one-dimensional diffusion equation is very similar to the generalization of the Fick-Jacobs equation given in Equation (16). The difference is the form of quantifying the effective mass flux of both diffusive processes.

A striking effect predicted by the above equation is that a macroscopic stationary state can be reached in such a way that the surface and bulk dynamics compensate each other. This effect is shown in Figure 5, where we show this coupling in a sinusoidal pore in the presence of Langmuir adsorption [47]. The presence of inhomogeneities on the surface concentration slaved to the form of the pore induce non-vanishing gradients, that is, induce bulk and diffusion currents developing in opposite directions along z. The result is the apparent formation of condensation-diffusion cells inside the pore [31].

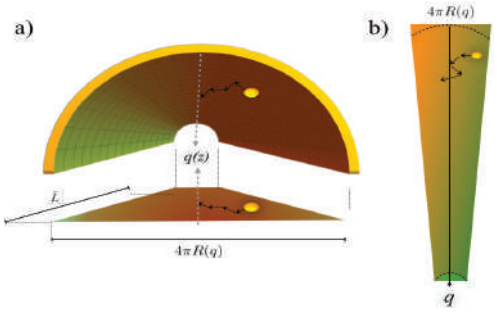

Figure 4. Projection approximation of the diffusion over the surface of a conical pore. (**a**) The effective length q appears due to the projection over the cone. (**b**) The motion along the q coordinate is approximately equal to the motion inside a two-dimensional funnel pore. The semicircular dotted lines indicate the exact form of the surface. For large pores as initially assumed $L >> R$, the error made by our approximation is negligible.

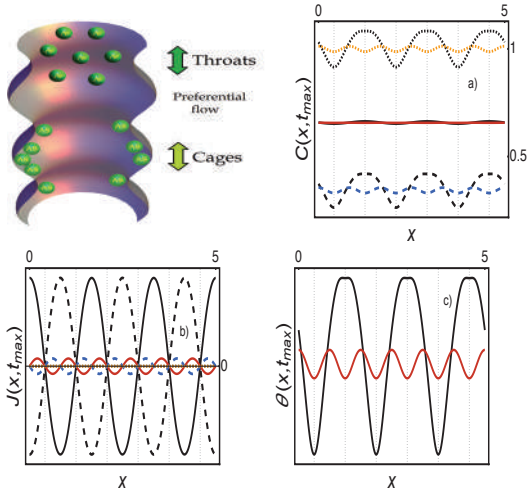

Figure 5. Langmuir adsorption dynamic inside the tortuous (black lines) and winding (color lines) pores in the presence of surface diffusion. In (**a**,**b**) figures the solid-lines correspond to the long-time (equilibrium) bulk concentration $C_b(x)$ and diffusion current $J_b(x)$, the dashed-lines to the long-time (equilibrium) surface concentration $C_s(x)$ and diffusion current $J_s(x)$ and the dotted-lines to the long-time (equilibrium) total concentration $C = C_b + C_s$ and current $J = J_b + J_s$. At long times the particles in the bulk tend to be distributed homogeneously inside the pore while in (**c**) the coverage fraction $\theta(x)$ shows that the adsorbed particles tend to segregate producing an accumulation in the wider regions of the pore. This interesting effect suggests the existence of bulk-surface exchange counter-fluxes in the interior of the pores, even when macroscopic equilibrium is reached. See Appendix A for simulation details.

5. Heterogeneous Catalysis

In previous sections we have presented a theoretical framework that describes the spatial and temporal evolution of the concentration of molecules along axisymmetrical irregular pore whose shape is known, and in which heterogenous reactions and surface diffusion take place. The theoretical framework is summarized by Equations (16) and (29), which separate the processes occurring in

the bulk from those in the adsorbed phase because the diffusion in each case has different origins and magnitudes.

In both equations, the irregularity of the pore geometry enters through the geometric parameters $\mathcal{A}$ and γ, which represent the cross area and the length-density of the walls, respectively. Therefore, if the reaction of adsorption and desorption is known, as well as the bulk and surface diffusion coefficients in the limit of zero concentration, then Equations (16) and (29) allow, in principle, to describe in detail the concentration of any fluid inside the pore.

However, in practice the parameter $\gamma(z)$ is frequently unknown, and therefore the effect of the adsorption–desorption kinetics on the overall transport across the pore or the membrane is only assessed in average form. Thus, in this situation it is convenient to approximate the parameter $\gamma(z)$ in terms of an average *enhancement factor*: $\overline{\gamma} = L^{-1}\int_0^L \gamma(z)dz$, and introduce an operational definition for $\overline{\gamma}$. For a previous discussion on this subject, see Ref. [18,31]

An operational definition $\overline{\gamma}$ can be introduced in terms of the ratio between the reaction velocity constant inside the pore with respect to that of a flat surface. Thus, $\overline{\gamma}$ can be expressed in terms of the net bulk reaction velocity $\tilde{\mathcal{R}} = \overline{\gamma}\,\mathcal{R}$, where $\mathcal{R}$ was defined through Equations (17) to (19). Assuming that the chemical kinetics has an overall characteristic velocity constant κ, like for instance in Equation (21), then we have: $\tilde{\mathcal{R}} = -\overline{\gamma}\kappa C_b$. Thus, as an approximated average measure of the enhancement factor of the reaction due to the fact that the reactions take place into a pore, we may propose the relation

$$\overline{\gamma} \simeq \tilde{\kappa}/\kappa, \tag{30}$$

where $\tilde{\kappa}$ is the effective velocity constant inside the pore, and κ is the velocity constant in a flat surface.

5.1. An Example: The Isomerization Reaction

In this subsection we will illustrate the capabilities of the theory by considering a simple isomerization reaction at the internal surface of the pore [14]. In this example, schematically represented in Figure 6, the particles of A enter the pore with concentration C_b^A. Some are adsorbed at the wall forming the reactive AS with concentration C_s^A:

$$A + S \underset{\mathrm{k_{-A}}}{\overset{\mathrm{k_A}}{\rightleftharpoons}} A \cdot S\,, \tag{31}$$

and therefore with reaction velocity

$$\tilde{\mathcal{R}}_{Ads} = \tilde{\kappa}_{ads}\left(C_b^A\, C_S - K_{ads} C_s^A\right), \tag{32}$$

where $C_S = C_s^0 - C_s^A - C_s^B$ denotes the concentration of vacant sites in the Langmuir-Hinshelwood approximation, and K_{ads} is the equilibrium constant associated with the adsorption–desorption process of species A. Afterwards, the catalytic reaction transforms the reactive AS into the isomer B attached to the wall, BS, with concentration C_s^B:

$$A \cdot S \underset{\mathrm{k_{-S}}}{\overset{\mathrm{k_S}}{\rightleftharpoons}} B \cdot S\,, \tag{33}$$

with the corresponding reaction velocity

$$\tilde{\mathcal{R}}_{Cat} = \tilde{\kappa}_{cat}\left(C_s^A - K_{cat} C_s^B\right), \tag{34}$$

where K_{cat} is the equilibrium constant associated with the catalytic reaction at the surface of the pore.

Finally, the isomer B is desorbed and transported out of the pore, with concentration C_b^B, that is:

$$B \cdot S \underset{\mathrm{k_{-S}}}{\overset{\mathrm{k_S}}{\rightleftharpoons}} B + S\,, \tag{35}$$

for which the reaction velocity is given by

$$\tilde{\mathcal{R}}_{des} = \tilde{\kappa}_{des}\left(C_s^B - K_{des}C_b^B C_S\right), \tag{36}$$

where K_{des} is the equilibrium constant associated with the desorption-adsorption process of the isomer B.

The dynamics of the catalytic process can therefore be described by the following two sets of evolution equations for the bulk and surface concentrations. For the reactive A we have

$$\frac{\partial C_b^A}{\partial t} = \frac{1}{\mathcal{A}}\frac{\partial}{\partial x}\left[D_b\mathcal{A}\frac{\partial C_b^A}{\partial x}\right] - \tilde{\mathcal{R}}_{Ads}, \tag{37a}$$

$$\frac{\partial C_s^A}{\partial t} = \frac{1}{\mathcal{A}}\frac{\partial}{\partial x}\left[4\pi D_s\frac{\mathcal{A}}{\gamma w}\frac{\partial}{\partial x}\left(\frac{\mathcal{A}}{\gamma w}C_s^A\right)\right] + \tilde{\mathcal{R}}_{Ads} - \tilde{\mathcal{R}}_{cat}. \tag{37b}$$

The equations for the isomer B are in turn

$$\frac{\partial C_b^B}{\partial t} = \frac{1}{\mathcal{A}}\frac{\partial}{\partial x}\left[D_b\mathcal{A}\frac{\partial C_b^B}{\partial x}\right] + \tilde{\mathcal{R}}_{Des}, \tag{38a}$$

$$\frac{\partial C_s^B}{\partial t} = \frac{1}{\mathcal{A}}\frac{\partial}{\partial x}\left[4\pi D_s\frac{\mathcal{A}}{\gamma w}\frac{\partial}{\partial x}\left(\frac{\mathcal{A}}{\gamma w}C_s^B\right)\right] - \tilde{\mathcal{R}}_{Des} + \tilde{\mathcal{R}}_{cat}. \tag{38b}$$

Different predictions on the behavior of the reactive and product concentrations can be obtained depending on the slower step in the chain of processes of the heterogeneous catalysis. In Figure 7 we show the results of the catalytic model in which the distribution of active sites over the pore surface is inhomogeneous. In fact only three portions of active sites were considered with the aim to show that the concentration of molecules at the surface is inhomogeneous. Two cases were considered, with and without surface diffusion of A and B. As expected, surface diffusion helps to homogenize the distribution and enhances the total mass transport across the pore, see Ref. [31] for more details.

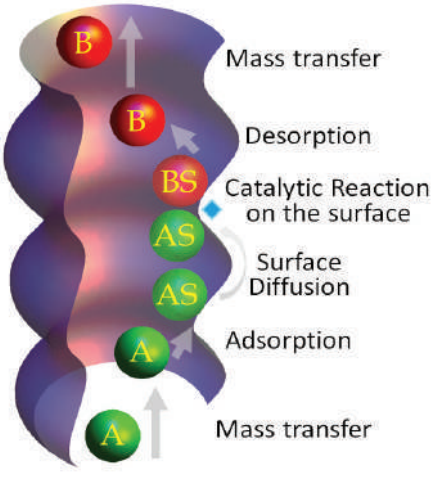

Figure 6. Illustrative image of the different steps of the heterogeneous catalysis inside an irregular pore.

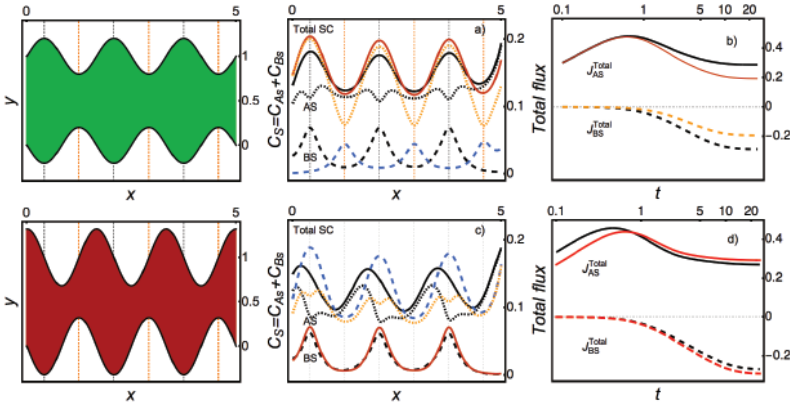

Figure 7. Numerical experiments predicting the surface concentration profiles of the species A and B of the heterogeneous isomerization reaction considered in Section 5.1. The upper line shows the *tortuous* pore together with the corresponding results Figures (**a**,**b**). In (**a**) the black lines show to the surface concentrations $C_{AS}(x)$ (dotted line) and $C_{BS}(x)$ (dashed line) together with the total concentration $C = C_{AS} + C_{BS}$ (solid line) when the active sites are located in the positions indicated by the gray gridlines (corresponding to the wider positions of the pore). The color lines correspond to the same concentrations when the active sites are located in the orange gridlines (corresponding to the narrower positions of the pore). In (**b**) the corresponding diffusion fluxes as a function of time are shown. The bottom line shows a similar situation but for the *sinuous* pore. Negative values of the flux indicate that the species B leaves the pore at the left end. In (**c**) the solid lines (black and red) show a dramatic change of total mass transport depending on the position of the active sites. This is related with the also dramatic difference of efficiency of the heterogeneous isomerization reaction in this pore, see black and blue dashed lines. The changes are also drastic with respect to the tortuous pore. The total surface fluxes of species A and B are compared in (**d**). The details of the parameters used are given in Appendix A.

6. The Effective Diffusion Coefficient of Adsorbent and Non-Adsorbent Membranes

When a fluid crosses a porous medium, the flow is reduced due to the presence of the solid material. The causes of this reduction have been traditionally split in three factors. First, the reduction of effective volume available for the fluid; second, the increase of the path-length that the molecules have to travel due to the sinuosity of the pores and finally, the third factor which is related with the decrease of the effective flux due to the corrugation of the pores.

These factors are represented by three parameters which can be measured experimentally in uptake experiments. They are, respectively, the porosity ϕ defined as the ratio between the internal and total volume of the membrane; the tortuosity τ which is the average of the square ratio of the real path-length that the molecules have to travel and the longitudinal length of the membrane; and the constriction factor δ of a membrane which quantifies the reduction of the flow due to the presence of the walls. It is an experimentally well known fact that these parameters modify the effective diffusion coefficient D_m of a membrane make up with non-adsorbent pore's surface in the form

$$\frac{D_m}{D_0} = \frac{\phi}{\tau}\delta \leq 1, \tag{39}$$

where the inequality comes from the fact that the geometric parameters obey the corresponding inequalities $\phi, \delta \leq 1$ and $\tau \geq 1$.

The present theory allows one to calculate with detail the form in which the irregularity of the pore affects the effective flux inside the porous material and, therefore, it also allows to connect it with information that can be obtained from macroscopic measurements, see Figure 8. By means of simple

conservation arguments provided in Ref. [30], it can be proved that the constriction factor of a porous material of non-adsorbent walls is given by

$$\frac{1}{\delta_{NA}} = \left\langle \frac{D_0}{D_b(z)\,\mathcal{A}(z)} \right\rangle \langle \mathcal{A}(z) \rangle. \tag{40}$$

In this expression, the brackets represent the spatial average in the longitudinal coordinate z. We have added the subscript NA to emphasize that Equation (40) is valid for non-adsorbent membranes. Therefore, the constriction factor in Equation (40) together with the porosity and tortuosity, having their corresponding expressions in Ref. [30], help to predict the diminution of the flow in a non-adsorbent porous material. This expression is a general form of a previous expression intuitively obtained for the diffusivity in Ref. [48].

Adsorbent Membranes

In most of the practical cases, however, one is interested on membranes able to carry out adsorption–desorption processes. The interesting question now is to determine in which cases the effective membrane diffusion coefficient D_m increases and in which decreases. The question is not obvious to solve a priori since an enhancement of the bulk diffusion may occur by the presence of surface diffusion effects, and the fact that the adsorption along the pore can increase the local concentration gradient inside the pore, accelerating the entrance of more fluid to the pore.

In order to consider the influence that the adsorption process and the irregularity of the geometry have in the measured diffusivity, one has to consider the total change in the two flows inside the channel: The flow due to bulk diffusion and which is originated by the external concentration gradient $J_b = -D_b \frac{\partial C_b}{\partial x}$, and the flow due to surface diffusion that is owing to the internal variations of concentration in the adsorbed layer $J_s = -\frac{4D_s}{\gamma w} \frac{\partial}{\partial x} \left(\frac{wC_s}{\gamma} \right)$. In mathematical terms, the reduced scheme we have used in Equations (16) and (29) allows to show that the total flow per unit of area is

$$J_t = -D_b \frac{\partial C_b}{\partial x} - \frac{4D_s}{\gamma w} \frac{\partial}{\partial x} \left(\frac{wC_s}{\gamma} \right). \tag{41}$$

As the total flow can be written macroscopically only on terms of an effective diffusion coefficient D_t, and the total concentration $C_t = C_b + C_s$ as $J_t = -D_t(x) \frac{\partial C_t}{\partial x}$, simple comparison of this equation with Equation (41) allows to obtain D_t if the isotherm of the system $C_s(C_b)$ is known. In this case and if the adsorption/desorption process is the rate limiting step in the catalytic reaction, it is possible to calculate the rate conversion factor $\lambda = \frac{\partial C_s}{\partial C_b}$. With this information, the local effective diffusivity of the particles inside a pore of adsorbent walls is [18]

$$D_t(x) = D_b(x) \frac{1}{1+\lambda(x)} + \frac{4D_s(x)}{\gamma^2(x)} \frac{\lambda(x)}{1+\lambda(x)}. \tag{42}$$

Since $\lambda > 0$ for most of the known isotherms, the last equation establishes that the effective diffusivity of the fluid inside the pore is proportional to the bulk and surface diffusion coefficients D_b and D_s, and it can be enhanced or diminished depending on the intensity of the adsorption rate $\lambda(C_s, C_b)$. There are two facts that Equation (42) confirms: first, the effective diffusivity of particles depends upon the position along the pore; secondly, the diffusivity depends upon the internal concentration of bulk and adsorbed particles. More importantly, this internal diffusivity can be predicted if D_0 and D_s are known in the limit of zero loading.

In these terms, the conservation principles used for obtaining the constriction factor δ in Equation (40) for a non-adsorbent membrane, can be easily generalized for an adsorbent one, and the more general expression for this parameter is just:

$$\frac{1}{\delta} = \left\langle \frac{D_0}{D_t(z)\,A(z)} \right\rangle \langle A(z) \rangle. \tag{43}$$

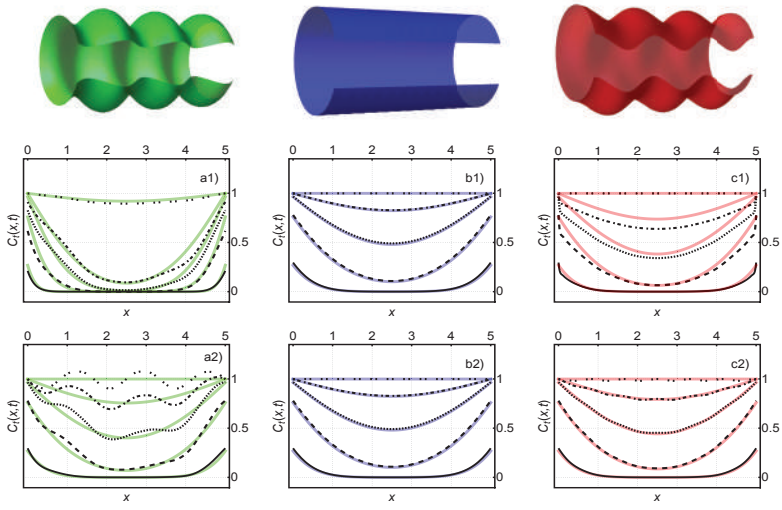

Figure 8. Concentration profiles in three pores depicted above, where an homogeneous adsorption process takes place along the pore with equal concentrations at both ends. In (**a1**) we show the predictions of the concentration profiles for a tortuous pore (green) when adsorption and bulk diffusion takes place at different times. Black lines show the predictions by Equations (16) and (29) whereas solid color lines (green) show the prediction by the most elemental one-dimensional diffusion Equation (12) having no-corrections from the geometry of the pore. In (**a2**) we show a similar comparison in the presence of surface diffusion. The comparisons in (**b1**,**b2**) correspond to the cylindrical pore (blue) and show that, only in this case, the approaches are equivalent, as expected. Comparisons in (**c1**,**c2**) correspond to the winding pore (red). Remarkable differences between tortuous and winding pores emerge from this simulation study, in particular in the case when surface diffusion is present. Cylindrical and tortuous pores have very similar behavior whereas the tortuous pore introduces large deviations with respecto to the elemental description of the concentration profile. See Appendix A for details of the parameters used in the simulations.

This constriction factor in the effective diffusion coefficient of a membrane in Equation (39), depends on the concentration of the adsorbed phase and therefore, it depends on the loading. This means that if the curves D_m versus loading θ are known, one can establish the relative importance of the surface diffusion and the irregularity of the pore in the efficiency of the adsorption process [18]. Since our reduced model in Equations (16) and (29) allows to obtain with detail the internal concentration, it enables to establish how these curves change in terms of the corrugation of the pore and in terms of the intensity of the surface diffusion, this will be illustrated in the following section.

7. How to Use This Theory in Uptake Experiments

In previous sections we have shown how the speed and efficiency of the mass transport process through a membrane are related to the shape of the pores which make up the membrane. If the shape of the pores is known, then by using the average transport equations Equations (16) and (29) it is possible to predict with a good degree of approximation, the amount and distribution of the material adsorbed as well as its concentration in the bulk.

Nonetheless, most practical situations impose the inverse problem, that is, the necessity of finding out some general qualitative characteristics of the pores of a material from, for instance, uptake experiments. Without pretending to be exhaustive in this issue, in the present section we will illustrate how this structural or geometrical information can be extracted from experiments by fitting the

obtained data with the numerical solution of the Equations (16) and (29). In order to do this, we will consider two examples.

7.1. Breakthrough Curve and Internal Pore Geometry

As a first example, consider the experiment of a fluid adsorbed on a column of a porous material in which the pores have, approximately, the same geometric shape and an homogeneous distribution of adsorption sites. In this experiment a fluid penetrates the column from one side and diffuses towards the exit side. If the fluid is partially adsorbed at the surface of the pores, then the rapidity with which the bulk concentration at a certain height of the column reaches its saturation value may be different depending on the shape of the pores. This follows from the fact that the effective diffusivity of the membrane depends on the balance between the bulk and the surface concentrations. These concentrations are implicit functions of the adsorption velocity inside the column which, in turn, is partially determined by the geometry of the pores and the distribution of the active sites.

The process already described can be understood with the help of a breakthrough curve, in which the concentration at a certain point is measured as a function of time. The important data are the initial time, at which the increase in concentration begins, and the slope of the curve which is critically determined by the balance between the characteristic times associated with the volumetric diffusion and the reaction of adsorption.

Figure 9 shows the numerical solution of Equation (16) for a simple adsorption process at the surface of the pore. Each curve represents the same diffusion-adsorption dynamics for a winding (black lines) and a tortuous (color lines) pores, see details in the caption of the figure and in Appendix A. A significative difference among the breakthrough curves of materials having straight (or near straight) pores is clear, when compared with those emerging from membranes in which the pores have important constrictions or sinuosities. Therefore, small changes on the geometry can be detected in principle in these experiments.

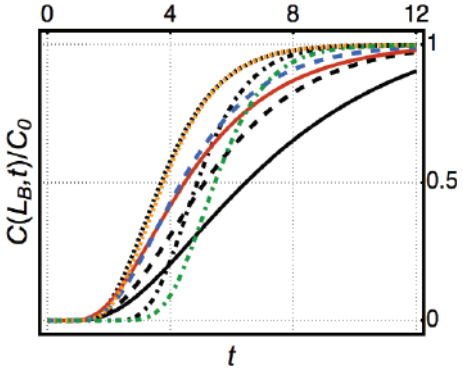

Figure 9. Breakthrough curves obtained from solving Equation (16) for a simple linear adsorption process given by $\dot{\rho} = -r_a C_b(z)$ with r_a the adsorption rate and D_0 the diffusion coefficient. The pores considered are the winding (black lines) and tortuous (colour lines) pores with length $L = 5$. The boundary conditions consist of fluid entering at the left ($C_b(z = 0) = 1$), and exiting at the right ($C_b(z = L) = 0$). The values of the constants (in arbitrary units) were $r_a = 0$ and $D_0 = 1$ for the solid lines, $r_a = 0.1$ and $D_0 = 0.75$ for the dashed lines, $r_a = 0.4$ and $D_0 = 0.5$ for the dotted lines, and $r_a = 1.0$ and $D_0 = 0.1$ for the dash-dotted lines. In order to obtain the breakthrough curve, the temporal increasing of the concentration is measured at $z = 4.5$. Our theory predicts that a small difference on the slope of these curves can be the result of purely geometrical changes, and the constriction and sinuosity of the pores can be reflected in this type of curves. See Appendix A [16].

7.2. Effective Diffusivity of the Membrane as a Function of the Average Load

The second example consists on a similar experiment with a porous column. However, in this case we will consider the possibility of modifying the chemical properties of the surface of the pore by some procedure without essentially changing its internal geometry. Depending on the active materials added to the surface of the pores in the membrane, the density and distribution of active sites of adsorption will be increased or reduced, thus changing the average load that the column can adsorb.

In this experiment it should be possible to measure the time evolution of the spatial profiles of the *total* concentration ($C_t = C_b + C_s$) inside the membrane, as recent experiments in pulsed field gradient NMR techniques have shown [34,49,50]. The resulting curves, such as those reported in Ref. [51] may be reproduced with our theory as it follows from Figure 8.

Furthermore, since the spatial profile of the *total* concentration is related with the effective diffusion coefficient of the membrane, then by changing the properties of the surface it is possible to change the relationship between the effective diffusion coefficient of the membrane and the average adsorbed load. Thus, from independent measurements it should be possible to establish the dependence of the effective diffusion of the membrane in terms of the average adsorbed load.

The same can be done by using as an starting point the Equations (16) and (29). These equations can be solved in order to find the *total* mass concentration within the pore as a function of position and time. Then, by using the parameter $\lambda = (\partial C_s/\partial C_b)_T$ as well as Equations (41) through (43), it is possible to find the effective diffusion coefficient associated with the *total* mass concentration, i.e., the effective diffusion coefficient of the membrane, D_m. The Figure 10 shows the predictions for these experiments, that is, the value of the effective diffusion coefficient as a function of the spatially averaged load $\langle \Theta(x) \rangle_x$. Each frame in the figure represents an experiment with three different columns, corresponding to pores having different geometries and the same fixed value of the surface diffusivity. Each point of the curve represents a different value of the adsorption rate which reflects the changes in the number of active sites within the membrane and therefore, a different load capacity.

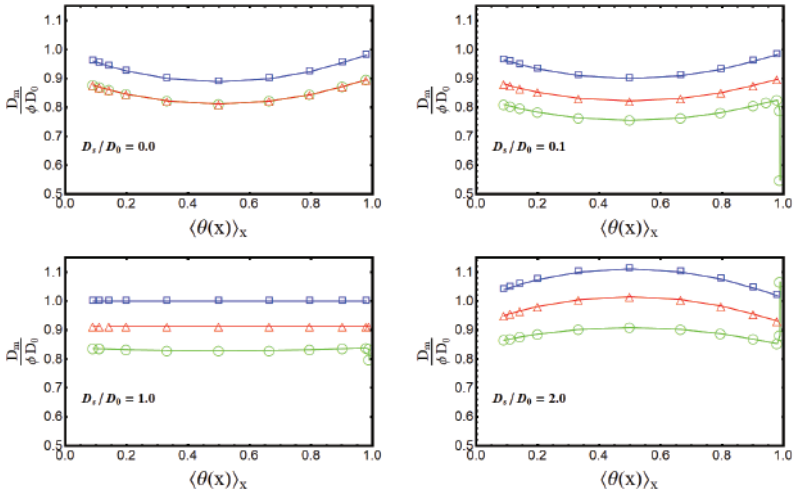

Figure 10. Effective diffusion coefficient of a membrane as a function of the loading for the three pores studied, and for several values of the surface diffusion coefficient. It is clear that the surface diffusion changes the concavity of the curve and, at fixed loading, increases the efficiency of the mass transport. See Appendix A for simulation details.

The Figure 10 provides some qualitative consequences about the relationship between the shape of the pores and the surface diffusion. From the figure, it follows that the surface diffusion increases

the net effective diffusivity of the particles relative to the state where the particles cannot move along the surface. Since this seems to happen especially for intermediate or high loads, a change in the concavity of the curve may be related to a change in the surface diffusion of the process. For high surface diffusivities and loads, adsorbed particles slow down the total diffusion due to their mutual interactions. The other mechanism associated with the change of the shape of these curves is directly related with the shape of the pore. Sinuous and tortuous pores tend to reduce the effective diffusion coefficient with respect to a straight cylindrical pore, as expected. An important consequence of this effect is that, although both irregular pores have the same effective volumetric diffusion coefficient, since one pore has less surface area than the other, it has a lower effective diffusion coefficient.

As concluding remarks of this section, we want to emphasize that from these two examples, and their multiple variants, it is possible to infer that although it is not entirely possible to predict the shape of the pores or the value of the surface diffusion coefficient solely from the results of the averaged equations, it is possible to establish some general and qualitative characteristics about the internal structure of the pores making up the membrane. It goes without saying that a systematic study on this problem will be extremely interesting, and that our theory provides with a theoretical tool to solve it.

8. Summary and Conclusions

Porous materials are of paramount importance nowadays, because the narrowness of the empty space inside them and its enormous internal surface. These two characteristics make them very attractive for a wide range of applications, ranging from drug delivery to oil refination and the elaboration of proton exchange membranes. Their effectiveness is based on having very fine pores that control the diffusion, and thereby amplify the speed of the chemical adsorption and conversion that occur within it. Due to this relevant role, it is therefore crucial to understand how all these processes depend on the geometry of the pores.

In this work, we generalized previous studies on the single dimensional description of the diffusive mass transport across two dimensional pores [16,18,21,30,31] to a three-dimensional case with axial symmetry. The key idea is that, on averaging the three-dimensional mass balance equation along the transport direction, one obtains two single-dimensional mass conservation equations, for volumetric bulk and surface concentrations, providing with a sound theoretical basis in order to describe how bulk and surface diffusion are affected by adsorption and desorption processes, as well as by catalytic conversion within the space defined by the irregular geometry of the pores of the material. In this aspect, the theory represents a powerful generalization of the Shaphiro–Brenners's theory for macrotransport processes, which was formulated for regular domains and was restricted to low concentrations. Our theoretical framework constitutes therefore a bridge between the microscopic detail of the pore and the macroscopic measurements of the experiment, a versatility that will allow in the future to contribute to the design of porous materials such as membranes with specifically optimized physical-chemical properties.

Beside the virtues already mentioned and as far as we know, the present work constitutes the *first analytical approach* to the study of surface diffusion in irregular porous media. The tremendous generality of the pair of equations we have derived, Equations (16) and (29), allows to establish the analytical expression of two coefficients widely used in the industry to determine the efficiency of chemical reactors, namely, the mass transfer coefficient and the effectiveness factor, both of them depending on the constriction and tortuosity of the pore. The relationships that we have established between the geometry and these macroscopic parameters, are given through the generalized Thiele modulus of a porous medium, as well as its relation, at the pore scale, with the effective diffusion coefficient of a membrane, a quantity measurable in experiments. These parameters may be used to quantify the efficiency of artificial and structured porous media, as well as in porous materials such as some zeolites.

Additionally, we have explained for the first time how surface diffusion increases the effectiveness of catalysis. In practice, our study predicts how to design artificial nano-membranes based on conical pores that optimize sieving, transfer and catalytic conversion. This allows to adjust the design of the membrane in function of the results that the industrial applications require, which is of capital importance nowadays, especially when the perspective on membrane 3D printing is emerging as a very promising fabrication technique [32].

The theory we have postulated can be used as a tool for modeling the distribution and diffusivity of particles in the bulk and on the surface of irregular pores, when the processes involved in heterogeneous chemistry take place simultaneously. Therefore, Equations (16) and (29) constitute a very powerful theoretical framework in the description of chemical reactors formed by membranes, where all these processes occur simultaneously in the conversion of reactants into products through a catalytic reaction on the surface.

The great advantage of using our theoretical framework is that the microscopic quantities that refer to the internal detail of the flow, and the interactions within the irregular pore, can be translated into macroscopic variables that are currently measured in experiments. This makes it of huge practical importance.

Author Contributions: Conceptualization, I.S.-H. and A.L.-D.; mathematical analysis and simulations I.S.-H., S.I.H., C.G.-A. and A.L.-D.; investigation I.S.-H., S.I.H., C.G.-A. and A.L.-D.; writing—review and editing, I.S.-H., S.I.H., C.G.-A. and A.L.-D.; project administration, S.I.H.; funding acquisition, I.S.-H. and S.I.H.

Funding: This research was funded by UNAM-DGAPA grant numbers PAPIIT IN116617, IN117419, IA104319 and LANCAD-UNAM-DGTIC-276.

Conflicts of Interest: The authors declare no conflict of interest.

Appendix A

Appendix A.1 Figure 1

In order to simplify the description, in these work we have studied pores which can be reduced to the well known two-dimensional case, whose three-dimensional equivalents are plotted in Figure 1 [21]. A two dimensional pore is constructed by two walls $w_1(z)$ and $w_2(z)$. In this case, the width and the middle line are given by $w(x) = w_2(z) - w_1(z)$ and $h(z) = [w_1(z) + w_1(z)]/2$, respectively. The effective bulk diffusion coefficient is then given by the generalized Bradley-Zwanzig [23] diffusion coefficient equivalent to Equation (15) in two dimensions:

$$D(z) = \frac{D_0}{1 + h_z^2(z) + \frac{w_z^2(z)}{12}}. \tag{A1}$$

The four pores of length $L = 5$ plotted are obtained with the data of Table A1.

Table A1. Values of the parameters used to build the four pores used in the main text.

Label	$w_1(z)$	$w_2(z)$
Tortuous	$0.2 \sin\left(\frac{6\pi z}{L}\right)$	$1 - 0.2 \sin\left(\frac{6\pi z}{L}\right)$
Winding	$-0.2 \sin\left(\frac{6\pi z}{L}\right)$	$1 - 0.2 \sin\left(\frac{6\pi z}{L}\right)$
Straight	0	1
Conical	$-m\,z$	$1 + m\,z$

In the plotted example in Figure 1, $m = 0.1$.

Appendix A.2 Figure 2

Comparison of the concentration profiles inside two different pores for pure diffusion (left) and diffusion-adsorption (right) processes. The concentration for the tortuous (black lines) and winding (color lines) pores which have the same effective diffusion coefficient $D_b(z) = \frac{D_0}{1+0.19\cos^2\left(\frac{6\pi z}{5}\right)}$, have been plotted for four different times (continuous line $t = 0.0$, dotted line $t = 5.0$, dot-dashed line $t = 10.0$, dashed line $t = 50.0$). Left: In a first process, only bulk diffusion in the two pores is taken into account. We solved Equation (16) with $D_0 = 1$ and $\dot{\rho} = 0$. We plot the concentration as function of time considering that $C_b(z = 0) = 1$ and $C_b(z = L) = 0$. As expected, the pure bulk diffusive dynamics is essentially the same in both pores. Right: In a second process, an adsorption reaction in the surface with rate $\dot{\rho} = -0.05$ is now included. In this case, the difference of the enhancement factor ($\overline{\gamma} = 1.3$) of the tortuous pore makes the adsorption process more effective than the winding one ($\overline{\gamma} = 1.05$). This is confirmed by the fact that less concentration of particles reaches the exit side of the pore in the winding geometry [21].

Appendix A.3 Figure 3

The mass transfer coefficient k is the proportionality constant between the flux at the entry and the difference of concentration between the two ends of the pore [14]. Therefore, we solve Equation (16) for the mentioned geometries with the boundary conditions $C(z = 0) = C_0 = 1$ and $C(z = L) = 0$ at the ends of the pore, and $J(z = 0) = k(C_0 - 0)$. The reference value $k_0 = D_0/L$ is obtained when there is no adsorption, and the pore is straight. In contrast, the effectiveness factor η is the ratio between the amount of mass entering the pore, compared with the mass that would be adsorbed if the entire pore were exposed to the external concentration ($C_0 = 1$).

In both cases, analytic expressions can be obtained from the reduction scheme for conical pores [16] changing the rate of the liner adsorption in Equation (16) as $\dot{\rho} = -\kappa C_b(z, t)$. The four pores can be obtained with $R(z) = 1 + mz$, with $m = 0.5$ (red), 0.2 (orange), 0 (green) and -0.2 (blue), respectively. The length of these pores is $L = 2$.

Appendix A.4 Figure 5

Langmuir adsorption dynamics inside the tortuous (black lines) and winding (color lines) pores in the presence of surface diffusion was calculated by solving Equations (37) with $D_0 = 1$, $D_s = 0.1$ and the Langmuir reaction in Equation (32) with $\tilde{\kappa}_{ads} = 1$ and $K_{ads} = 0.3$. In this case $\mathcal{R}_{cat} = 0$ and we use periodic boundary conditions.

The solid lines in Figure 5a,b show the long-time (equilibrium) bulk concentration $C_b(x)$ and diffusion current $J_b(x)$, respectively. In the same figures, the dashed-lines show the long-time (equilibrium) surface concentration $C_s(x)$ and diffusion current $J_s(x)$. The dotted-lines in Figure 5a,b represent the long-time (equilibrium) total concentration $C_t = C_b + C_s$ and current $J_t = J_b + J_s$. Black lines correspond to the tortuous pore, color lines to the winding pore. In Figure 5c we show the coverage fraction $\theta = C_s/C_s^0$, with $C_s^0 = 1$ for the tortuous (black lines) and the winding (red lines) pores.

The adsorbed particles tend to segregate producing an accumulation in the wider regions of the pore. As it can be seen, the different diffusivities in the bulk and in the surface particles can generate internal fluxes inside the pore, since surface and bulk particles tend to move to the narrower and wider parts of the pore, respectively. As it is expected, this effect is more visible in the tortuous pore than in the winding one, where both concentrations are nearly homogeneous [31].

Appendix A.5 Figure 7

Evaluation of the heterogeneous catalysis process described in Equations (37) and (38) for the tortuous (upper row) and sinuous (bottom row) pores with flow of A entering by the left to the pore [$C_b^A(z = 0) = 1, C_b^A(z = L) = 0$], null concentration of B at the exterior [$C_b^B(z = 0) = C_b^B(z = L) = 0$],

and no surface concentration of B or A [$C_s^A(z=0) = C_s^A(z=L) = C_s^B(z=0) = C_s^B(z=L) = 0$]. The bulk and diffusion coefficients are $D_0 = 1$ and $D_s = 0.1$. The coefficients of the different reactions in Equations (32) , (34) and (36) are $\tilde{\kappa}_{ads} = \tilde{\kappa}_{cat} = \tilde{\kappa}_{des} = 1$, $K_{ads} = K_{des} = 0.3$, and $K_{cat} = 0.3$. The position of the active sites in the reduced scheme is controlled by the function $f(z)$ which is zero almost everywhere, except in the points z_i indicated by the dashed lines in the Figure. The comparison is done among the active sites at the gray gridlines located at: $\{z_i\} = \{\frac{5}{12}, \frac{25}{12}, \frac{15}{4}\}$ (black lines), and those located at the orange gridlines defined by: $\{z_i\} = \{\frac{5}{4}, \frac{35}{12}, \frac{55}{12}\}$.

The pore and the respective position of the active sites is given in the first row of this figure. Figure 7a (tortuous) and c (sinuous) show the surface steady-state concentrations of A, B [AS (dotted lines) and BS (dashed lines)] as well as the total one concentration obtained in each case [SC (solid lines)]. It is confirmed the increase of particles B near the active sites of catalysis. The Figure 7b (tortuous) and d (sinuous) show the flux of A (in bulk and surface entering the pore), and the flux of B exiting the pore. From this model study it follows that the active sites near the throats (orange grid lines) increase the conversion process in the tortuous pore, since more particles of A are being converted into B [31]. Surface flow behavior is more sensitive on the position of the active sites for the tortuous pore than for the sinuous one.

Appendix A.6 Figure 8

We simulate the diffusion and adsorption processes given by Equations (37), with a Langmuir adsorption in Equation (32) in the winding, straight and tortuous pores depicted below. In each case, the different lines correspond to different times, showing the filling process with boundary conditions $C_t(z=0) = C_t(z=L) = 1$. The dashed lines depict the internal concentration by using the microscopic approach, provided by the reduced model we present in Equations (16) and (29). The parameters used were $D_0 = 1$, $\tilde{\kappa}_{ads} = 0.1$, $K_{ads} = 1$. In the upper row $D_s = 0$, and in the bottom one $D_s = 1$. The solid lines represent the macroscopic approach as the result of using the most elemental one dimensional diffusion Equation (12) with the same boundary conditions, and using the effective diffusion coefficient D_m as predicted by Equation (39) in Ref. [18]. As it can bee seen, the results derived from all the microscopical details are well captured by the macroscopic diffusion coefficient.

Appendix A.7 Figure 9

Breakthrough curves obtained from solving Equation (16) for a simple linear adsorption process given by $\dot{\rho} = -r_a C_b(z)$ with r_a the adsorption rate and D_0 the diffusion coefficient. The pores considered are the winding (black lines) and tortuous (colour lines) pores with length $L = 5$. The boundary conditions consist of fluid entering at the left ($C_b(z=0) = 1$), and exiting at the right ($C_b(z=L) = 0$). The values of the constants (in arbitrary units) were $r_a = 0$ and $D_0 = 1$ for the solid lines, $r_a = 0.1$ and $D_0 = 0.75$ for the dashed lines, $r_a = 0.4$ and $D_0 = 0.5$ for the dotted lines, and $r_a = 1.0$ and $D_0 = 0.1$ for the dash-dotted lines. In order to obtain the breakthrough curve, the temporal increasing of the concentration is measured at $z = 4.5$. Our theory predicts that a small difference on the slope of these curves can be the result of purely geometrical changes, and the constriction and sinuosity of the pores can be reflected in this type of curves. [16].

Appendix A.8 Figure 10

Curves measuring the effective diffusion coefficient D_m as a function of the loading. Each point in these plots corresponds to the solution of Equations (37), for the geometry and surface diffusion coefficient indicated. The fixed parameters are $D_0 = 1$ and $\tilde{\kappa}_{ads} = 0.1$. For the horizontal axis, the changes in the average loading $\langle \theta(X) \rangle_X$ are obtained by averaging the surface concentration along the domain. Each point corresponds to a different value of K_{ads} which modifies the adsorption process and the amount of particles attached to the surface. For the vertical axis, the changes in K_{ads} modify the ratio of adsorption λ, changing the effective diffusion coefficient in the local scale in Equation (42)

and, therefore modifying D_m / D_0 in Equation (40). For the represented case, the rate K_{ads} was varied between 0.01 and 1 approximately.

As it is expected, the tortuous geometry decreases the effective diffusion coefficient respect to the straight pore, whereas the winding pore constitutes a middle case. Be aware how the surface diffusion augments the transport properties of the pore. Therefore, our theoretical framework allows us to estimate some qualitative aspects of a membrane, when taking as reference one with straight pores [18].

References

1. Taylor, G.I. Dispersion of soluble matter in solvent flowing slowly through a tube. *Proc. R. Soc. Lond. Ser. A Math. Phys. Sci.* **1953**, *219*, 186–203.
2. Aris, R. On the dispersion of a solute in a fluid flowing through a tube. *Proc. R. Soc. Lond. Ser. A Math. Phys. Sci.* **1956**, *235*, 67–77.
3. Brenner, H. *Macrotransport Processess*; Butterworth-Heinemann: Boston, MA, USA, 1993.
4. Ibrahim, H.; Hassan, H.; Mekhamer, H.; Kenawy, S. Diffusion and sorption of Cs+ and Sr 2+ ions onto synthetic mullite powder. *J. Radioanal. Nucl. Chem.* **2018**, *319*, 1–12. [CrossRef]
5. Millhauser, G.L.; Salpeter, E.E.; Oswald, R.E. Diffusion models of ion-channel gating and the origin of power-law distributions from single-channel recording. *Proc. Natl. Acad. Sci. USA* **1988**, *85*, 1503–1507. [CrossRef]
6. Wijmans, J.; Baker, R. The solution-diffusion model: A Review. *J. Membr. Sci.* **1995**, *107*, 1–21. [CrossRef]
7. Yan, C.; Liu, J.; Liu, F.; Wu, J.; Gao, K.; Xue, D. Tube formation in nanoscale materials. *Nanoscale Res. Lett.* **2008**, *3*, 473–480, doi:10.1007/s11671-008-9193-6. [CrossRef]
8. Martínez-Balbuena, L.; Hernández-Zapata, E.; Santamaría-Holek, I. Onsager irreversible thermodynamics of the dynamics of transient pores in spherical lipid vesicles. *Eur. Biophys. J.* **2015**, *44*, 473–481. [CrossRef]
9. Wu, R.; Liao, Q.; Zhu, X.; Wang, H. Pore network modeling of cathode catalyst layer of proton exchange membrane fuel cell. *Int. J. Hydrog. Energy* **2012**, *37*, 11255–11267. [CrossRef]
10. Stavarek, P.; Vajglova, Z.; Kristal, J.; Jiricny, V.; Kolena, J. Self-sustained oscillations of temperature and conversion in a packed bed microreactor during 2-methylpropene (isobutene) hydrogenation. *Catal. Today* **2015**, *256*, 250–260. [CrossRef]
11. Adler, P. *Porous Media: Geometry and Transports*; Elsevier: Amsterdam, The Netherlands, 2013.
12. Otero, J.A.; Mazarrasa, O.; Villasante, J.; Silva, V.; Prádanos, P.; Calvo, J.I.; Hernández, A. Three independent ways to obtain information on pore size distributions of nanofiltration membranes. *J. Membr. Sci.* **2008**, *309*, 17–27. [CrossRef]
13. Carberry, J.J.; Varma, A. *Chemical Reaction and Reactor Engineering*; CRC Press: Dover, NY, USA, 2001.
14. Fogler, H.S. *Elements of Chemical Reaction Engineering*; Prentice-Hall International: London, UK, 1999.
15. Glavatskiy, K.S.; Bhatia, S.K. Effect of pore size on the interfacial resistance of a porous membrane. *J. Membr. Sci.* **2017**, *524*, 738–745. [CrossRef]
16. Ledesma-Durán, A.; Hernández Hernández, S.I.; Santamaría-Holek, I. Effectiveness Factor and Mass Transfer Coefficient in Wedge and Funnel Pores Using a Generalized Fick–Jacobs Model. *J. Phys. Chem. C* **2016**, *120*, 29153–29161. [CrossRef]
17. Seetha, S.; Manickam, J.G.; McCutcheon, J.R. Pore structure characterization of asymmetric membranes: Non–destructive characterization of porosity and tortuosity. *J. Membr. Sci.* **2014**, *454*, 549–554.
18. Ledesma-Durán, A.; Hernández, S.I.; Santamaría-Holek, I. Effect of Surface Diffusion on Adsorption–Desorption and Catalytic Kinetics in Irregular Pores. II. Macro-Kinetics. *J. Phys. Chem. C* **2017**, *121*, 14557–14565. [CrossRef]
19. Chandler, M.; Zydney, A. Effects of membrane pore geometry on fouling behavior during yeast cell microfiltration. *J. Membr. Sci.* **2006**, *285*, 334–342. [CrossRef]
20. Kanani, D.M.; Fissell, W.H.; Roy, S.; Dubnisheva, A.; Fleischman, A.; Zydney, A.L. Permeability–selectivity analysis for ultrafiltration: Effect of pore geometry. *J. Membr. Sci.* **2010**, *349*, 405–410. [CrossRef]
21. Ledesma-Durán, A.; Hernández-Hernández, S.I.; Santamaría-Holek, I. Generalized Fick–Jacobs Approach for Describing Adsorption–Desorption Kinetics in Irregular Pores under Nonequilibrium Conditions. *J. Phys. Chem. C* **2016**, *120*, 7810–7821. [CrossRef]
22. Zwanzig, R. Diffusion past an entropy barrier. *J. Chem. Phys.* **1992**, *96*, 3926–3930. [CrossRef]

23. Bradley, R.M. Diffusion in a two-dimensional channel with curved midline and varying width: Reduction to an effective one-dimensional description. *Phys. Rev. E* **2009**, *80*, 061142. [CrossRef]
24. Pineda, I.; Alvarez-Ramirez, J.; Dagdug, L. Diffusion in two-dimensional conical varying width channels: Comparison of analytical and numerical results. *J. Chem. Phys.* **2012**, *137*, 174103. [CrossRef]
25. Berezhkovskii, A.; Pustovoit, M.; Bezrukov, S. Diffusion in a tube of varying cross section: Numerical study of reduction to effective one-dimensional description. *J. Chem. Phys.* **2007**, *126*, 134706. [CrossRef] [PubMed]
26. Santamaría-Holek, I.; Grzywna, Z.J.; Miguel Rubi, J. A non-equilibrium thermodynamic model for combined adsorption and diffusion processes in micro-and nanopores. *J. Non-Equilib. Thermodyn.* **2012**, *37*, 273–290. [CrossRef]
27. Santamaría-Holek, I.; Grzywna, Z.; Rubi, J. Entropic effects in diffusion-adsorption processes in micropores. *Eur. Phys. J. Spec. Top.* **2013**, *222*, 129–141. [CrossRef]
28. Rubi, J.; Reguera, D. Thermodynamics and stochastic dynamics of transport in confined media. *Chem. Phys.* **2010**, *375*, 518–522. [CrossRef]
29. Reguera, D.; Rubi, J. Kinetic equations for diffusion in the presence of entropic barriers. *Phys. Rev. E* **2001**, *64*, 061106. [CrossRef]
30. Ledesma-Durán, A.; Hernández, S.; Santamaría-Holek, I. Relation between the porosity and tortuosity of a membrane formed by disconnected irregular pores and the spatial diffusion coefficient of the Fick-Jacobs model. *Phys. Rev. E* **2017**, *95*, 052804. [CrossRef] [PubMed]
31. Ledesma-Durán, A.; Hernández, S.; Santamaría-Holek, I. Effect of Surface Diffusion on Adsorption–Desorption and Catalytic Kinetics in Irregular Pores. I. Local Kinetics. *J. Phys. Chem. C* **2017**, *121*, 14544–14556. [CrossRef]
32. Low, Z.X.; Chua, Y.T.; Ray, B.M.; Mattia, D.; Metcalfe, I.S.; Patterson, D.A. Perspective on 3D printing of separation membranes and comparison to crossmark related unconventional fabrication techniques. *J. Membr. Sci.* **2017**, *523*, 596–613. [CrossRef]
33. Kondepudi, D.; Prigogine, I. *Modern Thermodynamics: From Heat Engines to Dissipative Structures*; John Wiley and Sons: Hoboken, NJ, USA, 2014.
34. Kärger, J.; Ruthven, D. *Diffusion in Zeolites and other Microporous Solids*; J. Wiley and Sons Inc.: New York, NY, USA, 1992; p. 341.
35. Pineda, I.; Dagdug, L. Projection of two-dimensional diffusion in narrow asymmetric channels onto the longitudinal direction. *J. Chem. Phys.* **2014**, *1579*, 121–129.
36. Berezhkovskii, A.; Szabo, A. Time scale separation leads to position–dependent diffusion along a slow coordinate. *J. Chem. Phys.* **2011**, *135*, 074108. [CrossRef]
37. Ho, C.; Qiao, R.; Heng, J.B.; Chatterjee, A.; Timp, R.J.; Aluru, N.R.; Timp, G. Electrolytic transport through a synthetic nanometer-diameter pore. *Proc. Natl. Acad. Sci. USA* **2005**, *102*, 10445–10450. [CrossRef] [PubMed]
38. Mistura, G.; Pozzato, A.; Grenci, G.; Bruschi, L.; Tormen, M. Continuous adsorption in highly ordered porous matrices made by nanolithography. *Nat. Commun.* **2013**, *4*, 2966. [CrossRef] [PubMed]
39. Yameen, B.; Ali, M.; Neumann, R.; Ensinger, W.; Knoll, W.; Azzaroni, O. Single conical nanopores displaying pH-tunable rectifying characteristics. Manipulating ionic transport with zwitterionic polymer brushes. *J. Am. Chem. Soc.* **2009**, *131*, 2070–2071. [CrossRef] [PubMed]
40. Yamauchi, Y.; Nagaura, T.; Ishikawa, A.; Chikyow, T.; Inoue, S. Evolution of standing mesochannels on porous anodic alumina substrates with designed conical holes. *J. Am. Chem. Soc.* **2008**, *130*, 10165–10170. [CrossRef] [PubMed]
41. Siwy, Z.; Heins, E.; Harrell, C.C.; Kohli, P.; Martin, C.R. Conical-nanotube ion-current rectifiers: The role of surface charge. *J. Am. Chem. Soc.* **2004**, *126*, 10850–10851. [CrossRef]
42. Siódmiak, J.; Santamaría-Holek, I.; Gadomski, A. On morphological selection rule of noisy character applied to model (dis) orderly protein formations. *J. Chem. Phys.* **2010**, *132*, 05B608. [CrossRef]
43. Miyabe, K.; Guiochon, G. Measurement of the parameters of the mass transfer kinetics in high performance liquid chromatography. *J. Sep. Sci.* **2003**, *26*, 155–173. [CrossRef]
44. Miyabe, K.; Guiochon, G. Fundamental interpretation of the peak profiles in linear reversed-phase liquid chromatography. *Adv. Chromatogr.* **2000**, *40*, 1–113.
45. Miyabe, K.; Guiochon, G. Surface diffusion in reversed-phase liquid chromatography. *J. Chromatogr. A* **2010**, *1217*, 1713–1734. [CrossRef]

46. Medveď, I.; Černý, R. Surface diffusion in porous media: A critical review. *Microporous Mesoporous Mater.* **2011**, *142*, 405–422. [CrossRef]
47. Langmuir, I. The adsorption of gases on plane surfaces of glass, mica and platinum. *J. Am. Chem. Soc.* **1918**, *40*, 1361–1403. [CrossRef]
48. Festa, R.; d'Agliano, E.G. Diffusion coefficient for a Brownian particle in a periodic field of force: I. Large friction limit. *Phys. A Stat. Mech. Appl.* **1978**, *90*, 229–244. [CrossRef]
49. Kärger, J.; Kortunov, P.; Vasenkov, S.; Heinke, L.; Shah, D.B.; Rakoczy, R.A.; Traa, Y.; Weitkamp, J. Unprecedented insight into diffusion by monitoring the concentration of guest molecules in nanoporous host materials. *Angew. Chem. Int. Edit.* **2006**, *45*, 7846–7849. [CrossRef] [PubMed]
50. Kärger, J.; Binder, T.; Chmelik, C.; Hibbe, F.; Krautscheid, H.; Krishna, R.; Weitkamp, J. Microimaging of transient guest profiles to monitor mass transfer in nanoporous materials. *Nat. Mater.* **2014**, *13*, 333–343. [CrossRef] [PubMed]
51. Kärger, J.; Ruthven, D.M.; Theodorou, D.N. *Diffusion in Nanoporous Materials*; John Wiley & Sons: Hoboken, NJ, USA, 2012.

MDPI
St. Alban-Anlage 66
4052 Basel
Switzerland
Tel. +41 61 683 77 34
Fax +41 61 302 89 18
www.mdpi.com

Catalysts Editorial Office
E-mail: catalysts@mdpi.com
www.mdpi.com/journal/catalysts

MDPI
St. Alban-Anlage 66
4052 Basel
Switzerland

Tel: +41 61 683 77 34
Fax: +41 61 302 89 18

www.mdpi.com

ISBN 978-3-0365-3602-6